SERI/TR-252-2897
UC Category: 59a
DE88001119

Experimental Studies of Heat and Mass Exchange in Parallel-Passage Rotary Desiccant Dehumidifiers for Solar Cooling Applications

D. Bharathan
J. M. Parsons
I. L. Maclaine-cross

November 1987

Prepared under Task No. 3023.210
FTP No. 01-540A

Solar Energy Research Institute
A Division of Midwest Research Institute

1617 Cole Boulevard
Golden, Colorado 80401-3393

Prepared for the
U.S. Department of Energy
Contract No. DE-AC02-83CH10093

Printed in the United States of America
Available from:
National Technical Information Service
U.S. Department of Commerce
5285 Port Royal Road
Springfield, VA 22161

Price: Microfiche A01
Printed Copy A06

Codes are used for pricing all publications. The code is determined by the number of pages in the publication. Information pertaining to the pricing codes can be found in the current issue of the following publications, which are generally available in most libraries: *Energy Research Abstracts, (ERA); Government Reports Announcements* and Index (*GRA* and I); *Scientific and Technical Abstract Reports (STAR);* and publication, NTIS-PR-360 available from NTIS at the above address.

PREFACE

In keeping with the national energy policy goal of fostering an adequate supply of energy at a reasonable cost, the United States Department of Energy (DOE) supports a variety of programs to promote a balanced and mixed energy resource system. The mission of the DOE Solar Buildings Research and Development Program is to support this goal by providing for the development of solar technology alternatives for the buildings sector. It is the goal of the Program to establish a proven technology base to allow industry to develop solar products and designs for buildings that are economically competitive and can contribute significantly to building energy supplies nationally. Toward this end, the program sponsors research activities related to increasing the efficiency, reducing the cost, and improving the long-term durability of passive and active solar systems for water and space heating, cooling, and daylighting applications. These activities are conducted in four major areas: Advanced Passive Solar Materials Research, Collector Technology Research, Cooling Systems Research, and Systems Analysis and Applications Research.

<u>Advanced Passive Solar Materials Research</u> — This activity area includes work on new aperture materials for controlling solar heat gains and for enhancing the use of daylight for building interior lighting purposes. It also encompasses work on low-cost thermal storage materials that have high thermal storage capacity and can be integrated with conventional building elements, and work on materials and methods to transport thermal energy efficiently between any building exterior surface and the building interior by non-mechanical means.

<u>Collector Technology Research</u> — This activity area encompasses work on advanced, low-to-medium-temperature (up to 180°F useful operating temperature) flat-plate collectors for water and space heating applications, and medium-to-high-temperature (up to 400°F useful operating temperature) evacuated tube/concentrating collectors for space heating and cooling applications. The focus is on design innovations using new materials and fabrication techniques.

<u>Cooling Systems Research</u> — This activity area involves research on high-performance dehumidifiers and chillers that can operate efficiently with the variable thermal outputs and delivery temperatures associated with solar collectors. It also includes work on advanced passive cooling techniques.

<u>Systems Analysis and Applications Research</u> — This activity area encompasses experimental testing, analysis, and evaluation of solar heating, cooling, and daylighting systems for residential and nonresidential buildings. This involves system integration studies, the development of design and analysis tools, and the establishment of overall cost, performance, and durability targets for various technologies and system options.

A national goal of DOE's cooling systems research is to reduce the amount of nonrenewable energy required to maintain comfort in buildings. Thus, the Solar Energy Research Institute (SERI), for DOE's Solar Buildings Research and Development Program, has been conducting fundamental heat and mass transfer research in desiccant dehumidifiers for solar cooling applications.

This report contains an account of research at SERI in cooling systems, particularly concerning the performance of advanced, parallel-passage, rotary dehumidifiers. Detailed descriptions of the experimental method and data analyses are provided. Work in SERI's Cyclic Test Facility has culminated in a better understanding of the research issues related to rotary dehumidifiers having practical geometries.

The authors would like to express their appreciation to L. Flowers for his leadership as the technical program integrator, and to T. Penney, K. Schultz, F. Zangrando, H. Pohl, J. Dolan, and K. Dukehart for carrying out various aspects of the task so that this report could be completed.

D. Bharathan, Senior Engineer

Approved for

Solar Energy Research Institute

D. H. Johnson, Manager
Solar Thermal Research Branch

G. C. Groff, Director
Solar Heat Research Division

SUMMARY

Objective

The objective of this work was to experimentally characterize the performance of rotary desiccant dehumidifiers and to develop and validate analytical methods for evaluating their performance in air-conditioning systems.

Discussion

SERI has developed a facility and a test-and-analysis procedure to evaluate the performance of rotary dehumidifiers. Experiments were aimed at developing a basic understanding of the simultaneous heat- and mass-transfer processes in rotary dehumidifiers. Two dehumidifier test articles were tested under cyclic operation to fully characterize their performance. Detailed accounts of SERI's Cyclic Test Facility, its hardware and instrumentation, the two test articles, data generated on the test articles, and data reduction and analyses methods are provided in this report. The data provide an engineering data base for evaluating rotary dehumidifiers for cooling applications.

Conclusions

For a simple low-pressure-drop geometry, such as the parallel plate, ensuring and maintaining a uniform air passage gap is critical to obtaining high performance. The tests reported here indicate that nonuniform passage spacing, in which 48% of the passages possess gaps ranging from 0.08 to 1.92 times the design gap, resulted in about a 50% reduction in the overall number of transfer units for dehumidification from the nominal design value of 10.

Low- and high-speed test results correlated well with the analogy theory, while medium-speed results deviated significantly from this theory. A nonlinear analogy method incorporating a linear variation of the matrix capacity was adopted to analyze the medium-speed results, with satisfactory agreement.

The effective gel mass in the matrix was found to be 63% of the total gel mass. Independent static tests confirmed this finding. The dehumidifier's performance as measured by the effectiveness agreed with theory to within ±10%. This work represents the first attempt to compare a detailed component model for a rotary desiccant dehumidifier with a complete set of experimental data relevant to solar cooling applications.

The Cyclic Test Facility at SERI can be used to further improve the theoretical model for other desiccants and geometries. The model will help designers determine the trade-offs that must be made among such design characteristics as pressure loss, mass-transfer performance, cost, reliability, and aging.

TABLE OF CONTENTS

TABLE OF CONTENTS (Concluded)

LIST OF FIGURES

LIST OF FIGURES (Concluded)

LIST OF TABLES

NOMENCLATURE

A_c	minimum matrix flow area (m^2)
A_d	unobstructed upstream flow area (m^2)
A_{ref}	reference midsection matrix flow area (m^2)
A_2	nozzle exit flow area (m^2)
A_4	unobstructed downstream flow area (m^2)
A_i	dimensionless inverse propagation velocity
a	nominal coated tape thickness (m)
b	air passage gap (m)
b_m	mean air passage gap (m)
C_d	discharge coefficient
C_i	dimensionless rotational speed for the *ith* wave in the process period
C_{ij}	dimensionless rotational speed for the *ith* wave in the *jth* period
C_{max}	maximum air stream heat capacity rate (W/K)
C_{min}	minimum air stream heat capacity rate (W/K)
C_r	matrix heat capacity rotational rate (W/K)
COP	thermal coefficient of performance
C_{pa}	specific heat capacity of air (J/kg K)
C_{pd}	specific heat of desiccant (J/kg K)
$C_{p\ tape}$	specific heat of substrate tape (J/kg K)
$(C_{dA})_r$	radial leakage product of discharge coefficient times area (m^2)
$(C_{dA})_c$	circumferential leakage product of discharge coefficient times area (m^2)
c_m	mean air velocity (m/s)
c_{1p}, c_{1r}	nondimensional rotational speed for F_1 transfer for process and regeneration streams
c_{2p}, c_{2r}	nondimensional rotational speed for F_2 transfer for process and regeneration streams
cc	heat capacity of matrix per unit active desiccant mass (J/kg K)

NOMENCLATURE (Continued)

$\Delta c/c$	normalized variation in capacity ratios between process and regeneration streams
D_h	effective hydraulic diameter (m)
D_s	surface moisture diffusivity in desiccant (m^2/s)
D_W	moisture diffusivity in desiccant (m^2/s)
D_w	moisture diffusivity in air (m^2/s)
d_p	desiccant particle diameter (m)
E	thermocouple electromotive force
E_1	number of transfer units for sensible heat transfer
E_2	unbalance in air mass flow ratio between process and regeneration streams
E_3	nondimensional rotational speed for sensible heat transfer
E_4	unbalance ratio in heat transfer coefficient times transfer area product
e_s	solid-side conductance geometry factor
F_{ij}	combined *ith* potential for the *jth* period
F_1	combined first potential
F_2	combined second potential
f	Fanning friction factor
f_w	fugacity of water vapor in air
f_{ws}	fugacity of water vapor in air at saturation
Gr	Graetz number
g	gravitational acceleration (m^2/s)
h	specific enthalpy of air (J/kg) or heat of adsorption (J/kg)
$(ha)'$	unbalance ratio in heat-transfer coefficient times transfer area product
h_{pi}	specific enthalpy of process inlet air stream (J/kg)
h_{po}	specific enthalpy of process outlet air stream (J/kg)
h_{ri}	specific enthalpy of regeneration inlet air stream (J/kg)

NOMENCLATURE (Continued)

h_{ro}	specific enthalpy of regeneration outlet air stream (J/kg)
Δh_r	change in regeneration stream specific enthalpy (J/kg)
Δh_p	change in process stream specific enthalpy (J/kg)
K	slope of nondimensional pressure-drop variation with Reynolds number
k_m	mean thermal conductivity of air (W/m K)
k_3	rotational correction coefficient
L	matrix depth (m)
Le	Lewis number
ℓ_1, ℓ_2	circumferential leakage rates at stations 1 and 2 (kg/s)
ℓ_3, ℓ_4	circumferential leakage rates at stations 3 and 4 (kg/s)
ℓ_{14}, ℓ_{23}	radial cross leakage rates (kg/s)
M_a	molecular weight of air (kg/mole)
M_w	molecular weight of water (kg/mole)
$\dot{m}_p, \dot{m}_r$	dry air mass flow rate of process and regeneration streams, respectively, corrected for leaks (kg/s)
$\dot{m}_1, \dot{m}_2$	dry air mass flow rate of process and regeneration streams at stations 1 and 2, respectively (kg/s)
m_{dd}	total mass of dry desiccant (kg)
N	wheel speed (rev/h)
NTU_o	overall number of transfer units
NTU_t	overall number of transfer units based on temperature
NTU_w	overall number of transfer units based on moisture transfer
Nu	Nusselt number
$(Nu)_{pp}$	Nusselt number for uniform parallel passages
p_{sat}, p_s	saturation pressure (Pa)
p_{amb}	ambient pressure (Pa)
p_f	fraction of passages outside of design gap or packing factor

NOMENCLATURE (Continued)

p_t total pressure (Pa)

p_1,p_2 inlet static pressures at stations 1 and 2 (Pa)

p_3,p_4 outlet static pressures at stations 3 and 4 (Pa)

Δp_p process stream pressure drop across matrix (Pa)

Δp_r regeneration stream pressure drop across matrix (Pa)

$p(b)$ probability density distribution of nonuniform passages

q dynamic pressure (Pa)

R universal gas constant (J/mole K)

R_d Reynolds number at metering nozzle exit

R_m ratio of maximum passage width to nominal passage width

Re Reynolds number

Re_m Reynolds number evaluated at mean properties

r relative humidity or wheel radius (m)

S derivative of logarithm of saturation pressure with temperature

Sc Schmidt number

sgf silica gel fraction

Sh Sherwood number

T absolute temperature (K)

T_{dp} dew-point temperature (^oC)

T_t upstream stagnation temperature (K)

t temperature (^oC)

t_{pi},t_{po} process inlet and outlet temperatures to the matrix (^oC)

t_{ri},t_{ro} regeneration inlet and outlet temperatures to the matrix (^oC)

t_m mean matrix temperature (^oC)

t_{pint} process intersection-point temperature (^oC)

t_{rint} regeneration intersection-point temperature (^oC)

NOMENCLATURE (Continued)

t_1, t_2	inlet temperatures at stations 1 and 2 (^oC)
t_3, t_4	outlet temperatures at stations 3 and 4 (^oC)
u	air velocity (m/s)
u_m	mean air velocity (m/s)
u_2	air velocity at matrix entry (m/s)
u_3	air velocity at matrix exit (m/s)
v_p	desiccant void volume (cc/g)
W	matrix moisture content (kg/kg)
w	absolute humidity of air (kg/kg of dry air)
w_m	mean air absolute humidity (kg/kg of dry air)
w_{pi}, w_{po}	process inlet and outlet absolute humidities (kg/kg of dry air)
w_{ri}, w_{ro}	regeneration inlet and outlet absolute humidities (kg/kg of dry air)
w_{pint}	process intersection-point absolute humidity (kg/kg of dry air)
w_{rint}	regeneration intersection-point absolute humidity (kg/kg of dry air)
w_1, w_2	absolute humidities at inlet stations 1 and 2 (kg/kg of dry air)
w_3, w_4	absolute humidities at outlet stations 3 and 4 (kg/kg of dry air)
w_p	change in absolute humidity of process stream through the matrix (kg/kg of dry air)
w_r	change in absolute humidity of regeneration stream through the matrix (kg/kg of dry air)
x	downstream distance (m)
x_{eff}	fraction of active desiccant mass to total

Greek Symbols

α_i	slope ($-\partial t/\partial w$) along the combined potential F_i
α_h	slope of lines of constant enthalpy in t vs. w plot
α_w	slope of lines of constant matrix moisture contant in t vs. w plot

NOMENCLATURE (Concluded)

β	metering nozzle contraction ratio or sorbability of matrix
γ_i	specific capacity ratio of F_i potential
γ_{1p}, γ_{2p}	specific capacity ratios for the process stream for the 1 and 2 potentials
γ_{1r}, γ_{2r}	specific capacity ratios for the regeneration stream for the 1 and 2 potentials
Δ	changes
ζ	$r\left(\frac{\partial W}{\partial r}\right)_t$
η_1, η_2	effectiveness for the F_1 and F_2 transfer
η_t	temperature effectiveness
η_w	moisture transfer effectiveness
θ	time (s)
Λ_p, Λ_r	process and regeneration NTUs for the combined potentials
λ	ratio of the heat of sorption to the enthalpy of moisture in fluid mixture
μ	ratio of desiccant mass to air mass in the matrix
μ_m	mean air dynamic viscosity (kg/m s)
ν	sorption parameter
ρ_d, ρ_s	desiccant density (kg/m^3)
ρ_m	mean air density (kg/m^3)
σ	ratio of specific heat of matrix to that of fluid mixture
τ	tortuosity of desiccant pores or residence time per period (s)
ψ	$\left(\frac{\partial h}{\partial w}\right)_t / h_s$
Ω	$1-p/p_t$

<u>Subscripts</u>

p	process
r	regeneration

1.0 INTRODUCTION

1.1 Solid Desiccant Cooling

A major national goal is to reduce the amount of nonrenewable energy required to maintain comfortable temperatures and humidity in buildings. In summer, infiltration, ventilation, solar gains, building envelope conduction, and internal heat and moisture generation by occupants and equipment (including artificial lighting) raise the temperature and humidity of the conditioned space. Better equipment, building design, insulation, sealing, and ventilation systems can reduce but not eliminate these loads. The heat and moisture generated by occupants depend on the building's function and cannot be significantly altered (Mitchell 1983). An economically competitive, reliable cooling system using renewable energy that reduces energy consumption is an attractive alternative to a conventional electric vapor-compression system for the consumer, utility, builder or developer, and equipment manufacturer.

After 60 years of research and development, the limits of conventional vapor compression systems are well understood. New cooling systems using renewable energy directly are being developed as the economics become favorable. Two renewable energy sources for cooling are direct solar energy and the energy of the unsaturated atmosphere. These energy sources impose constraints on the choice of systems. Closed cooling systems (in which the refrigerant does not contact the atmosphere) cannot use the energy of the unsaturated atmosphere. Open systems evaporating water into the atmosphere as a refrigerant use this energy source as well as less direct solar energy; e.g., the simple evaporative cooler requires nonrenewable energy only to move the air and water. Closed systems may be combined with open systems to form a hybrid and take maximum advantage of renewable resources.

Open systems perform less well in humid areas unless dehumidification is used. A solar collector will deliver more heat at low temperatures because heat losses are lower (Lunde 1980; Duffie and Beckman 1980). Thus, open cycles employing dehumidification are promising options for renewable energy cooling systems.

A nationally marketed system should be compact and have low capital and operating costs and few maintenance requirements, as well as high performance and reliability. High performance may be achieved if the system approaches the limits set by the second law of thermodynamics (Lavan et al. 1982; Van Den Bulck et al. 1983; Kang 1985; Maclaine-cross 1985). One of the Department of Energy (DOE) goals for a renewable energy cooling system for the year 2000 is a projected initial system cost of \$1500/ton of cooling capacity. Theoretical analyses indicate that this goal is achievable using advanced cycles that more closely approach these second-law limits (Maclaine-cross and Parsons 1986), provided that the heat transfer occurs across small temperature differences and mass transfer across small concentration differences. Rotary adiabatic regenerative dehumidifier designs offer a practical alternative in achieving the long-term DOE goal.

The design of regenerative dehumidifiers is, however, complicated by the mass transfer resistance and somewhat difficult manufacturing properties of available desiccants. Combining new materials, geometries, and innovative manufacturing techniques can reduce size, cost, and maintenance requirements and increase the performance and reliability of regenerative dehumidifiers.

Figure 1-1 shows the substantial progress of and future targets for one aspect of solid desiccant cooling cycle performance, namely, the thermal coefficient of performance

(COP) (Penney and Maclaine-cross 1985). The state of the art is a thermal COP of 1.0 at ARI standard test conditions. A major part of the last 20 years of progress has been due to improvements in dehumidifiers. Achievement of the year 2000 goal of a thermal COP of 2.0 or more depends on dehumidifier improvements as well as progress in other areas.

The Solar Energy Research Institute (SERI), for DOE's Solar Buildings Research and Development Program, has been making fundamental heat- and mass-transfer measurements on solid desiccant materials, matrices, and model dehumidifiers. In four separate test facilities at SERI, a variety of research issues related to desiccants for solar cooling applications are addressed (Penney and Maclaine-cross 1985).

1.2 Purpose of the Research

The purpose of the research activities under the present task is to characterize experimentally the performance of advanced dehumidifiers operating at conditions relevant to solar cooling applications. The scope of the work encompasses test-article selection in regard to desiccant material, substrate, and matrix; limited practical aspects of engineering design and fabrication; testing; data collection; data analyses; analytical model validation; and research issues recommended to further improve the dehumidifiers' performance and the predictive methodology. The FY 1985 work consisted of characterizing two dehumidifier geometries. Data analyses have been confined to adapting analogy theories, assuming a linear matrix capacity variation with air state properties.

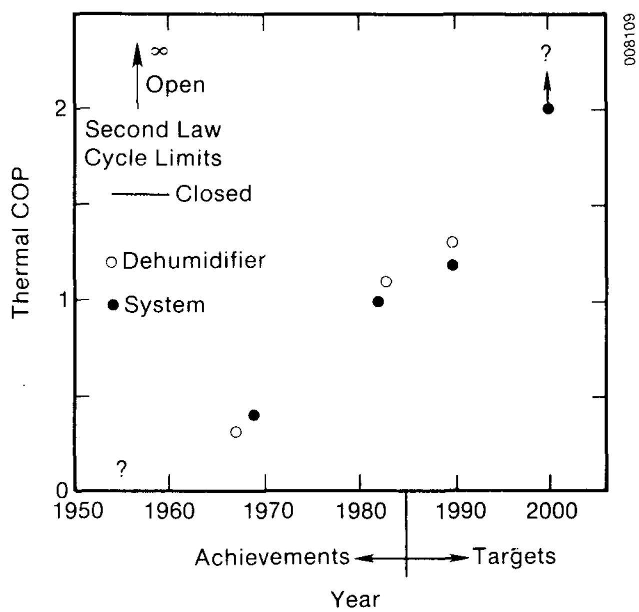

Figure 1-1. Progress in Desiccant Open-Cycle Thermal Coefficient of Performance at ARI Conditions

This report describes recent improvements to the Cyclic Test Facility at SERI, the two dehumidifier test articles, measurements of these units using the Cyclic Test Facility, and the calculation of the combined heat and mass transfer characteristics of the dehumidifiers from the measurements. The facility is described in Section 2.0, the test articles in Section 3.0, the experimental procedures in Section 4.0, and the results in Section 5.0. Appendices A through H complement these descriptions with respect to details concerning measurement uncertainties, the experimental data, dehumidifier fabrication, desiccant properties, seal leakage, effects of nonuniform passages, the data processing procedure, and the experimental procedure, respectively. Appendix I presents the method used to determine the dehumidifier's wheel static capacity.

1.3 Theory of Rotary Dehumidifier Tests

In rotary dehumidifiers the process airstream transfers moisture to and absorbs sensible heat from a rotating desiccant matrix, which subsequently transfers the moisture to and absorbs sensible heat from a counterflow regeneration airstream. The matrix may be homogeneous or a composite of a carrier with the mechanical properties necessary to support the desiccant, an adhesive film to bind the desiccant to the carrier, and the desiccant film or powder itself. Combined heat and mass transfer occurs in the air, the desiccant, and contaminants, if present. Heat transfer occurs in the carrier and the adhesive. Figure 1-2 shows these components, transfers, and important parameters schematically.

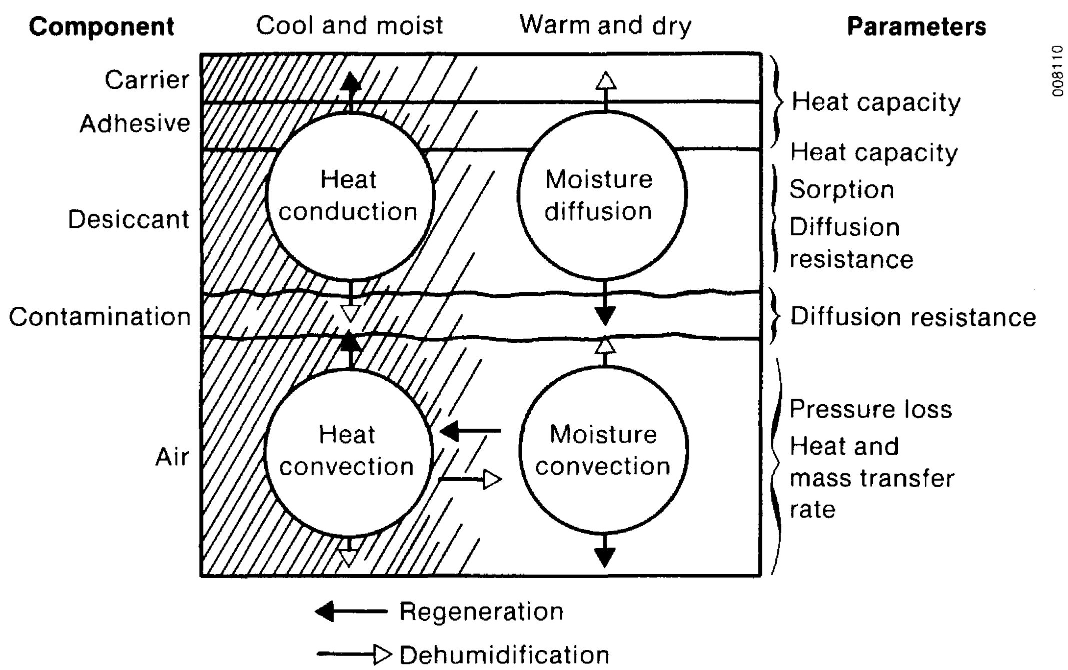

Figure 1-2. Combined Heat- and Mass-Transfer Processes in a Dehumidifier

The combined heat-and mass-transfer processes in the air are well understood and are similar to those for the wet bulb psychrometer. Wylie (1969, 1981) found for the wet bulb psychrometer that of the 10 known combined heat- and mass-transfer effects, six almost cancelled one another within a fraction of a percentage point. The important four remaining are diffusion, conduction, convection, and the accommodation coefficient at the surface. These effects have been measured within a few percentage points (Hilsenrath et al. 1958; Mason and Monchick 1965). Combined heat and mass transfer in air can be represented by heat transfer and mass transfer coefficients free of coupled effects, and for simple geometries they can be predicted accurately.

In the desiccant dehumidifier, combined heat and mass transfer can be more difficult to predict, especially if the dimensions of the desiccant in the transfer direction are comparable with those of the air passage. For high performance and low cost, the desiccant dimensions are usually made as small as practical compared with the air passage dimensions. This makes the desiccant almost isothermal, and only the mass transfer resistance need be considered. The diffusivity of liquid or crystalline desiccants is reproducible, but for amorphous polymers, such as silica gel, it can be highly dependent on manufacturing conditions. Contaminants commonly found in buildings can be adsorbed by the desiccant. Their likely chemical composition and effect on desiccant cooling systems is not known at present. For the tests described in this report, however, precautions have been taken in both construction and installation to avoid undue contamination.

For high-performance dehumidifier designs, the temperature and concentration differences between the desiccant and matrix are usually small. There is no reason to believe that transfer rates between the desiccant and air cannot be modeled adequately by sensible heat and mass transfer coefficients. Their values depend on the geometry and the physical properties of air and matrix. The geometry may be difficult to describe and analyze mathematically, and matrix properties in sufficient detail may be unknown. Measurement of the transfer coefficients is an important objective of dehumidifier tests. The dimensionless ratio of mass-transfer to heat-transfer resistance or an effective Lewis number is a useful index of matrix performance, because reducing the mass-transfer resistance improves the dehumidifier's performance.

The equilibrium properties of humid air and the matrix are also important in defining the dehumidifier's performance. The matrix vapor pressure isotherm, heat of adsorption, and specific heat all affect the dehumidifier's performance (Jurinak and Mitchell 1984). For amorphous desiccants, these properties, and especially the isotherm, are highly dependent on manufacturing conditions. The adhesive or contaminants may penetrate or isolate the desiccant, desiccant may be lost from the dehumidifier during operation, or matrix manufacturing nonuniformities may partially isolate the desiccant, all reducing the effective slope of the isotherm. These practical considerations make it essential to measure the "effective" equilibrium properties of the dehumidifier matrix rather than to make extrapolations based on idealized models of segments of the matrix.

Capital cost and parasitic power must both be low for an advanced dehumidifier. This requires that the matrix possess a low pressure drop at high mass flow rates and suffer no loss in either transfer rates or equilibrium capacities. A favorable passage geometry and high matrix porosity are imperative. The parallel-plate geometry, which can provide both low pressure drop and high porosity, is relatively easy to construct and analyze (Dunkle et al. 1980). Pressure drop and mass flow rate are important measures of the dehumidifier's performance.

The six dehumidifier measurements we have discussed may be correlated conveniently using the Nusselt number, the ratio of measured to predicted desiccant mass-transfer resistance, the ratio of effective to actual desiccant dry mass, the apparent specific heat of the carrier, the product of the Fanning friction factor times the Reynolds number, and the Reynolds number times the ratio of minimum free flow to wetted surface area. For turbulent flow or unquantifiable geometries, slight modifications to this choice of parameters are necessary, but such tests have not yet been made. Adiabatic step transient tests are capable of measuring all these quantities (Pesaran et al. 1986). The construction of a single rotary dehumidifier test article is difficult, and cyclic test facilities are complicated and expensive to design and assemble. The expense, however, is justified because the theory of combined heat and mass transfer in dehumidifiers allows the first four measurements to be calculated from cyclic regenerator tests with greater accuracy than they could be from more economical test methods. The cyclic tests also provide an important basis for predicting dehumidifier performance under other than the test conditions. The predictive methodology is briefly discussed here.

Simultaneous partial differential equations can be written for transfer rates, conservation, and equilibrium to describe combined heat and mass transfer in dehumidifiers. The transfer coefficients and matrix mass may be corrected for a variety of effects, such as conduction in the flow direction, so additional terms do not have to be added to the equations and the boundary conditions do not have to be modified (Maclaine-cross 1973, 1980). The same set of partial differential equations (Maclaine-cross 1973) can be used to describe all dehumidifiers of interest. However, coupling in the rate equations and coupling and nonlinearity in the equilibrium relations complicate the solution of the equations. Many empirical, approximate, and semianalytical methods have been used in predicting dehumidifier performance, but for calculating test results there are two useful methods: analogy to heat transfer alone and the finite-difference solution.

D'Alembert's classical mathematical method for solving simultaneous differential equations consists of finding multipliers for the equations that convert them to a number of independent sets of equations in canonical variables. These appear in only one equation, which then can be solved independently of the others. This approach was first applied to a combined heat and mass transfer system by Henry (1939). Banks (1972) improved the usefulness of this method by introducing the concept of combined potentials F_i and combined specific capacity ratios γ_i.

When this method is applied to dehumidifiers (Maclaine-cross and Banks 1972), the enthalpy and moisture contents of the air and matrix are replaced in the equations by the "combined potentials" of the air and matrix. The equations are then reduced to two sets of equations, each individually the described the behavior of one combined potential. Each set of equations is analogous to those for heat transfer (alone) in rotary heat exchangers, and there are in the literature tables, charts, and simplified equations for their solution (Kays and London 1964). In the analogy to heat transfer, the combined potentials are analogous to temperature or the driving potential, and the combined specific capacity ratios are analogous to the ratio of the matrix to fluid specific heat.

Figure 1-3 shows the combined potentials and Figure 1-4 the combined specific capacity ratios for a simplified silica gel (Banks et al. 1970). The combined potentials and specific capacity ratios used here were calculated using the algorithms and equations described in Appendix D. Should the lines of constant potential and specific capacity ratios be orthogonal, we may infer that the described equations are uncoupled. However, Figures 1-3 and 1-4 show that the equations are still coupled, because the combined specific capacity ratios are functions of both the combined potentials. Maclaine-cross and Banks (1972) suggested that errors due to this coupling could be reduced if

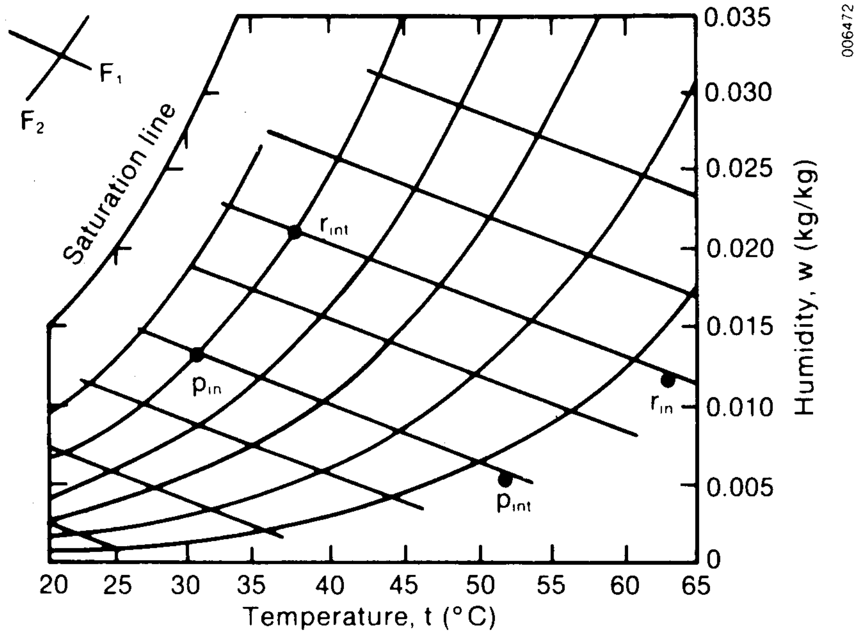

Source: Maclaine-cross 1974

Figure 1-3. **Lines of Constant Combined Potentials F_i for a Simplified Silica Gel-Water-Air System (p = process; r = regeneration; in = inlet; int = intersection point)**

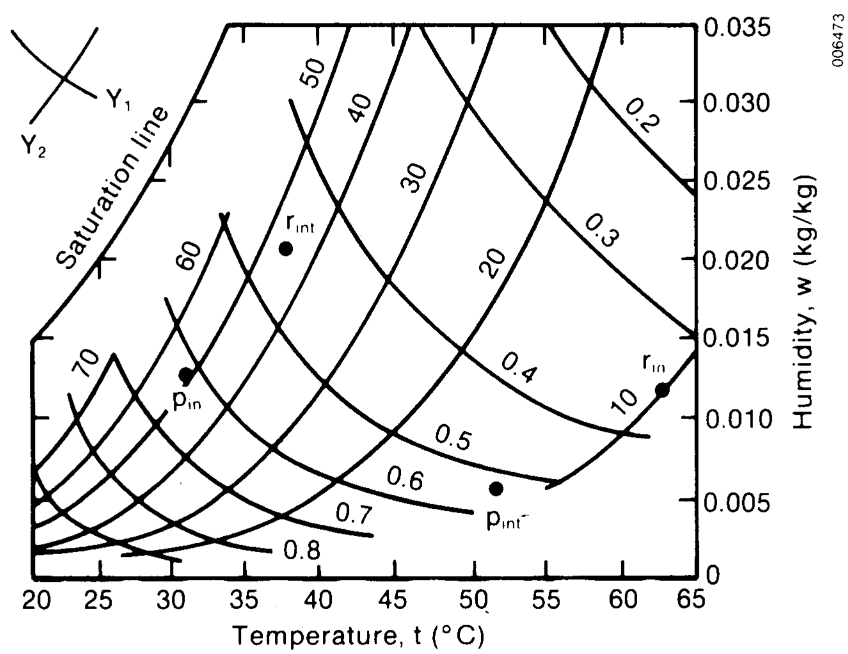

Source: Maclaine-cross 1974

Figure 1-4. **Specific Capacity Ratios γ_i for a Simplified Silica Gel-Water-Air System (p = process; r = regeneration; in = inlet; int = intersection point)**

appropriate average values of the combined specific capacity ratios were used in the dimensionless parameters of the analogous heat-transfer-alone solutions. The accuracy of this suggestion and other details of the analogy method have been examined in subsequent studies and refinements (Maclaine-cross 1973, 1974; Jurinak and Banks 1982; Banks 1985).

For a sensible heat regenerator, the performance is expressed in terms of an effectiveness that is a function of four nondimensional parameters, E_1 through E_4 (Maclaine-cross 1974). The overall number of transfer units E_1 is proportional to the heat-transfer coefficients of the process and regeneration streams, the fluid stream capacity rate ratio E_2 is proportional to the mass flow ratio between the two streams, the capacity rate ratio E_3 is proportional to the heat exchanger matrix rotational speed, and the ratio of heat-transfer coefficient times the area between the two streams is represented by parameter E_4. Figure 1-5 illustrates the dependence of sensible heat exchanger effectiveness η as a function of the nondimensional matrix rotational speed E_3 for selected values of the other three parameters.

From this figure, we note that for $E_3 < 1$, the effectiveness is proportional to E_3 and is essentially independent of other parameters, including the heat-transfer coefficients. At E_3 far greater than one, the effectiveness is independent of the rotational speed E_3 and is asymptotic to the effectiveness of a counterflow heat exchanger. These results, along with the use of the analogy theory, can be used to explain the great accuracy that can be obtained from cyclic dehumidifier tests.

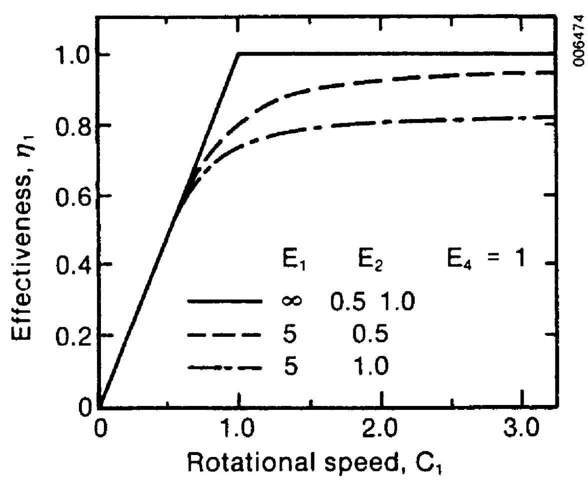

Figure 1-5. Comparison of Infinite and Finite Transfer Coefficient Solutions for Counterflow Regenerator, Plotted as Transfer Effectiveness η vs. Rotational Speed C_1

To look at the dehumidifier analogous to the sensible heat exchanger, the dehumidifier is viewed as two independent rotors, each one acting to transfer one of the combined potentials F_i ($i = 1,2$). The process and regeneration streams are denoted by periods j, with $j = 1$ or 2. The nondimensional matrix rotational speed for a potential i and a period j is denoted by C_{ij}.

When $C_{ij} \gg 1$ (for all i's and j's), the dehumidifier is operating at a high rotational speed. The analogy theory and Figure 1-5 predict that rotational speed effects are small and the temperature and moisture effectiveness depend mainly on the heat- and mass-transfer coefficients. The dehumidifier outlet state is relatively uniform, allowing for accuracy in measuring the bulk mean air outlet states and hence efficiencies. Corrections for the small rotational speed effects can be made using the analogy method, which is very accurate at high rotational speeds (Maclaine-cross 1974). High rotational speed cyclic tests provide the most accurate method known to us of measuring dehumidifier transfer coefficients.

A dehumidifier with $C_{ij} \ll 1$ for both combined potentials i and periods j is operating at a low rotational speed. The analogy theory and Figure 1-5 predict that the efficiencies are almost proportional to rotational speed and almost independent of the transfer coefficients. The temperature and moisture gradients are strong, reducing the accuracy of efficiency measurements slightly. Combined potential two efficiency is almost proportional to the active mass of desiccant on the matrix, which is an important dehumidifier performance parameter. Combined potential one efficiency is almost proportional to combined specific capacity ratio one, which is strongly dependent on the effective heat capacity of the matrix. Low-rotational-speed cyclic tests allow us to infer the two most important equilibrium dehumidifier properties accurately.

When C_{ij} lies in the neighborhood of unity, the dehumidifier is operating at a medium rotational speed. The best rotational speed for dehumidifier operation is at the low end of this speed range (Jurinak 1982; Van Den Bulck et al. 1985). The dehumidifier properties measured at high and low rotational speeds can be used to predict performance accurately in the medium-speed range. The errors in the analogy method are greatest in this speed range, making accurate finite-difference solutions (Maclaine-cross 1973) essential for highly accurate comparisons. If the analogy theory is used to reduce results with $C_{ij} > 0.5$, the analogous heat-transfer-alone solutions should include the effect of variable specific heat (Maclaine-cross 1978; Banks 1985). Despite these limitations, the analogy method has advantages over other solution methods in providing a better understanding of the exchanger's operation, in enabling performance predictions to be made via parameters analogous to those for heat exchangers, and in its computational speed. For the checks of experimental consistency required here, the analogy method is satisfactory.

For the analogy method, the transformation of rate and conservation equations for the dehumidifier into the same form as for a sensible heat exchanger requires defining the new dependent variables combined potentials F_1 and F_2 and analogous capacity ratios γ_1 and γ_2. In addition, various assumptions are satisfied exactly if the regenerator overall NTU approaches infinity, the effective overall Lewis number ($Le_o = NTU_t/NTU_w$) is unity, the combined potentials are truly orthogonal, and the capacity ratios γ_1 and γ_2 do not vary through the process. For a practical dehumidifier, none of these assumptions hold well. The influence of deviations from the assumptions has been examined by Banks (1985) and Jurinak (1982). Banks established that with the removal of moisture from air using silica gel, the combined potentials F_1 and F_2 may be treated as orthogonal. Jurinak inferred that for specific process and regeneration conditions (35°C, 14.2 g/kg for process and 85°C, 14.2 g/kg for regeneration)--overall NTU > 1.25 and effective Lewis number < 2.0--the errors in the analogy method using the intersection point were limited to less than 1°C and 0.5 g/kg in the air outlet states when compared to a finite-difference solution. Jurinak, however, used average values for the capacity rate ratios γ_1 and γ_2 in his calculations.

For this study of a silica-gel dehumidifier, the experimentally inferred overall NTU was found to be greater than 6 at all tested air flow rates, and the effective Lewis number was less than 1.2 (see Section 5.2). The use of average values for γ_1 and γ_2 was found to be unsatisfactory at medium wheel rotational speeds. To remedy this problem, the calculation method of Lambertson (1958) was modified to incorporate the varying specific capacity of the sensible heat regenerator. Thus, the analogy method used in this report for analyses of the experimental data is entirely consistent with the experimental measurement uncertainties and findings reported in later sections.

1.4 Dehumidifier Test Techniques

The measurement of dehumidifier performance is among the most difficult in mechanical engineering. The six parameters of interest require the simultaneous measurement of air flow, pressure, temperature, humidity, and rotational speed. No standards exist for testing dehumidifiers; the national standards for measuring air flow, temperature, and humidity yield accuracies considerably less than those required for predicting the performance of solid desiccant cooling systems to within 10%. The bulk mean air state must be integrated with great accuracy at a minimum of four locations. These difficulties are formidable and were perhaps the experimental limitations when desiccant cooling was invented over 30 years ago (Pennington 1955). Improvements in measurement techniques, however, and greater experience in dehumidifier testing have resulted in greater accuracies in these measurements.

The design of the SERI Cyclic Test Facility is described by Schlepp et al. (1984). This design was based on a survey of domestic dehumidifier test facilities. Schultz (1986) has described measurements on a preliminary test article using this facility. Recent facility modifications to improve the accuracy of the measurements are described later in this report. Further improvements may be necessary to detect smaller differences between dehumidifiers or deviations from ideal performance.

Dehumidifier tests have been performed in Australia (Dunkle et al. 1980; van Leersum and Close 1982), Canada, and Europe (Spahn and Gnielinski 1971). Most of these tests have employed larger diameter dehumidifiers than the SERI facility was designed for, typically 1.25 m. This choice was usually made on the grounds that greater measurement accuracy could be obtained with the larger size because there would be less disturbance of flow by instruments, a higher Reynolds number in flow measuring devices and ducts, and a lower duct perimeter and hence less heat loss per unit mass flow.

The Monash University (Ambrose et al. 1983) and University of Manitoba (Chant et al. 1973) test rigs are for a 1.25-m rotor diameter using a single-loop design. One advantage that this design offers is the ability to measure the dehumidifier's performance with a heat- and mass-balance on the loop, which is less dependent on sensor accuracy and integration errors (Ambrose et al. 1983).

Wet-bulb psychrometer accuracy has improved substantially (Wylie 1981; Lee 1984) as a result of greater theoretical understanding. Humidity can now be measured with an uncertainty of less than 1% in the psychrometer constant. International and foreign standards (Ower and Pankhurst 1975) permit the measurement of air flow and pressure drop with an error about half that of domestic standards. The cone inlet nozzle is particularly convenient because it does not require an upstream length of straight duct; it has been used successfully in Australia (Ambrose et al. 1983; van Leersum and Close 1982; Maclaine-cross and Ambrose 1980).

1.5 Results of Previous Tests

Switched beds of silica gel beads have been tested by Johnston (1967), the results correlated statistically, and the performance of a desiccant cooling system predicted. The predicted thermal COPs were less than 0.5, indicating very poor dehumidifier performance.

Van Leersum and Close (1982) reported tests on rotating beds of silica gel beads. They were not able to correlate the results with either the analogy theory or finite-difference solutions, but the effective Lewis numbers all appeared to be significantly greater than 2.0.

Dunkle et al. (1980) reported that high rotational speed tests on parallel-plate, wool, and salt-impregnated matrices indicated high mass transfer resistance.

Schultz (1986) presented the first but limited set of cyclic test results over the full rotational speed range on a parallel-plate dehumidifier spirally wound from polyester adhesive tape coated with silica gel particles. The passages were highly nonuniform, because of practical mechanical problems in winding (see also Appendix C). From a limited number of low-speed tests, approximately 90% of the gel present on the matrix appeared to be active. The overall Lewis number ranged from 1.1 to 2.0.

2.0 THE EXPERIMENTAL FACILITY

2.1 Overview

Over the past two years, SERI has designed and implemented a versatile experimental facility, the Cyclic Test Facility, to permit the experimental evaluation of rotary mass and heat exchangers operating between co- or counterflowing air streams (Schlepp et al. 1984; Schultz 1986). Our focus has been on solar cooling applications, to obtain experimental performance data on advanced rotary desiccant dehumidifiers. The facility is thus equipped to provide two independent air streams, one for process and the other for regeneration of the desiccant wheel.

For the process stream, the maximum air flow rate is 0.45 kg/s, which can be supplied at a maximum temperature of 35°C and a relative humidity of up to 95%. The maximum capabilities of the regeneration stream are a 0.45-kg/s air flow rate, a 100°C temperature, and 10% relative humidity at the maximum air flow.

The facility is equipped with a full set of automated controls to maintain steady inlet conditions, instrumentation to characterize air stream inlet and outlet conditions (flow, temperature, and humidity) for both process and regeneration, and a variable-speed drive for wheel-speed control, regulation, and monitoring. There are also provisions for monitoring ambient air conditions. Detailed descriptions of the Cyclic Test Facility, including its hardware, control systems, and instrumentation, are provided in this section. (We list specific manufacturers and model numbers for information purposes only).

2.2 The Cyclic Test Facility

Figure 2-1 is a schematic of the Cyclic Test Facility located in the west high bay of SERI's Field Test Laboratory Building. The facility is designed to provide two independent streams of air, process and regeneration, to the test unit.

For the process stream, induced room air is first heated and then humidified to achieve the air temperature and humidity required. It then flows through a variable-speed fan and through a long, straight-duct section for flow metering. Just upstream of entry into the test article, inlet air states are monitored at station 1. Outlet states are monitored at station 3. The outlet flow rate can again be metered through a second ASME flow nozzle before the air is exhausted back into the room.

The regeneration stream is configured similarly to the process stream, with inlet and outlet states monitored at stations 2 and 4, respectively.

2.2.1 Process Control

All process variables are monitored and feedback signals are initiated via a data acquisition/control unit (Hewlett Packard, model 3497A) controlled by a personal computer (International Business Machines, model PC). The control unit is equipped with an extender (Hewlett Packard, model 3498A) to provide a total of 15 slots for data acquisition and control card placement.

The computer is provided with 512 kB of memory and two 360-kB floppy diskette drives. It communicates with the control unit via a serial interface (RS-232) at a baud rate of 2400 bps. The data gathered by the control unit and commands initiated by the computer

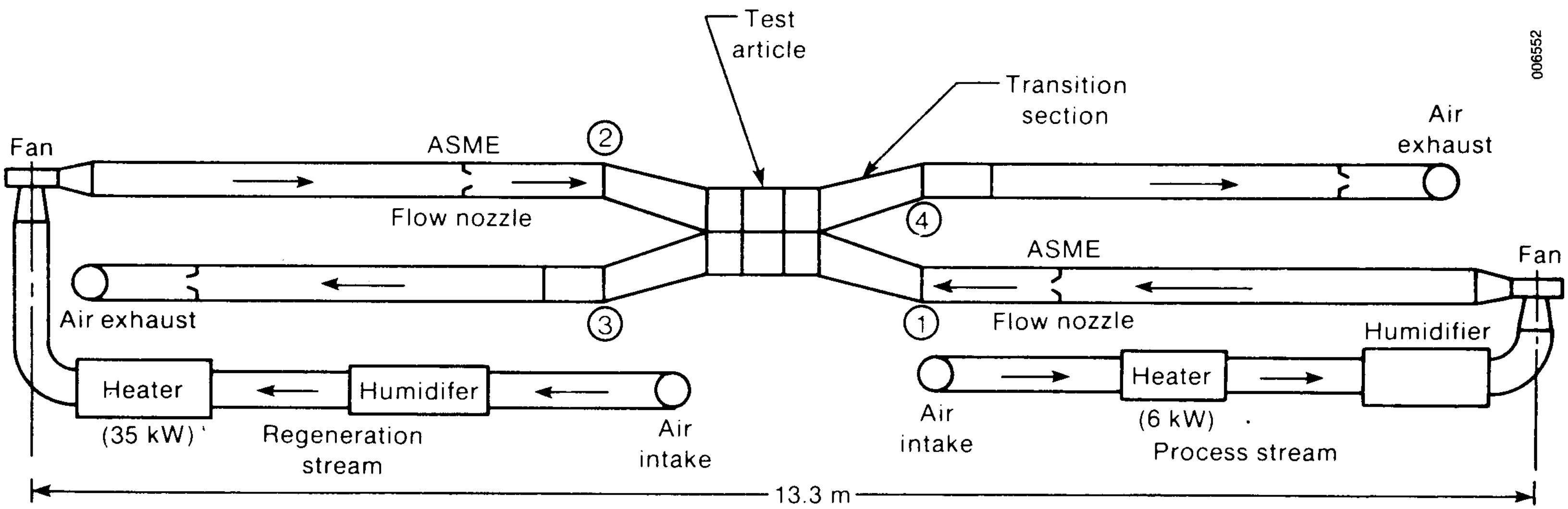

Figure 2-1. Schematic Layout of the Cyclic Test Facility

are coordinated by means of an inquire/acknowledge software handshake. Data gathered by the computer are displayed on a monitor and also stored in floppy diskettes for further processing.

2.2.1.1 Air Flow

Air flow for each stream is induced by a centrifugal blower (New York Blower, model compact GI124, rated at 0.5 m^3/s at 1000 Pa static pressure) driven by a 2-hp, variable-speed ac motor. The motor is powered by a variable-frequency speed controller (Fincor, model 5100), which converts a 230-V, single-phase, 60-Hz power source to an ac voltage of a frequency proportional to an input dc current signal of 4 to 20 mA. This input signal is provided by a current source card located in the HP3497A control unit.

Air flow control is accomplished by inferring the air flow rate from the measured Δp across the ASME metering nozzle, computing an error proportional to the deviation from the set point, and feeding back a proportional current signal to the fan speed controller. Typically, the time required to achieve a set-point flow rate within a few percentage points was found to be about 40 s.

2.2.1.2 Air Temperature

Heat is added to each stream by a 480-V, three-phase electric resistance duct heater. The process stream heater has a capacity of 6 kW, and the regeneration heater, 35 kW. Power input to the heater is regulated by a silicon-controlled rectifier (SCR) controller (Holmar Electronics, series LZF2) which accepts a 0-5 mA current signal as input. Again, using a differential proportional control based on measured and set-point air temperature, a feedback signal is sent to the SCR power supply to the respective heater. Under steady state, for typical experimental conditions, air temperature fluctuations can be held to within ±0.2°C over test periods of 4 hours or more.

2.2.1.3 Air Humidity

We maintained the humidity conditions by injecting steam into the air streams. The steam is generated by an Electro-Steam (50-kW electric boiler with on/off control) through a pressure regulator with 4-kPa (1/2-psi) differential (Watts Regulator Co., model 5M3). The steam is injected into the air stream through a Walton ST-100 steam humidifier. The steam flow to each stream is regulated by a Fisher Control electro-pneumatic valve.

Hysteresis in the control valves and the long response time (15-20 s) of the humidity sensing loop made computer control of the steam flow difficult. Fluctuations in the laboratory air humidity ratio further complicated the task. Currently, we control the steam flow manually from the IBM PC. An integer value (between 3,000 and 10,000) from the IBM PC is converted to a current signal (between 4 and 20 mA) by the HP3497A. The current signal determines the position of the pneumatic valve. The search for the correct valve position requires the operator's continual attention. The inlet humidity ratio can be held to within ±0.5 g/kg for each stream during the course of an experiment.

2.2.1.4 Wheel Speed

The dehumidifier is circumferentially friction-driven by a dc servomotor (Electro-Craft Corp., model E26-2) turning a rubber-rimmed drive wheel through a reduction gear assembly. An optical encoder (BEI encoder model E25AB) mounted on the drive motor outputs 1000 pulses per motor revolution, which is monitored by a counter card

(HP 44426A) in the HP3497A. The HP3497A averages the elapsed time per revolution over a thousand counts, and this information, together with the gear-reduction ratio, allows us to calculate the wheel speed. The drive motor is driven by a manually controlled, 40-V, 8-A power supply (KEPCO, model JQE 36-8M). Manual control is acceptable in this case, as we can reach set-point wheel speeds within 20-30 seconds and hold them to within ±1.0%.

2.2.2 Instrumentation

Figure 2-2 shows the arrangement of instrumentation adjacent to the test article. These include four sets of temperature and humidity measuring devices, two differential pressure transducers, and a wheel-speed measuring device. In addition, farther away from the test article, a set of four ASME flow nozzles together with their Δp transducers helps to monitor the flow rates.

Table 2-1 summarizes the instrumentation. Further details on each measurement are provided below.

2.2.2.1 Air Temperatures

Air temperatures upstream and downstream of the dehumidifer are measured for each stream using a set of four bare wire copper/constantan (type T) thermocouple junctions arranged in parallel. Sufficient bare wire was exposed to the air stream near the

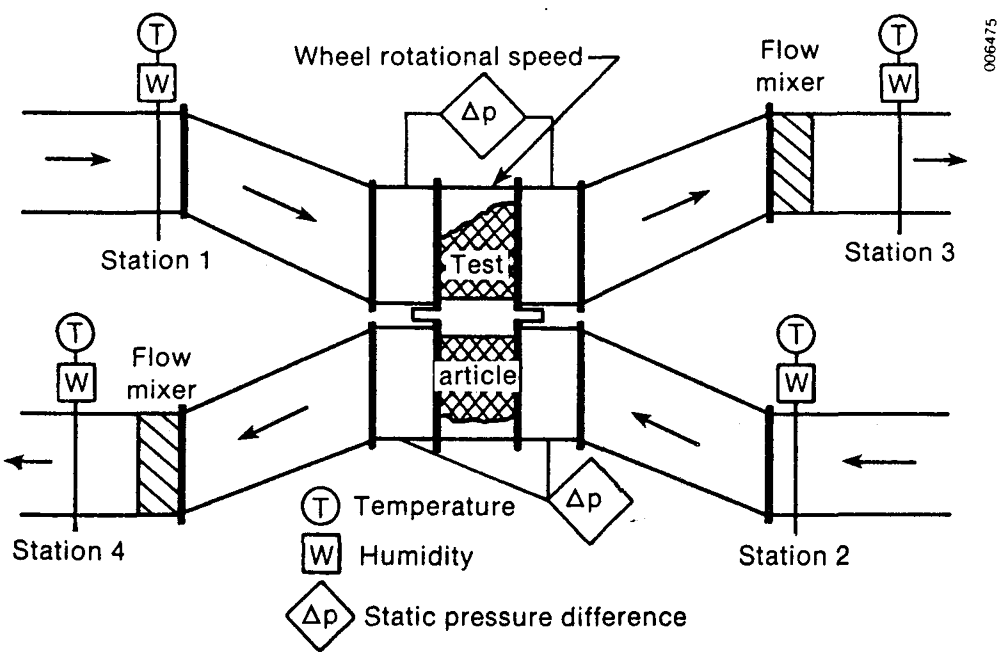

Figure 2-2. Locations of Instrumentation near and around the Test Article

Table 2-1. Summary of Instrumentation for the Cyclic Test Facility

Variable	Device	Comments
Wp inlet flow nozzle	Capacitance pressure sensors (MKS Instruments, Baratron type 221A)	Eight static pressure taps at each flow nozzle are configured to sense an average static pressure difference.
Wp outlet flow nozzle	Capacitance pressure sensors (MKS Instruments, Baratron type 221A)	Two static pressure taps at each flow nozzle are used to sense a static pressure difference.
Wp_p, Wp_r	Capacitance pressure sensors (MKS Instruments, Baratron type 221A)	Five static pressure sensors for each flow stream are used to measure the static pressure difference across each side of the dehumidifier.
T_1, T_2, T_3, T_4	Type T thermocouple	An array of four thermocouples connected in parallel is used to obtain an area-weighted average at each sampling location.
w_1, w_2, w_3, w_4	Dew point hygrometers (General Eastern, model 1100 DP/1111D)	The bulk average humidity ratios at each location are obtained by mixing air sampled at four points across the duct cross section.
p_7 or p_{amb}	Capacitance pressure sensor (MKS Instruments, Baratron type 220A)	
N	Optical encoder (BEI Model E25AB)	The encoder is mounted on the drive motor and outputs 1000 pulses per motor revolution to an HP counter card.

measuring junction to reduce the conduction errors to less than 0.01°C. The flow duct was insulated to reduce radiation errors to less than 0.5°C.

Temperatures were inferred by measuring the thermocouple electromotive force (emf) through a digital voltmeter referenced to an electronic 0°C (emf) put out by the voltage card (HP model 44422A) in the HP3497A.

A polynomial recommended by the National Bureau of Standards (NBS) was used to convert the measured emf to temperature (Benedict 1977):

$$T = +2.5661297 \times 10 \times E - 6.1954869 \times 10^{-1} \times E^2 + 2.2181644 \times 10^{-2} \times E^3 - 3.550000 \times 10^{-4} \times E^4 ,$$

where

T = temperature, in °C

E = emf, in mV.

This equation yields temperatures to within ±0.2°C. The combined overall uncertainty in the air temperature measurement is estimated to be ±0.6°C.

2.2.2.2 Air Humidity

Air humidity levels were monitored using dew-point hygrometers (General Eastern, models 1100DP/1111D). These instruments operate by monitoring the temperature of a chilled mirror surrounded by the sampled air. The mirror is chilled in a controlled fashion to induce vapor condensation on the mirror's surface. The onset of condensation is sensed optically by reduced reflectivity. The mirror's temperature is monitored by a platinum resistance thermometer. Four sensors were used to monitor the dew points of the two inlet and outlet streams. The sensors were calibrated by the manufacturers, with a resulting dew-point-temperature uncertainty of ±0.4°C.

The measured dew point temperature, T_{dp}, is then converted to an absolute humidity level in the sampled air stream by

$$w = 0.622 \frac{f_{ws}\, p_{sat}(T_{dp})}{p_t - p_{sat}(T_{dp})} ,$$

where

f_{ws} = fugacity of water vapor in air at saturation

T_{dp} = dew-point temperature (°C)

w = humidity ratio (kg/kg)

$p_{sat}(T_{dp})$ = saturation pressure of water vapor at the dew-point temperature (Pa)

p_t = total absolute pressure (Pa).

The saturation pressure as a function of T_{dp} is correlated as (Maclaine-cross 1974)

$$P_{sat} = \exp\left(23.28199 - \frac{3780.82}{T_{dp}} - \frac{225805}{T_{dp}^2}\right)$$

for $0 < T_{dp} < 100^oC$, and

$$P_{sat} = \exp\left(28.87 - \frac{6133.8}{T_{dp}}\right)$$

for $T_{dp} < 0^oC$.

Uncertainty in the derived absolute level of humidity results from incomplete mixing of the outlet air streams, errors in the temperature measurement, calibration errors, errors in the measurement of total absolute pressure, and errors in the saturation pressure correlation. For the present tests, errors in the absolute humidity level are estimated to be approximately ±3%.

2.2.2.3 Static Pressure

Pressure measurements are required for (1) pressure drop characteristics of the wheel, (2) pressure differences across the dehumidifier seals that cause leakage, (3) pressure differences across flow nozzles to calculate flow rates, and (4) ambient absolute pressure for air density and humidity ratio calculations.

Capacitance pressure sensors are used (MKS Instruments, Baratron type 221A) for differential pressure measurements and have a range of 0-250 Pa (0-10 in.) of water. These sensors put out a voltage signal linearly proportional to a pressure difference. The test loop uses six sensors: four to monitor the pressure differences across the flow nozzles in the inlet and outlet air streams, and two to monitor the pressure difference across each side of the dehumidifier.

We checked the calibration of these instruments by comparing them with a Hooke gauge manometer (Dwyer Instruments, Microtector) with a resolution of ±0.0002 in. of water. The results showed a typical differential pressure error of less than ±0.5%.

Again, we use a capacitance sensor to monitor the ambient absolute pressure (MKS Instruments, Baratron type 220A). This sensor was checked against a calibrated aneroid barometer with a resolution of 0.2 torr in the SERI Instrumentation/Metrology Center. Considering temperature effects on the pressure measurement, the uncertainty in the measurement is less than ±1%.

2.2.2.4 Air Flow Rate

Air flow rate in each stream was inferred through measurement of the pressure difference across standard ASME long-radius flow nozzles. The nozzles were installed in the flow stream with straight pipe lengths upstream and downstream of ten and five diameters, respectively, to conform to the ASME standards.

The air flow rate through the nozzle is given by Benedict (1977):

$$\dot{m} = C_d \frac{A_2 P_1}{\sqrt{RT_1}} \left(\frac{2\gamma}{\gamma-1}\right) \left[\frac{(r^{2/\gamma} - r^{(\gamma+1)/\gamma})(1 - r^{(\gamma+1)/\gamma}\ \beta^4)}{(1 - r^{2/\gamma}\ \beta^4)^2}\right]^{1/2} ,$$

where

$\dot{m}$ = air mass flow rate (kg/s)
C_d = nozzle discharge coefficient
A_2 = nozzle exit area (m^2)

R = gas constant for air, = 0.287 kJ/kg K
β = nozzle diameter ratio, = nozzle exit diameter/nozzle inlet diameter
T_t = upstream stagnation temperature (K)
γ = ratio of specific heats for air (taken to be 1.4)
p_1 = static pressure measured at one duct diameter upstream of nozzle (Pa)
p_2 = static pressure measured at one-half duct diameter downstream of nozzle (Pa)
r = static pressure ratio, = p_1/p_2.

Based on a number of comparisons, Benedict (1966) recommends the use of the following expression for the long radius flow nozzle discharge coefficient:

$$C_d = 0.19436 + 0.152884 (\ln R_d) - 0.0097785 (\ln R_d)^2 + 0.00020903 (\ln R_d)^3 ,$$

where

R_d = Reynolds number for the air flow at the nozzle throat.

The nozzle Δp was measured with a differential pressure transducer. Four static pressure taps at each upstream and downstream location were configured circumferentially equally spaced, to sense Δp. Uncertainty in the air flow measurement was estimated by procedures outlined by Benedict (1977, p. 479). The overall uncertainty in the airflow measurement is ±3.6%.

3.0 THE TEST ARTICLES

3.1 Rotary Dehumidifiers

A spirally wound, parallel-passage design using silica gel as the desiccant was chosen as the first geometry for the rotary dehumidifier. A photograph of this test article (test article 2) is shown in Figure 3-1. This design is similar to the prototypes tested earlier at SERI under transient conditions (Schlepp and Barlow 1984).

The desiccant used in this test article is Grade 11 Silica Gel, manufactured by Davison Chemicals, a division of W. R. Grace and Co., Baltimore, Md. Approximately 30 kg of silica gel with a particle-size range of 75 μm was crushed and sieved to yield about 15 kg of gel in a size range of 150 to 297 μm. This desiccant was then attached to a substrate

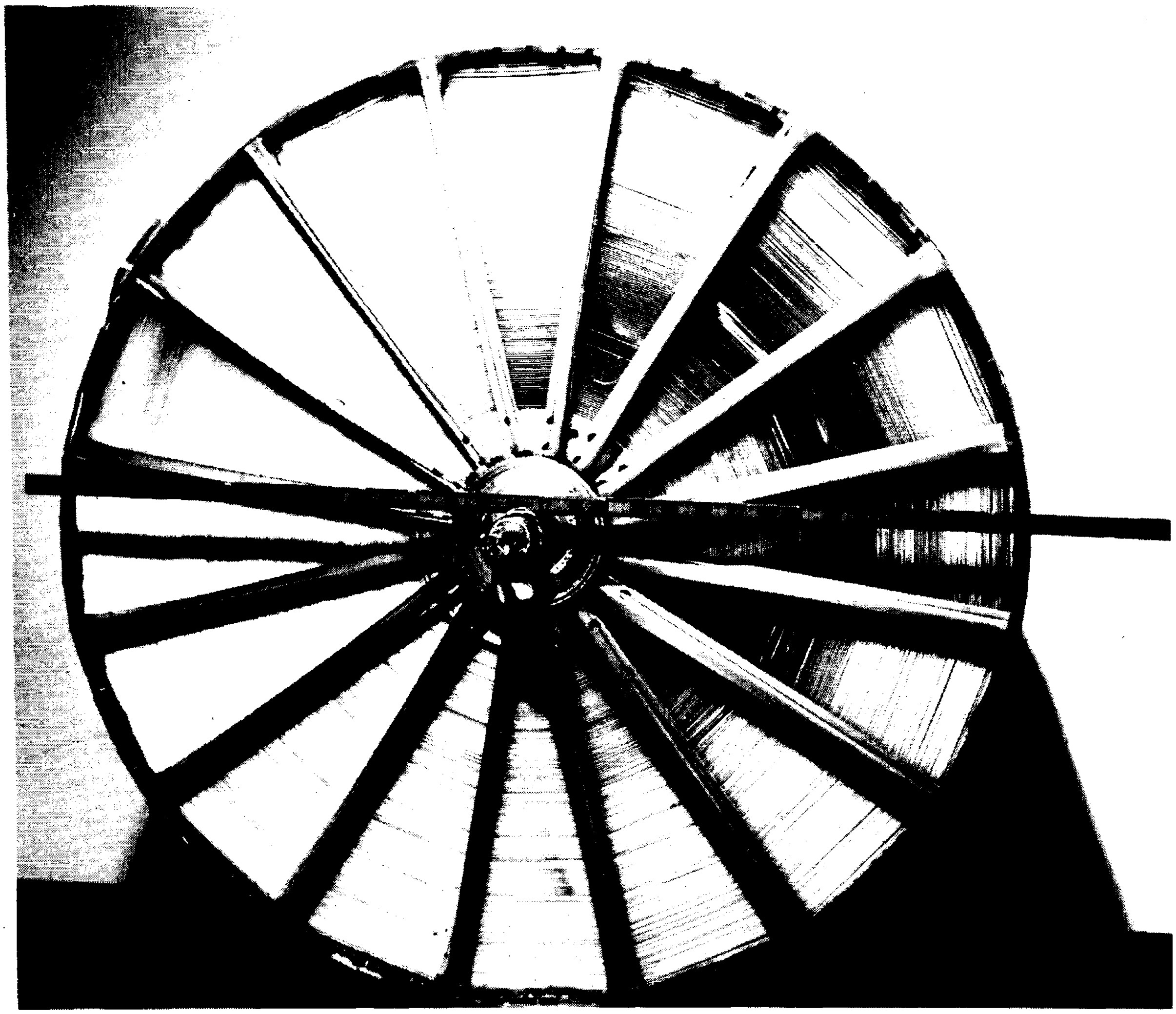

Figure 3-1. Rotary Desiccant Dehumidifier Test Article 2: Frontal View Showing Face Flange and Housing

polyester tape (Adhesives Research, Inc., Model ARclad 5190) nominally 25 μm thick, covered with adhesive 25 μm thick on both sides. About 400 m of the coated tape with a nominal width of 200 mm was forwarded to Rotary Heat Exchangers* Pty. Ltd. of Bayswater, Victoria, Australia, for incorporation into the dehumidifier test articles.

The coated, silica-gel-laden tape was initially wound under tension in a manner similar to that used in the manufacture of heat exchangers. However, because of the large variation in particle sizes used in coating the tape, compressive forces generated by the outer layers crushed the gel between spacers and caused significant radial movement of inner layers. Tension in the inner tape layers was significantly reduced, resulting in tape sagging and nonuniform gap spacing, as shown in the photograph in Figure 3-2. This test article was delivered to SERI in early 1985. Despite the deficiencies of this test article, labeled test article 1, a series of tests was conducted to bracket its performance "as is." These tests were carried out by Schultz (1986).

Later, this wheel was rewound to improve the uniformity of the passage spacing, primarily so that a practical data base could eventually be developed for comparing experimental results with existing analytical predictive models. This time, the wheel was wound at SERI so that adequate countermeasures could be taken to increase the effective radial stiffness of the spokes, should further problems arise.

To prevent radial movement of the inner layers, the radial compressive stiffness of the windings had to be increased by a considerable margin. Among the many alternatives considered, we decided to attach the spacers to each other and to the radial spoke with minute quantities of epoxy. About 30 to 50 windings were made before the epoxy was allowed to set overnight. The winding process of adding layers to the wheel took approximately 2 weeks to complete. A close-up view of the rewound wheel, labeled test article 2, is shown in Figure 3-3. The uniformity of the air passages was improved considerably from that achieved in earlier attempts, as illustrated in Figure 3-2. However, the passages are still far from uniform, as tests on pressure loss indicate (see Section 5.1).

The cause of the inadequate radial stiffness was analyzed in a fundamental fashion. Uniformity in passages can be assured provided the maximum particle size is less than 105 μm and the tape tension during winding is kept uniform and as high as possible. Following these principles, we have fabricated a third test article at SERI.

Tables 3-1 and 3-2 provide a summary of the relevant dimensions and masses of test articles 1 and 2, respectively. The major differences between the two test articles are the improved air passage spacing, as illustrated in Figures 3-2 and 3-3, and the revised estimates of desiccant and substrate masses.

3.2 Housing and Seals

The housing for the rotary dehumidifier was made of a cylindrical, 4.5-mm-thick sheet steel enclosure. Front and back flanges fitted with self-aligning bearings provided the support for the rotor and face plates for the seals incorporated along each spoke. A

---

*This firm possesses 20 years of reputable experience in fabricating Mylar tape parallel-passage rotary heat exchangers up to 2.5 m in overall diameter. Its heat-exchanger design and fabrication methods were adapted to the fabrication of the first high-performance dehumidifier test articles.

Figure 3-2. Rotary Desiccant Dehumidifier Test Article 1

circumferential clearance of approximately 5 mm between the rotor and the enclosure was maintained to allow free rotor movement.

The seal design used on our dehumidifiers is similar to that used previously by Rotary Heat Exchangers and consists of radial seals that prevent leakage between air streams and circumferential seals that prevent air from flowing around the dehumidifier between the wheel cover and the outer housing.

Figure 3-3. Close-up View of Air Passage in Test Article 2

Table 3-1. **Dimensions and Masses of Dehumidifier Test Article 1**

Description		Quantity
Outside diameter		0.8 m
Hub diameter		0.2 m
Passage depth		0.203 m
Number of spokes		16
Spacer dimensions	- thickness	1.18 mm
	- width	4.3 mm
Number of windings		178
Gel particle size range		180-350 μm
Sheet thickness (with gel)		0.58 mm
Passage width, average		1.04 mm
Sheet-to-sheet spacing, average		1.62 mm
Coated tape density (dry)		0.37 kg/m^2
Dry silica gel fraction		0.745
Mass of dry gel/period		7.35 kg
Mass of tape/period		2.56 kg
Face area/period		0.215 m^2

The radial seals consist of a 76-μm-thick polyester film attached to the spokes that contacts the seal plate. The contact area is such that at least one seal is always in contact with the seal plate. The seal plate width is set to make-before-break contact between two adjacent seals. The circumferential seals are made of the same polyester film but are serrated to prevent the seal from buckling and to ensure contact with the rim. Figure 3-4 shows the details of the seal design. Improved seal designs with less leakage and resistance to rotation are perhaps possible, but this is beyond the scope of this research.

3.3 Rotor Drive Arrangement

The rotor is friction-driven by a 20-cm, rubber-rimmed drive wheel to contact the dehumidifier cover. A slot 8 cm wide and 15 cm long cut in the housing enclosure allows the drive wheel to contact the dehumidifier directly. The drive wheel is driven by a dc motor via a set of gear-reduction units to allow wide variation in the wheel speed.

A photograph of dehumidifier test article 2, with its housing and face flange, is shown in Figure 3-5.

Table 3-2. Dimensions and Masses of Dehumidifier Test Article 2

Description	Quantity	Units	Remarks
Dimensions			
Outer diameter (nominal)	809.60	mm	Measured
Winding outer diameter	799.06	mm	Measured
Hub outside diameter	197.94	mm	Measured
Winding length along spoke	300.56	mm	Measured
Number of spokes	16		Measured
Number of tape windings	168		Measured
Spacer width	4.318	mm	Measured
Spacer thickness	1.180	mm	Measured
Tape spacing	1.755	mm	Average over the wheel
Silica gel particle size range	150 to 297	μm	50 to 80 mesh
Uncoated tape thickness	0.075	mm	Mylar tape and two adhesive layers
Tape width	203.2	mm	Measured
Nominal coated tape thickness	0.669	mm	Tape plus twice the maximum particle size
Nominal air passage gap	1.086	mm	Calculated
Total wheel frontal area (nominal)	0.515	m^2	Calculated
Total wheel midsection flow area	0.437	m^2	Depends on the assumed
Total wheel tape area	53.326	m^2	particle size
Total wheel exposed transfer area	50.967	m^2	Calculated
Flow cross-sectional area per period	0.213	m^2	Without blockage due to tape thickness
Transfer area per period	24.849	m^2	Calculated
Carry-over volume	0.077	m^3	Calculated
Masses			
Total mass of wheel	40.406	kg	Measured (±3%)
Coated dry tape surface density	0.383	kg/m^2	Measured (±3%)
Uncoated dry tape surface density	0.086	kg/m^2	Measured (±3%)
Dry silica gel fraction	0.776		Calculated
Coated tape total mass	20.424	kg	Calculated
Uncoated tape total mass	4.575	kg	Calculated
Total silica gel mass	15.848	kg	Calculated
Exposed silica gel mass	15.147	kg	Calculated
Mass of dry desiccant per period	7.574	kg	Calculated

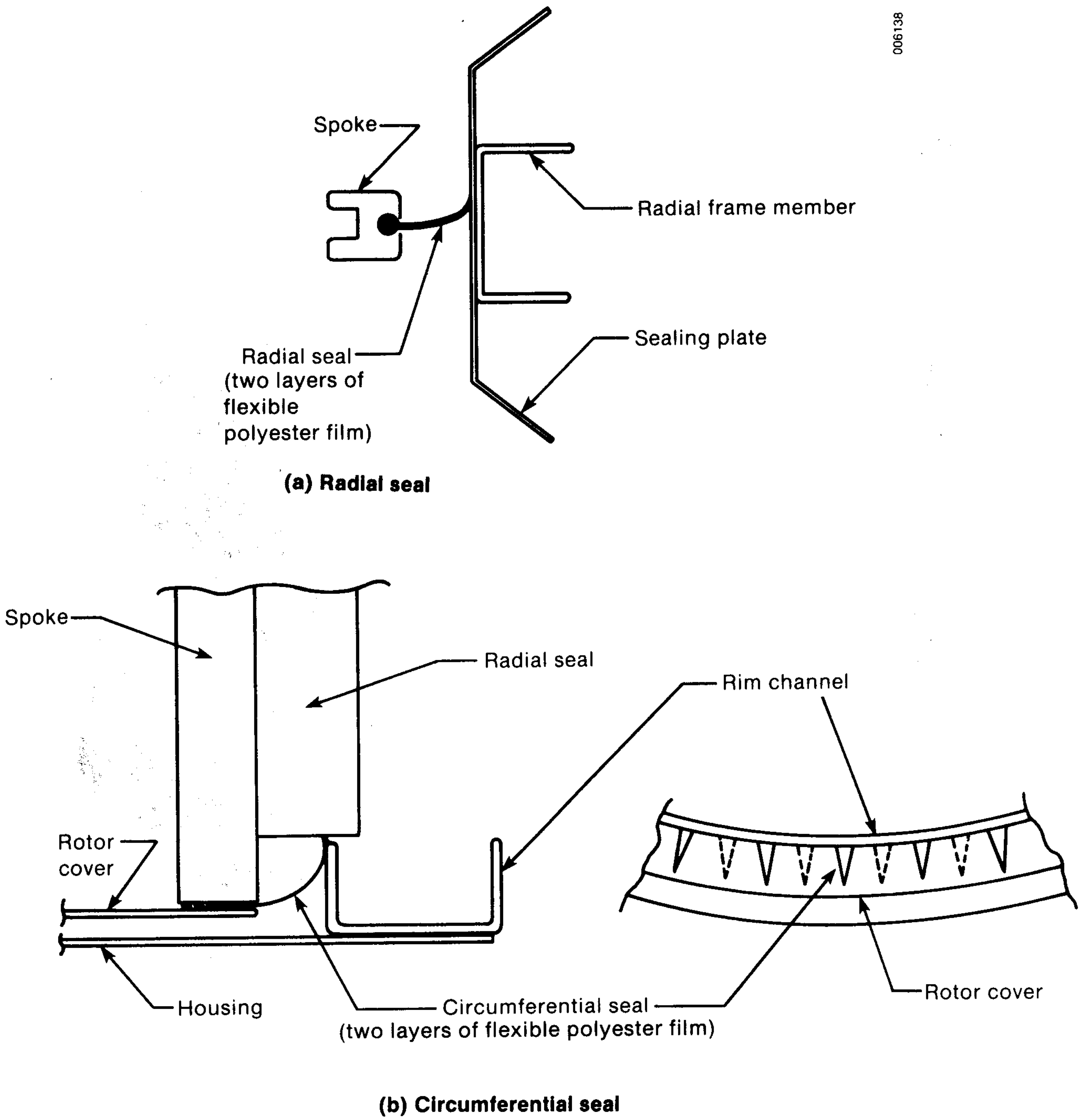

Figure 3-4. Details of Circumferential and Radial Seals

Figure 3-5. Test Article 1 Installed in the Cyclic Test Facility

4.0 THE EXPERIMENTAL PROCEDURE

To operate the Cyclic Test Facility (CTF), a carefully chosen procedure was adopted and followed to ensure the safety of the personnel and to generate consistent, accurate sets of data. When the test conditions for a particular run are specified in terms of the process and regeneration stream flow rates, inlet temperatures, humidities, and the wheel rotational speed, wheel rotation is initiated. The inlet conditions are entered into the central computer and the acquisition/control program is started. Automatic controls of the loop bring up the air stream flow rates and temperatures. The humidity of the incoming air streams must be controlled manually. The status of the loop variables is continually updated on the computer monitor at 10-second intervals to visually indicate the test status.

In addition, continuous traces of temperatures and humidities are recorded on a strip chart. Approximately 30 to 40 minutes are allowed to attain steady-state inlet conditions. Depending on the wheel rotational speed, the outlet conditions reach steady state over a maximum period of 2 hours, which can be inferred from steady strip-chart traces.

At this point, a steady-state data-gathering routine is initiated. All test variables are read and recorded on a floppy diskette at 60-second intervals. Continuous updates of enthalpy and mass balance errors are provided on the monitor. The operator monitors these errors to ensure that overall errors are within ±2%. The steady-state data-gathering routine is allowed to persist over a minimum period of 15 minutes. Special precautions are taken for the low- and high-speed tests. For low-speed tests, the entry of each spoke from process to regeneration results in periodic variations in outlet states. The operator begins and ends the data gathering over a minimum of four full cycles of these variations to ensure that true average outlet conditions are recorded. For high-speed tests, the approach of the matrix to a steady state is extremely slow. The associated time constant may be in hours. It is thus essential that the test be continued over four hours, and that the fluctuations in inlet conditions be kept minimal. Additional operational details for the CTF are provided in Appendix H.

5.0 EXPERIMENTAL RESULTS AND DATA ANALYSES

The raw experimental data are distorted by finite leakage out of the housing, cross-leakage between the streams, and carry-over, especially at high rotational speeds. Seal leakages at the housing are characterized by procedures described in Appendix E. Raw data are then processed according to procedures described in Appendix G to arrive at true rotor inlet and outlet conditions for further heat- and mass-transfer analyses.

In this section, further processing of the corrected data and accompanying results and discussions are provided. Section 5.1 describes the pressure-loss characterization and Section 5.2 the heat- and mass-transfer characterization of test article 2.*

5.1 Pressure-Loss Tests

To determine the rotor pressure-loss characteristics, we conducted two independent series of tests. For the first series, the rotor was configured in its housing and seals as in dehumidification applications with two counterflowing streams, each flowing through one-half of the rotor. For the second series, the rotor was removed from its housing and front and back flanges, and configured as shown in Figure 5-1 with a single stream of air flowing through the entire wheel, free from any other obstructions. This configuration is denoted as open rotor in the following sections. A wide range of air flows at a particular room temperature and humidity was used for all the pressure-loss tests. The two series of data were analyzed separately, following procedures outlined by Maclaine-cross and Ambrose (1980).

5.1.1 Data Analyses

Case 1: Open Rotor. The flow through the rotor is modeled as depicted in Figure 5-2. Stations 1 and 4 represent the locations of the static pressure taps used to measure the pressure difference. Stations 2 and 3 represent locations just upstream and downstream of the air flow through the matrix. True static pressure loss through the rotor, represented by $p_2 - p_3$, is expressed as

$$p_2 - p_3 = (p_1 - p_4) - (p_1 - p_2) - (p_3 - p_4) \ . \tag{5-1}$$

Here, $p_1 - p_2$ represents the initial contraction loss as the air acceleration into the matrix, and $p_3 - p_4$ represents an exit loss. The entrance loss is expressed as

$$p_1 - p_2 = \frac{\rho_2 u_2^2}{2} \left[1 - \left(\frac{A_c}{A_d}\right)^2\right] \ , \tag{5-2}$$

where A_c is the minimum cross-sectional area at station 2 and A_d is that of station 1. For open-rotor tests, the ratio (A_c/A_d) is essentially zero.

---

*The data analysis carried out in this report relies heavily on the analogy method for modelling dehumidifier performance. For a detailed understanding, it is suggested that the reader become familiar with the analogy method. Since the method is fairly detailed and has been documented in the literature, a formal introduction to the analogy method would be beyond the scope of this report.

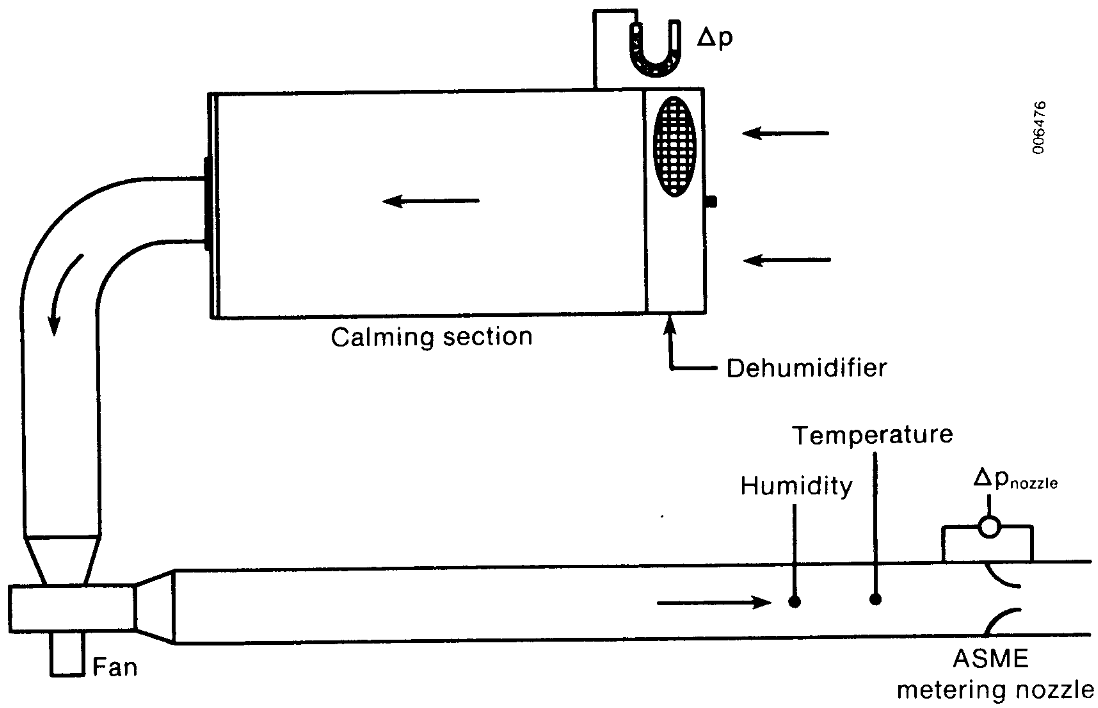

Figure 5-1. Open-Wheel Pressure-Loss Test Configuration

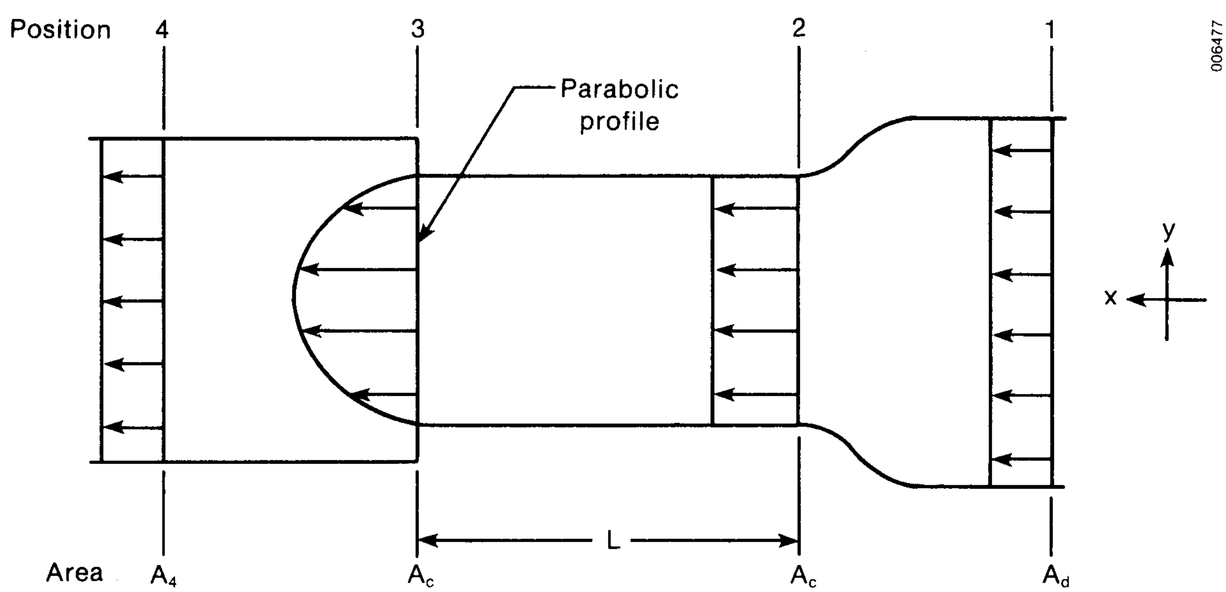

Figure 5-2. Assumed One-Dimensional Flow through the Dehumidifier Matrix for Calculating Inlet and Outlet Pressure Drop

The exit pressure loss is associated with an abrupt expansion in flow area and a change in the flow velocity profile from parabolic to essentially uniform (Maclaine-cross and Ambrose 1980). This loss is expressed as

$$p_3 - p_4 = \frac{\rho_3 u_3^2}{2} \{2 \left(\frac{A_c}{A_4}\right)^2 - 2.4 \left(\frac{A_c}{A_4}\right)\} . \tag{5-3}$$

Here, A_4 represents an area equivalent to the flow area free of velocity defects. In effect, it is the total area available for flow minus the frontal projected areas of large obstructions, such as those of the spokes and the hub. For the open wheel, the following areas were arrived at from the geometry:

$$A_c = \left(\frac{b}{a + b}\right) A_{ref} , \tag{5-4}$$

where

- b = the average air passage gap; $b = 1.755$ mm.
- a = an effective coated tape thickness, taken to be the sum of the nominal uncoated tape thickness and twice the largest particle screen size; $a = 0.075 + 2(0.297), = 0.669$ mm.
- A_{ref} = a reference flow area equal to the entire flow cross section at the rotor midsection; $A_{ref} = 0.4369$ m^2.
  A_4 was inferred to be 0.3792 m^2.

Using Eqs. 5-1 through 5-3, we calculated the true Δp, $p_2 - p_3$. This pressure difference was then normalized as $\Delta p D_h/2\mu uL$ and plotted as a function of the dimensionless parameter $ReD_h/4L$. Here, D_h represents an effective hydraulic diameter of the collective air passages, u is the air velocity through the passage, μ is the mean air dynamic viscosity, Re is the Reynolds number based on the hydraulic diameter, and L is the matrix depth.

Case 2: Counterflowing Stream. The analyses here follow the same procedure outlined above, except for estimations of varied areas for A_c, A_d, and A_4 for counterflowing streams.

A_d, representing the cross-sectional area of the upstream ducting, was calculated to be 0.185 m^2. A_c represents one-half of its value for the open-rotor case minus an "effective" shadow area depicting blockage of the front and back sealing surfaces. Since the air flow takes a path around these sealing surfaces, the shadow area is smaller than the projected sealing surface area. Based on experiments with rotary heat exchangers with similar designs, Maclaine-cross and Ambrose (1980) recommend that the shadow area be taken as the sealing surface area with its width reduced by 1.7 times its sealing lip, as indicated in Figure 5-3.

For the rotor being examined, with a seal lip of 0.0254 m, the resulting A_c was calculated to be 0.132 m^2. A_4, as before, was the exit duct cross-sectional area minus the projected areas of the spokes and hub. Here, $A_4 = 0.149$ m^2. Once again, the calculated $p_2 - p_3$ was made dimensionless as $\Delta p D_h^2/2\mu uL$ and plotted as a function of $ReD_h/4L$ for each counterflowing stream.

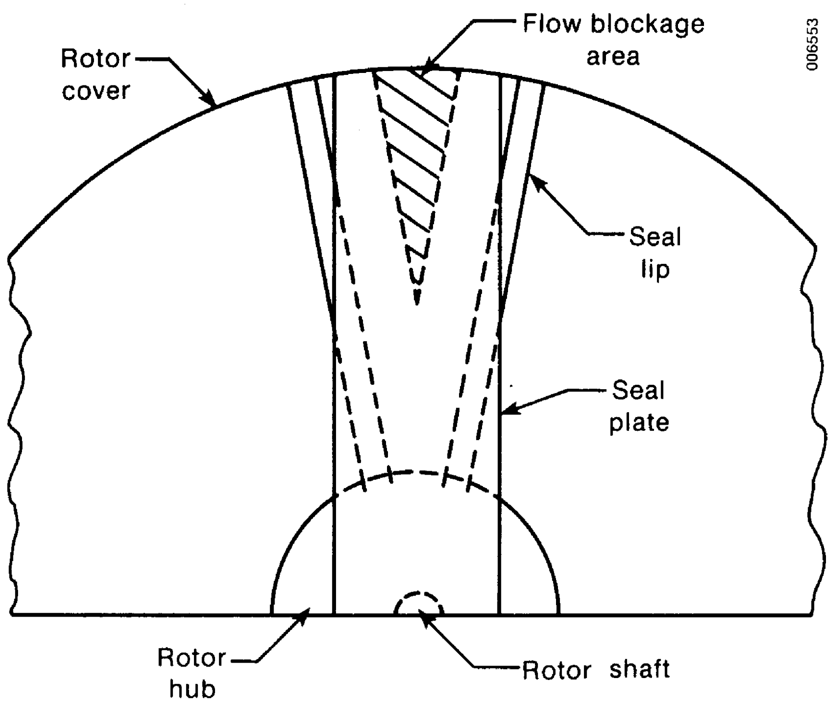

Figure 5-3. Masked Shadow Area Behind Front and Back Seal Plates

5.1.2 Pressure-Loss Test Results

The reduced data from open-rotor and counterflowing stream tests are shown in Figure 5-4. The measured $\Delta p D_h^2/2\mu uL$ varies from about 16.7 to 20 over an $ReD_h/4L$ range of 0.1 to 0.7. The scatter in the data is somewhat large, about ±7%. Despite the scatter, a definite trend of $\Delta p D_h^2/2\mu uL$, increasing with the abscissa, can be seen. A linear curve fit to the data indicates the following functional relationship:

$$\left(\frac{\Delta p D_h^2}{2\mu uL}\right) = 16.8 + 3.96\left(\frac{ReD_h}{4L}\right) .$$

In laminar flow for perfectly uniform parallel passages of infinite width, theoretical values for the slope K and intercept fRe are given by Cornish (1928), Lundgren et al. (1964), and Kays and London (1984), respectively, as K = 0.686, and fRe = 24. Here, f represents the Fanning friction factor. For rectangular passages of finite aspect ratio (b/w = 0.01436, for test article 2), fRe decreases to 23.538.

However, we note that the theoretical values are far from the experimentally inferred values. The cause for these discrepancies was identified as the nonuniform passage spacing of the tested matrix. The effect of nonuniformity in gap spacing is readily taken into account, provided that a probability distribution of the gap spacing is known, as follows.

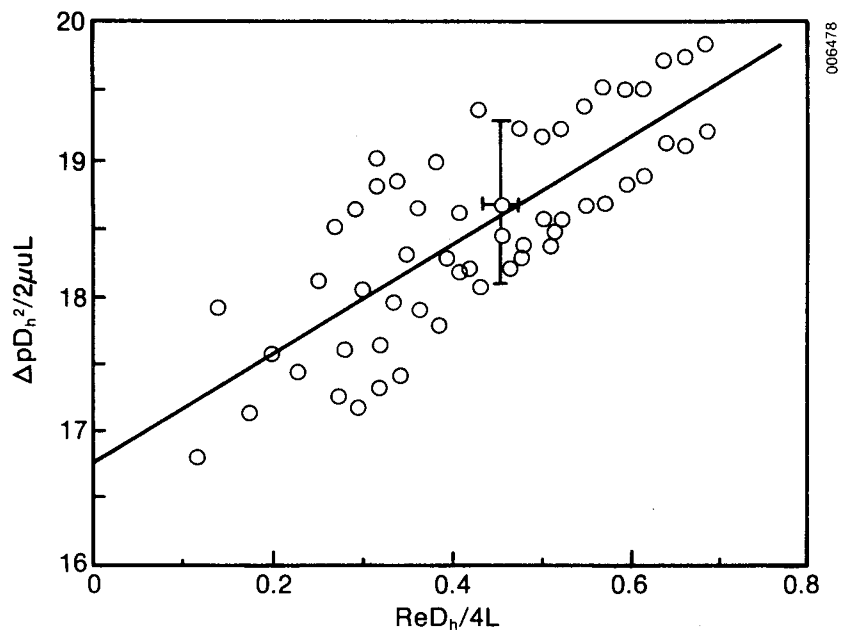

Figure 5-4. Dimensionless Pressure-Loss Variation with Reynolds Number for Test Article 2 and the Least-Squares Curve Fit

To reconcile the differences in the measured and theoretical values of the slope and intercept, we assumed a simple probability distribution for the gap spacing. A fraction $(1 - p_f)$, with p_f in the range $0 < p_f < 1$, of the passages was assumed to be at the nominal design gap. The remaining fraction p_f of the passages was assumed to be uniformly distributed symmetrically around the design gap, over a range of gap widths $(R_m - 2)$ to R_m times the design gap, with R_m in the range $1 < R_m < 2$.

Using the two parameters p_f and R_m to represent the gap distributions, we calculated the laminar-flow limits for fRe, K, and an effective Nusselt number Nu. Further details of these calculations are provided in Appendix F.

To match the experimental values of the intercept (16.8) and slope (3.96), we found the choices for the two parameters to be $p_f = 0.48$ and $R_m = 1.92$. The implications of these values are that only 52% of the passages of the matrix turned out to be at the design gap, and the remaining 48% of the passages possessed gap widths uniformly distributed in a range from 0.08 to 1.92 times the design gap.

The inferred probability distribution also implied that the effective Nusselt number for the matrix would be 31% of its value for a uniform gap spacing limit of $Nu_{pp} = 8.235$, at constant heat flux. This result was later verified during the heat and mass exchange tests described in the following sections. The measured Nu from the later tests indicated a value of 54% of the limiting Nu_{pp}, essentially confirming that the matrix did indeed possess nonuniform gap spacing and that the assumed simple probability distribution represented the actual case rather well.

The effect of a nonuniform passage distribution is to decrease the pressure-drop intercept and increase the slope dramatically, as plotted in Figure 5-4. An additional influence is to reduce the Nusselt number intercept when plotted versus a Graetz number, as shown in the following section.

5.2 Heat- and Mass-Transfer Tests

A series of tests to study heat and mass transfer was conducted over a wide range of process and regeneration inlet conditions and matrix rotational speeds. The data were gathered over 2 months of continuous testing. The heat- and mass-transfer data were analyzed using linear and nonlinear analogy theories (Maclaine-cross 1974; Banks 1985). For the analysis, the tests were categorized into high-speed, low-speed, and medium-speed tests. The following sections describe each of these. In each section, the data processing and analysis method is described first. Experimental results, comparisons with theory, and discussions follow. A complete set of experimental data is provided in Appendix B, and a description of the measurement uncertainties in Appendix A. Relevant desiccant and matrix properties for reducing the test data are summarized in Appendix D.

5.2.1 High-Speed Tests (C_{1p}, C_{2p} >> 1)

As the wheel rotational speed becomes very high (i.e., $C \to \infty$), the transfer effectiveness of the matrix η approaches an asymptotic limit that is governed by the heat- and mass-transfer rates within the matrix. The actual capacities of the matrix for heat and mass transfer do not affect the effectiveness significantly. Thus, by processing the high-speed-test data alone, we are able to arrive at the effective Nusselt and Lewis numbers for heat and mass exchange, respectively.

5.2.1.1 Data Analysis

To process the high-speed-test data, we adopted the following procedure.

- The effective fraction of silica gel in the matrix was assumed to be unity.
- The experimental data were sorted to select experimental conditions when $C_{1p} > 4$. Since C_{2p} is always greater than C_{1p}, the selection ensured that the dimensionless rotational speeds for both F_1 and F_2 transfer were almost independent of the capacity rate ratios.
- At high speed, since all the states within the matrix lie along a straight line connecting the process and regeneration inlet states, a mean matrix state is defined with a temperature

$$t_m = \left(\frac{t_{pi} + t_{ri}}{2}\right) \tag{5-5}$$

and a humidity ratio

$$w_m = \frac{(w_{pi} + w_{ri})}{2} \; . \tag{5-6}$$

The slope α_i is defined as

$$\alpha_i = -\left(\frac{\partial t}{\partial w}\right)_{F_i} \; , \tag{5-7}$$

and the specific capacity ratio γ_i is defined as

$$\gamma_i = \frac{\partial W}{\partial w} + \frac{\partial W}{\partial t} / \frac{\partial w}{\partial t}\Big|_{F_{3-i}} \; ; \tag{5-8}$$

they are calculated for i = 1 and 2 for the matrix, assumed to be in equilibrium with the mean air state defined by t_m and w_m.

- Assuming that both α_1 and α_2 are constants, the intersection point for the process condition is calculated by extending lines of constant F_i with their corresponding slope α_i.
- The process outlet condition as found from the experiment is corrected for experimental errors by averaging the process outlet conditions (temperature and humidity) with those arrived at from regeneration outlet conditions, and imposing mass and energy balances for the wheel.
- With the corrected process outlet condition, the effectiveness for temperature and moisture transfer are calculated as

$$\eta_t = \frac{t_{po} - t_{pi}}{t_{pi} - t_{ri}} \quad (5\text{-}9)$$

and

$$\eta_w = \frac{w_{po} - w_{pi}}{w_{pi} - w_{ri}} , \quad (5\text{-}10)$$

respectively.

- The corresponding capacity rate ratios or dimensionless wave speeds C_i for the process stream are calculated as

$$C_i = \frac{m_{dd}\ \gamma_i\ x_{eff}}{\dot{m}_p\ \tau} , \quad (5\text{-}11)$$

where

m_{dd} = the initially estimated amount of dry desiccant per period (kg)
γ_i = the specific capacity ratio
x_{eff} = the fraction of dry desiccant experimentally determined as effective
$\dot{m}_p$ = the process dry air flow rate (kg/s)
τ = the contact time (s), $= \frac{3600}{(2N)}$, where N is the wheel rotation speed, in rev/hr.

- Since C_i values are finite, the measured F_i efficiencies are incremented for infinite rotational speed as

$$\Delta\eta_{F_i} = \frac{k_3}{C_i^2} , \quad (5\text{-}12)$$

where k_3 has been determined to be approximately 0.09 [see, for example, Maclaine-cross (1974)].

- The corrections for finite wheel speed for F_i efficiencies are now converted to the temperature and moisture effectivenesses as

$$\Delta\eta_t = \left\{\frac{t_{pi} - t_{pint}}{t_{ri} - t_{pi}}\right\} \Delta\eta_{F_1} + \left\{\frac{t_{ri} - t_{pint}}{t_{ri} - t_{pi}}\right\} \Delta\eta_{F_2} \quad (5\text{-}13)$$

and

$$\Delta\eta_w = \left\{\frac{w_{pi} - w_{pint}}{w_{ri} - w_{pi}}\right\} \Delta\eta_{F_1} + \left\{\frac{w_{ri} - w_{pint}}{w_{ri} - w_{pi}}\right\} \Delta\eta_{F_2} . \quad (5\text{-}14)$$

- The corrected temperature and moisture effectivenesses are then converted to their corresponding number of transfer units (NTU) (Kays and London 1964) as

$$(NTU)_t = 1/\left[\frac{1}{\eta_t} - \frac{(1 + E_2)}{2}\right] \quad (5\text{-}15)$$

and

$$(NTU)_w = 1/[\frac{1}{\eta_w} - \frac{(1 + E_2)}{2}] \ , \qquad (5\text{-}16)$$

where E_2 represents the mass unbalance ratio between the process and the regeneration stream, defined as

$$E_2 = \dot{m}_p/\dot{m}_r \ . \qquad (5\text{-}17)$$

- An effective Lewis number, representing the ratio of overall resistance to mass transfer to that for heat transfer, is calculated as

$$(Le)_{eff} = \frac{(NTU)_t}{(NTU)_w} \ . \qquad (5\text{-}18)$$

- A mean overall Nusselt number is derived as

$$Nu = (NTU)_t \ Re_m \ Pr_m \ \{\frac{D_h}{2L}\} \ , \qquad (5\text{-}19)$$

where Re_m is the mean air Reynolds number,

$$Re_m = \frac{\rho_m \ C_m \ D_h}{\mu_m} \ ,$$

Pr_m is the mean air Prandtl number,

$$Pr_m = \frac{C_{p_m} \mu_m}{k_m} \ ,$$

and D_h is the hydraulic diameter of the passages (m).

Here, ρ_m is the air density, C_m is air velocity through the passage, μ_m is air dynamic viscosity, and k_m is the air thermal conductivity.

- The effective Lewis number can be expressed in terms of an efficiency of the desiccant particle-cum-substrate matrix e_s (Maclaine-cross 1974) as

$$Le = \frac{Sc}{Pr} \ \{1 + \frac{Sh}{60} \ (\frac{d_p}{D_h}) \ (\frac{1}{e_s \ p_F}) \ (\frac{\mu_m}{\rho_d D_W}) \ (\frac{dw}{dW})_t\} \ , \qquad (5\text{-}20)$$

where $(\frac{Sc}{Pr})$ represents the Schmidt-over-Prandtl-number ratio for air.

Sh = the Sherwood number
d_p = the mean desiccant particle size (m)
ρ_d = the dry desiccant density (kg/m^2)
p_F = the desiccant particle packing factor on the substrate
D_W = the diffusivity of moisture in the desiccant (m^2/s)

$(\frac{dW}{dw})_t$ = the isothermal rate of change of moisture in the desiccant with respect to the moisture content of the air, evaluated at t_m.

The efficiency e_s can be viewed as the ratio of surface area available for exchange to that if the particles were distributed as uniform spheres of diameter d_p, closely packed in a single layer. Note that the higher the e_s, the lower the solid-side resistance. From all the other parameters in Eq. 5-20, e_s, termed the "solid-side conductance geometry factor," is calculated.

The diffusivity of moisture in silica gel D_w is calculated by means of the formulation of Sladek et al. (1974) (see Appendix D), which yields estimates consistent with experimental values reported in the open literature.

5.2.1.2 High-Speed-Test Results

The results are plotted as the measured Nusselt number Nu versus a Graetz number Gr, defined as

$$Gr = Re\ Pr\ (D_h/4L) \tag{5-21}$$

in Figure 5-5. The measured Nusselt numbers remain essentially constant at 4.5 over a Graetz number range of 0.26 to 0.56.

Our earlier data on pressure drop indicate that for the assumed probability distribution for passage gaps, the Nusselt number should be 31% of the uniform-gap limit of 8.235. The experimental value is 54%, indicating that the assumed probability distribution is perhaps realistic. More accurate estimates of Nu are possible with more realistic assumptions on gap-size probability distributions.

The solid-side conductance geometry factor e_s (Eq. 5-20) is plotted as a function of the mean matrix temperature t_m in Figure 5-6 and of the mean air humidity ratio in Figure 5-7. The e_s varies from a low of 0.6 to a high of 1.6. No significant trend for

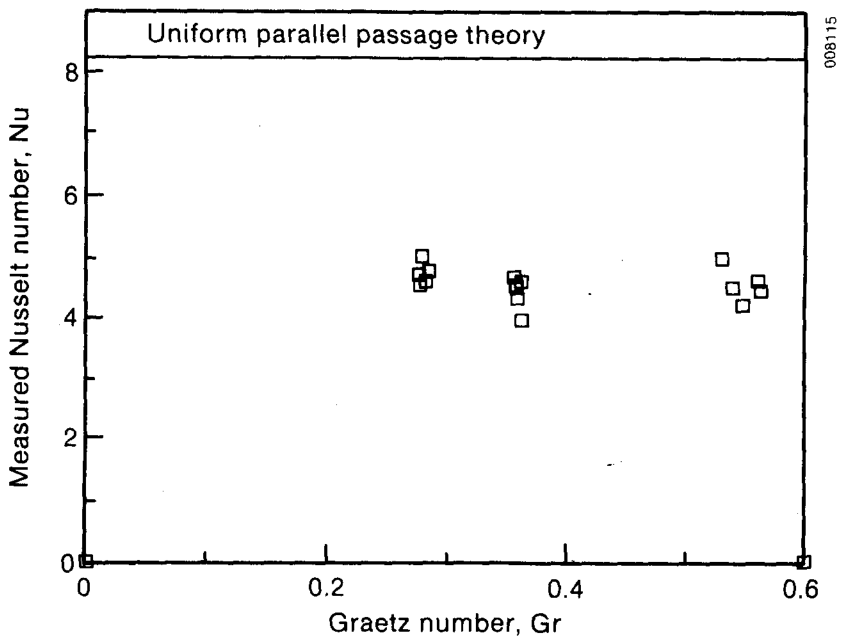

Figure 5-5. Measured Variation of Nusselt Number with Graetz Number

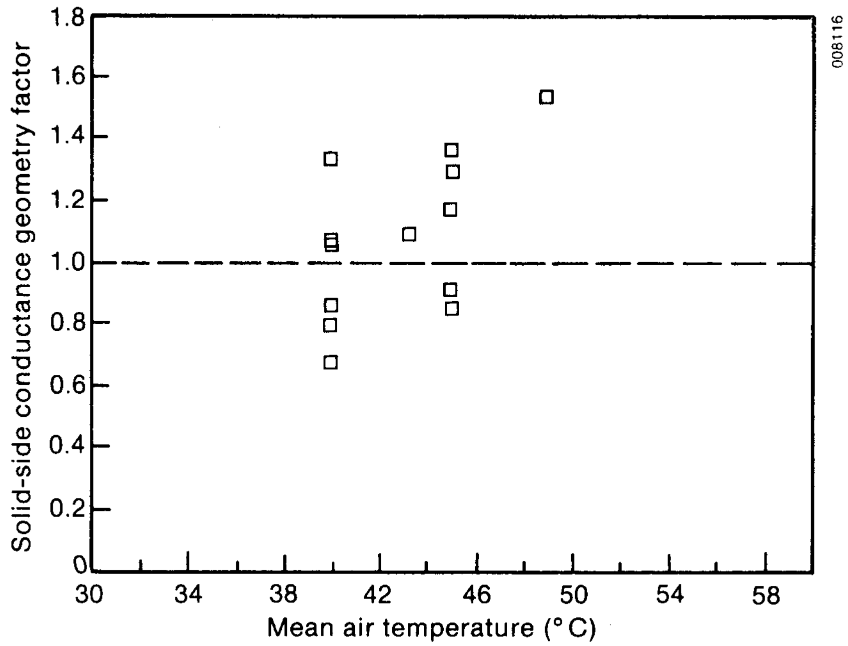

Figure 5-6. Measured Variation of Solid-Side Conductance Geometry Factor with Mean Matrix Temperature at Absolute Humidities Ranging from 8 to 16 g/kg

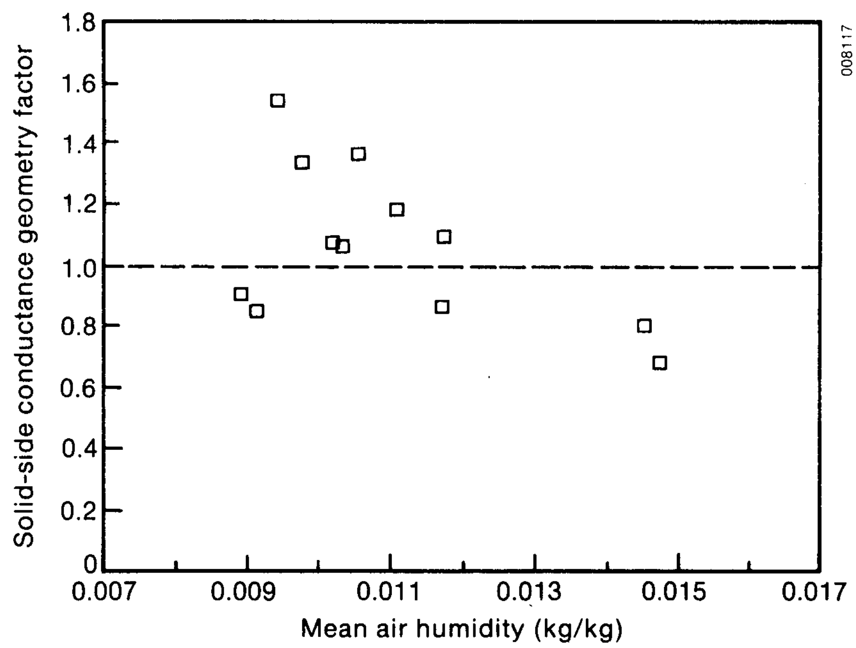

Figure 5-7. Measured Variation of Solid-Side Conductance Geometry Factor with Mean Air Humidity at Temperatures Ranging from 40° to 50°C

the variation of e_s with temperature or humidity could be discerned. The e_s data are widely scattered about a mean of approximately unity. For all practical purposes, a mean value of unity may represent the data well. Considering that the crushed silica gel particles were shaped more like parallelepipeds rather than spheres, values for this geometry factor over unity are acceptable. For the remainder of the data presented here, analyses were carried out with $e_s = 1$.

5.2.2 Low-Speed Tests (C_{1p} or $C_{2p} << 1$)

When the wheel rotates slowly, i.e., when the residence time of an element of the matrix is large compared with a typical time constant for heat or mass transfer, the transfer effectiveness is governed by the effective capacity of the matrix and is insignificantly affected by the heat- and mass-transfer rates. Thus, the low-speed tests provide a means for estimating the effective capacity of the wheel, both in terms of its active silica gel and effective overall heat capacity.

In general, for large NTUs (>8) and constant specific heats, the approximation $\eta_i = C_i$ holds good for $C_i < 0.7$. However, for $C_i > 0.5$, the F_i waves tend to spread within the matrix because of the varying capacity of the matrix from entry to exit, which results in significant reductions in the overall effectiveness. Maclaine-cross (1974) illustrates the effect of wave spreading by comparing an exact finite-difference solution with the analogy theory. For a capacity rate ratio variation of 2 (or 0.5) for balanced flow, the analogy theory overpredicts the effectiveness by as much as 15% for large NTUs, at wheel rotational speeds near unity. At present, only the linear variation of capacity has been captured (see Case 2) by a finite-difference solution similar to that of Lambertson (1958). Nonlinear effects still persist. Thus, we are forced to confine our low-speed data analyses to C_i values less than about 0.5.

However, as the rotational speed C decreases, the change between inlet and outlet states for either stream become smaller. Measurement uncertainties tend to propagate into the deduced effectivenesses, resulting in larger relative uncertainties. Thus, caution must be exercised in interpreting the low-speed-test data to arrive at effective capacities of the matrix.

5.2.2.1 Data Analysis

Case 1: Constant Matrix Specific Capacity. The following procedure was adopted to process the low-speed test data:

- The effective fraction of silica gel in the matrix is initially assumed to be unity (to be iteratively determined later), i.e.,

$$x_{eff} = 1.0 \ . \tag{5-22}$$

- The experimental data were sorted to select cases when C_{1p} or $C_{2p} < 1$, to estimate the capacities for heat or mass exchange, respectively.
- The process outlet condition as measured is corrected for experimental errors by averaging it with that arrived at from the regeneration outlet condition, imposing mass and energy balance for the wheel.
- The process and regeneration intersection points are calculated by integrating along lines of constant F_1 and F_2. The corresponding average specific capacity ratios $\bar{\gamma}_1$ and $\bar{\gamma}_2$ for the process stream are also obtained.

- The process effectivenesses for F_1 and F_2 transfer are calculated as

$$\eta_{2p} = \frac{(h_{po} - h_{pi})(w_{ri} - w_{pint}) - (w_{po} - w_{pi})(h_{ri} - h_{pint})}{(h_{pint} - h_{pi})(w_{ri} - w_{pint}) - (w_{pint} - w_{pi})(h_{ri} - h_{pint})} \qquad (5\text{-}23)$$

and

$$\eta_{1p} = \frac{(w_{po} - w_{pi})}{(w_{ri} - w_{pint})} - \eta_{2p}\frac{(w_{pint} - w_{pi})}{(w_{ri} - w_{pint})} . \qquad (5\text{-}24)$$

- The corresponding dimensionless wheel rotational speeds for the process stream are calculated as

$$C_i = \frac{m_{dd}\,\bar{\gamma}_i\,x_{eff}}{\dot{m}_p\,\tau} . \qquad (5\text{-}25)$$

- For both process and regeneration streams, mean Reynolds number, Prandtl number, and Graetz number are evaluated at their corresponding mean temperatures between inlet and outlet conditions.
- For each stream, mean Nusselt number is evaluated on the basis of the results of high-speed test data.

The corresponding NTU is evaluated as

$$NTU = Nu/Gr . \qquad (5\text{-}26)$$

- For each stream, the effective Lewis number is evaluated using Eq. 5-20.
- For F_1 and F_2 transfer, the dimensionless transfer coefficients are evaluated for both streams (Maclaine-cross 1974) as

$$\Lambda_i = \frac{(NTU)\left\{Le - \frac{\alpha_i}{\alpha_{3-i}}\right\}}{Le\left\{1 - \frac{\alpha_i}{\alpha_{3-i}}\right\}} , \quad i = 1,2 . \qquad (5\text{-}27)$$

- In calculating a theoretical effectiveness, the four E parameters for the process stream are calculated as

$$E_1 = \frac{\Lambda p}{(1 + E_4)} , \qquad E_2 = \frac{C_r}{C_p} ,$$
$$E_3 = C_p , \qquad E_4 = \frac{\Lambda_p C_r}{\Lambda_r C_p} , \qquad (5\text{-}28)$$

for each of the F_1 and F_2 waves.

- The theoretical efficiency for each wave is also calculated with the numerical finite-difference method developed by Lambertson (1958) for rotary heat exchange wheels.

Evaluation of the low-speed-test data continues as x_{eff} is determined in an iterative manner, as described in the following.

Low-Speed-Test Results for Case 1. Assuming that all the silica gel in the matrix is active, i.e., $x_{eff} = 1.0$, the measured experimental effectiveness is plotted against the corresponding theoretical effectiveness for the F_2 transfer in Figure 5-8 and for the F_1 transfer in Figure 5-9. A x_{eff} value of less than one implies that

$$m_{dd_{effective}} = m_{dd} \cdot x_{eff} , \tag{5-29}$$

and the heat capacity of the carrier (or substrate) per unit mass of effective dry desiccant cc is

$$cc = (1/sgf - 1)\ C_{p_{tape}}/x_{eff} + \left(\frac{1}{x_{eff}} - 1\right)C_{p_s} , \tag{5-30}$$

where

sgf = ratio of dry silica gel mass to dry coated tape mass

$C_{p_{tape}}$ = heat capacity of the tape (assumed to be that of Mylar), J/kgK

C_{p_s} = heat capacity of dry silica gel, J/kgK.

In Figure 5-8, a diagonal line representing $\eta_{exp} = \eta_{th}$ is shown. Note that all the η_{exp} data fall below the diagonal, indicating $\eta_{exp} < \eta_{th}$. η_{2exp} increases with increasing C_2, with a smooth trend and little scatter in the experimental data. For $\eta_{2exp} < 0.4$, the data lie on a straight line passing through the origin, with a slope of approximately 0.70.

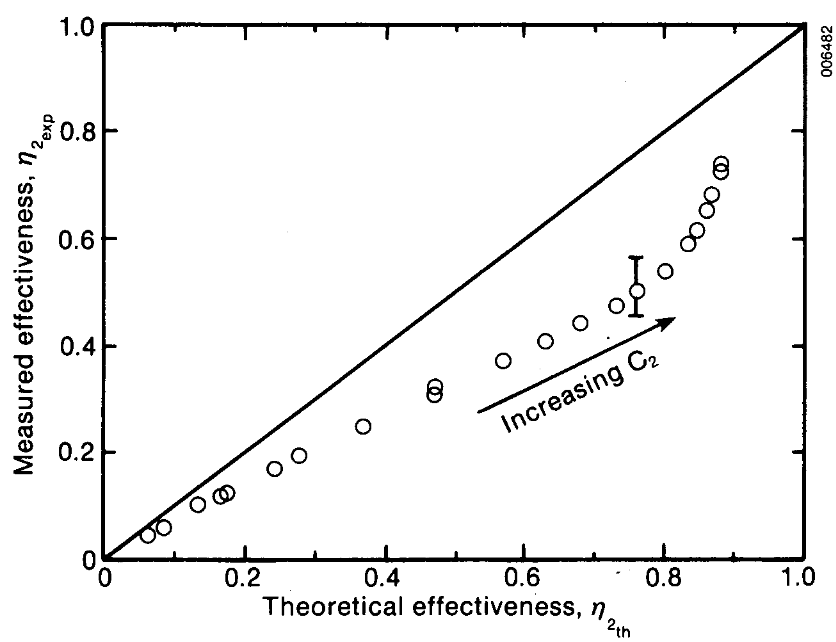

Figure 5-8. Measured F_2 Transfer Effectiveness η_{2exp} vs. Theoretical Effectiveness η_{2th} with Effective Mass Fraction $x_{eff} = 1.0$

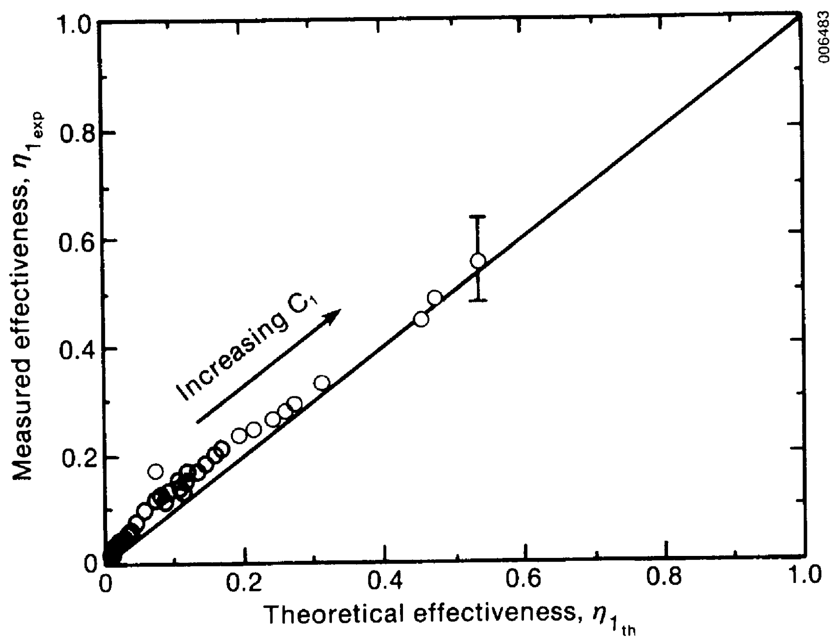

Figure 5-9. Measured F_1 Transfer Effectiveness η_{1exp} vs. Theoretical Effectiveness η_{1th} with Effective Mass Fraction x_{eff} = 1.0

This slope is a direct indicator of the effective silica gel fraction, x_{eff}. For $\eta_{2exp} > 0.4$, the data deviate considerably from the initial straight line, indicating nonlinear behavior. This deviation is caused by the assumption that the capacity rate ratio of the matrix is a constant. Corrections for taking varying capacity into account are addressed in the following section, as Case 2. In a range of η_{2exp} of less than 0.5, the theory over-predicts the efficiency by as much as 40%. As C_2 increases further, the deviation between the theory and the experiment gets smaller.

Figure 5-9 shows the variation of measured η_{1exp} versus theoretical η_{1th}. A diagonal line representing $\eta_{exp} = \eta_{th}$ is also shown in the figure. Note that, here, the experimental effectivenesses lie mostly above the diagonal, indicating $\eta_{exp} > \eta_{th}$. The slope of the η_{1exp} variation with η_{1th} in the neighborhood of the origin indicate that the heat capacity of the matrix is about 1.5 times what has been assumed with x_{eff} = 1.0. Note also that, as x_{eff} decreases, the effective heat capacity of the matrix increases. In the following discussions, the heat capacity as determined by Eq. 5-30 is used.

For a second iteration on identifying the effective mass, x_{eff} was assumed to be 0.70; a set of revised calculations was carried out. The results are shown in Figures 5-10 and 5-11 for the F_2 and F_1 transfers, respectively. These figures indicate that for $\eta_{exp} < 0.4$, the agreement between theory and experiment is closer. However, η_{2exp} is still generally lower than theory and η_{1exp} is higher, indicating that x_{eff} should perhaps be reduced to a value of about 0.65.

Further iterations were carried out taking into account varying matrix capacity, as discussed in the following section.

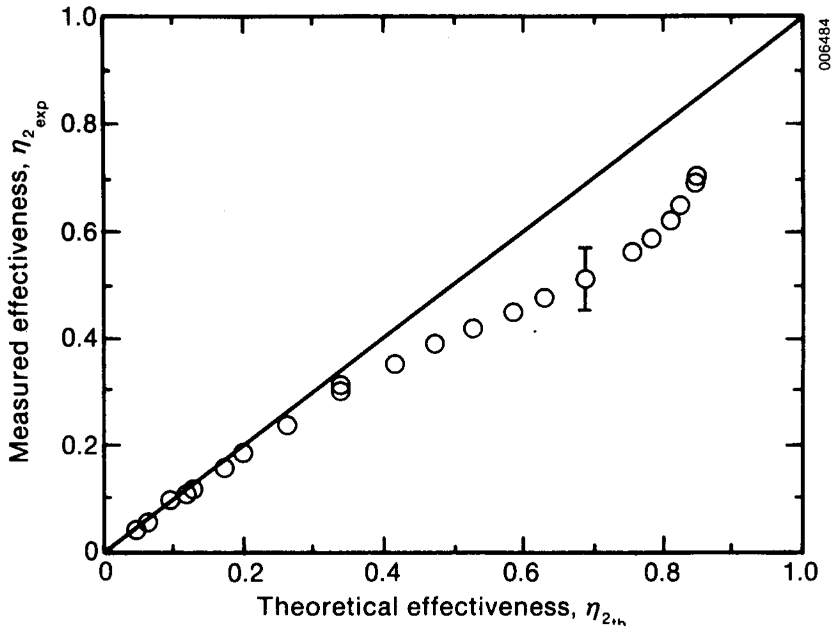

Figure 5-10. Measured F_2 Transfer Effectiveness η_{2exp} vs. Theoretical Effectiveness η_{2th} with Effective Mass Fraction $x_{eff} = 0.70$

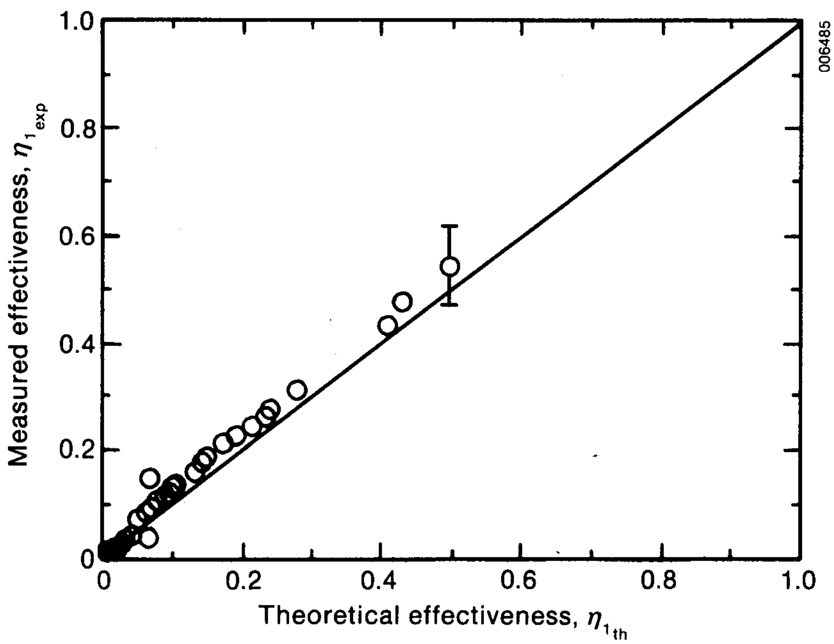

Figure 5-11. Measured F_1 Transfer Effectiveness η_{1exp} vs. Theoretical Effectiveness η_{1th} with Effective Mass Fraction $x_{eff} = 0.70$

Case 2: Varied Matrix Specific Capacity. The specific capacity ratios γ_1 and γ_2 for the F_1 and F_2 exchange vary widely over the nominal process and regeneration conditions. At nominal process and regeneration temperatures of 30^o and 80^oC, respectively, and an air humidity ratio of 0.015, γ_1 varies from 0.81 down to 0.39. The variation of γ_2 is larger; its value varies from 41 down to 4.6. The impact of these variations is an overall reduction in the transfer efficiency from the case with constant capacity.

To account for the variations in capacity, the finite-difference method of Lambertson (1958) was modified to calculate the sensible heat-exchanger efficiency based on the four characterizing parameters, $(NTU)_o$, C_{min}/C_{max}, C_r/C_{min}, and $(ha)'$. The capacity variation (assumed to vary linearly with temperature) was introduced using a parameter $\Delta C/C$ representing the overall variation in C_r, normalized by its mean value. An iterative scheme was employed to calculate outlet states based on inlet states for every element. These results were compared with an earlier model developed by Maclaine-cross (1974).

For the F_1 and F_2 transfer, we estimated the parameter $\Delta C/C$ using specific capacity ratios at process and regeneration inlet conditions. A set of theoretical efficiencies was calculated and compared with corresponding measured effectivenesses. An iterative process was then adopted to estimate the effective gel fraction x_{eff}.

5.2.2.2 Low-Speed-Test Results

Adopting the specific capacity ratio variations, the results, after a few iterations, with $x_{eff} = 0.625$, are shown in Figures 5-12 and 5-13. A comparison of measured F_2 effectiveness with η_{2th} is shown in Figure 5-12. For $0 < \eta_{2th} < 0.4$, the comparison is within ±3%. For $0.5 < \eta_2 < 0.7$, the theory predicts effectivenesses that are higher than the measurements by, at most, 10%. The cause for this discrepancy is a nonlinear variation of the capacity γ_2 as opposed to an assumed linear model in the theory.

Measured and theoretical effectivenesses for the F_1 transfer are shown in Figure 5-13. The experimental values are slightly higher than the theoretical values; however, they follow the trend extremely well. No significant deviation from theory can be seen here (as opposed to that for the F_2 effectiveness, shown in Figure 5-12). In general, the specific capacity γ_1 variation is smaller than that of γ_2, and thus the impact of capacity variations on F_1 effectiveness is smaller.

The general agreement between the measured and the experimental effectivenesses for F_1 and F_2 transfer indicate that the assumed effective gel fraction is around 0.625. However, uncertainties in this estimate arise from uncertainties in the air mass flow measurement, in the wheel rotational speed, and in the initial estimate of total gel on the test article. These result in an overall uncertainty in x_{eff} of ±10% of its value.

Some of the possible causes for a low effective gel fraction are uncertainties in the gel isotherm measurements, aging of the silica gel, and permeation of the adhesive to effectively block some of the pores otherwise available for adsorption. These causes cannot be quantified at present. A separate set of independent tests to determine the effective gel fraction will be carried out in the future in SERI facilities on samples taken from the matrix, to verify the findings.

5.2.3 Medium-Speed Tests ($0.5 < C_{1p}, C_{2p} < 2$)

Based on the low-speed and high-speed data analyses, the medium-speed performance of the rotor was predicted using the linearly varied capacity model described earlier. For

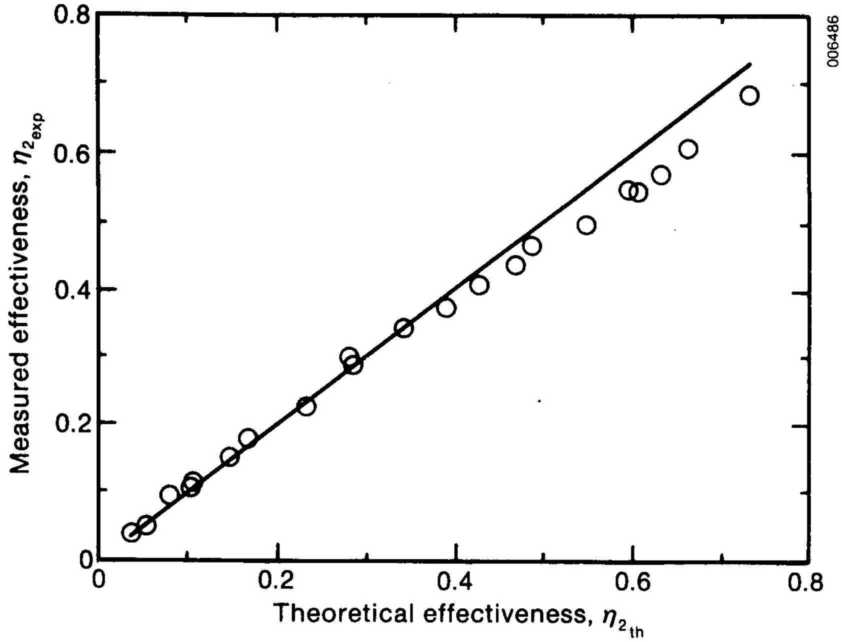

Figure 5-12. Measured F_2 Transfer Effectiveness η_{2exp} vs. Theoretical Effectiveness η_{2th} Using Linear Variation of γ_2 with x_{eff} = 0.625

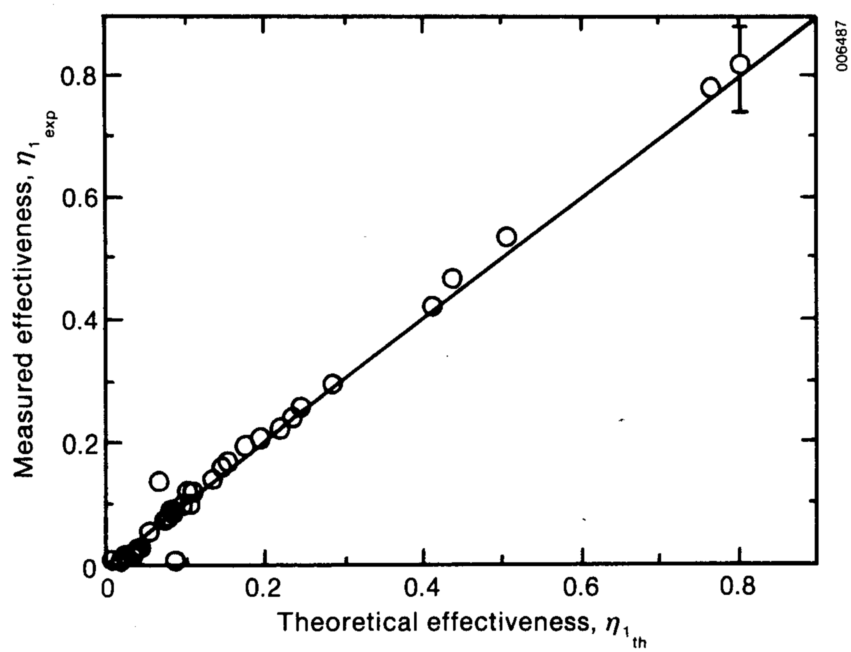

Figure 5-13. Measured F_1 Transfer Effectiveness η_{1exp} vs. Theoretical Effectiveness η_{1th} Using Linear Variation of γ_1 with x_{eff} = 0.625

the majority of the experimental conditions, the following parameters were found to hold. For the F_2 transfer:

$$(NTU)_o = 5 \qquad C_{min}/C_{max} = 1$$
$$(ha)' = 1 \qquad \Delta C/C = 1.6.$$

For the F_1 transfer:

$$(NTU)_o = 5 \qquad C_{min}/C_{max} = 1$$
$$(ha)' = 1 \qquad \Delta C/C = 0.6.$$

Using these parameters, we plotted the predicted theoretical effectiveness and the measured effectivenesses for both F_1 and F_2 transfers against a dimensionless rotational speed C_2 in Figure 5-14. C_2 varies from 0 to 8 on the abscissa. The theoretical F_2 effectiveness η_2 increases monotonically with C_2, reaching an asymptotic limit of 0.83 at large C_2 values. The experimental data follow the theory closely, rising rapidly in the range of $0 < C_2 < 2$, and gradually increasing further for larger C_2 values. Except for a few data points, the majority of the η_2 experimental data are in agreement with the theory, within a deviation of less than 10%.

Over the range of C_2 values, the dimensionless speed C_1 is approximately 1/35 of its C_2 value. The corresponding theoretical F_1 effectiveness is $\eta_1 = C_1$. Thus, the theoretical variation of η_1 with C_2 is essentially linear. The majority of the experimental η_1 effectivenesses follow this line, within a deviation of, once again, less than 10%.

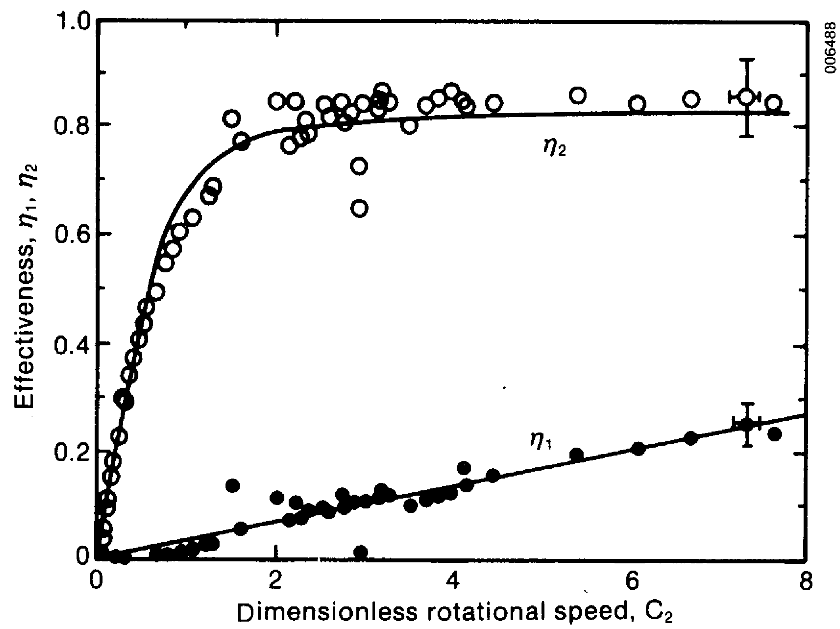

Figure 5-14. Measured Variations of η_1 and η_2 with C_2 over a Medium-Speed Range and a Theoretical Variation of η_1 and η_2 with C_2

The optimum rotational speed for a dehumidifier using silica gel, for balanced flow, with $x_{eff} = 1$, was found to be near $C_2 \approx 2$ (Jurinak 1982). This speed is close to C_2 when the ratio η_2/η_1 reaches a maximum. For the present test article, with $x_{eff} = 0.625$, this ratio reaches a maximum at rotational speeds greater than 2.

There are more experimental data points in the speed range $1.5 < C_2 < 4$ than in the other C_2 ranges. The scatter in measured η_2 in this range is also higher. These data were taken to identify the effects of varied air flow, process and regeneration temperatures, and absolute humidity levels. (See Appendix B on experimental data.) However, the scatter appears in the form of subtle but discernible trends in the variation of effectiveness with C_2 or C_1. We made no attempt to analyze these effects in more detail other than using an overall effectiveness variation with speed. A detailed numerical model such as MOSHMX (Maclaine-cross 1974) can perhaps be used to discern individual trends.

6.0 CONCLUDING REMARKS AND RECOMMENDATIONS

An independent series of leak tests, pressure-loss tests, and heat-and mass-transfer experiments on the rotary dehumidifiers tested led to the following findings.

- Leak tests indicated, for seals made of 76-μm-thick, double-layer Mylar tape, that an "effective" product of the discharge coefficient times leakage area per unit length of seal was 1.88×10^{-4} m for the circumferential seals and 9.35×10^{-4} m for the radial seals. Under typical operating conditions, these represent 2% and 3% air leaks per seal out of and across the two air streams. Since each percent leak translates into a percent reduction in overall dehumidifier effectiveness, it is desirable to develop improved seal designs to limit the discharge coefficient times leakage area product per unit length of seal to less than 0.5×10^{-4} m, without an undue increase in the rotor drive power. For the majority of applications, this leakage limit will translate into less than a 1% reduction in dehumidifier transfer effectiveness as a result of air leakage.

- The pressure-loss tests indicated large differences in both the intercept and the slope between the measurements and theoretical parallel-passage limits. Nonuniform passage spacing was identified as the cause of the discrepancy. Simple assumptions on the probability distribution of the gap size reconciled these differences. The assumed distribution implied a Nusselt number intercept, which was later verified from the heat- and mass-transfer tests within the experimental uncertainty range. The nonuniform gap spacing resulted in a 46% reduction in the overall NTU from the design value of 10. It is therefore critical for industry to obtain a desiccant/geometry matrix and manufacturing technique that compromises the uniformity of the air passages as little as possible to obtain the best dehumidifier performance. To limit the overall NTU reduction to less than 5% of a design value, the variation in air-passage-gap width should be limited to less than ±10% of the design gap.

- The heat- and mass-transfer test data were categorized according to high-, medium-, and low-speed tests and were analyzed by means of a nonlinear analogy theory. For the silica-gel dehumidifier, with experimentally inferred overall NTU of over 6 and effective Lewis number of less than 2, the analogy method was found entirely satisfactory for data analyses. The specific area of concern was found to be the matrix capacity rate ratio variations. The following paragraphs address further details.

- The high-speed-test results allowed us to infer "effective" heat- and mass-transfer rates and an overall NTU for the exchange processes. The Nusselt number was found to be 4.5, approximately 54% of its theoretical uniform passage limit. This value is consistent with the pressure-loss results referred to earlier. From the mass-transfer effectiveness, an "effective" Lewis number for the matrix was found to be 1.17. Should the resistance to mass transfer on the solid side be negligible, a lower limit on the effective Lewis number of 0.846 is possible. The inferred "effective" Lewis number thus implies that the solid side contributes about 38% to the overall mass-transfer resistance. Inference of the Lewis number enabled us to calculate a "solid-side conductance geometry factor." The solid-side resistance to mass transfer is inversely proportional to this conductance geometry factor, the desiccant density, its moisture diffusivity, and its isothermal rate of change of moisture content with respect to air humidity, and it is directly proportional to the desiccant particle size. The experimentally inferred solid-side conductance geometry factor was found to be near unity, and no significant variation was indicated with the matrix temperature or moisture content. Provided that all other desiccant properties are known, the packing factor on a substrate tape and the conductance geometry factor permit an engineering evaluation to be made of the solid-side resistance to estimate the design and performance of a crushed silica gel matrix such as those used for these test articles.

- The low-speed-test data correlated well with the analogy theory; at medium speeds, however, significant deviation from the theory was observed. A nonlinear analogy method, incorporating linear variation of the matrix capacity, was used to analyze the data. From the combined potential transfer effectiveness variations with the wheel rotational speed, an effective silica gel fraction was inferred to be 62.5% with an uncertainty of ±10% of its value. (See Appendix I on static capacity determination.) Causes for a low effective fraction are surmised to be adhesive penetration and reduction in gel capacity with age, and they will be evaluated by an independent investigation of this result on samples of the coated tape from the matrix. The implication of the reduced effective gel fraction is that the design capacity of this particular dehumidifier must be derated by 38%. However, since the reasons for the reduced gel fraction are yet to be identified, it is difficult at present to recommend means to improve this effective fraction. With further research, a target value of 90% for the effective gel fraction for advanced dehumidifier designs appears to be achievable.

- Using the low-speed and high-speed-test results, we predicted the medium-speed performance with the nonlinear analogy theory. The experimental effectivenesses agree with the theoretical model to within less than ±10%. The linear capacity variation used in the current model is, however, unsatisfactory. With improvements on the baseline model using a nonlinear variation, agreements to within less than 5% are perhaps possible. The analytical method available to characterize and predict dehumidifier performance provides a valuable tool in evaluating overall solar cooling system options.

Other accomplishments included an initial attempt by industry to fabricate a parallel-passage rotor, using double-sided, coated plastic tape with silica gel, of realistic rotor dimensions. Early attempts to wind the wheel were, however, unsuccessful, resulting in floppy tape segments and widely varied air gaps. The resulting wheel, labeled test article 1, was, however, tested over a range of conditions typical to solar cooling. The results indicated that the rotor did function as a dehumidifier, but an adequate basis for a comparison of experiments and existing theory could not be developed.

An attempt to rewind the rotor after the causes of nonuniformity were found and corrected resulted in considerably improved gap spacings. During the course of the winding, the causes for the nonuniformity arising from inadequate radial stiffness were identified as the wide variation in gel particle sizes, the large size of the particles in relation to the spacer width, and insufficient winding tension. The rewound wheel, labeled test article 2, was tested over a wide range of operating conditions.*

Based on the findings of this study, the following research activities are recommended for resolving open issues.

- An independent confirmation of the effective gel fraction must be pursued, using samples from the matrix.

- Nonuniform passages cause a significant reduction in the overall transfer effectiveness and are important factors in the fabrication of practical dehumidifiers. The details of

---

*During the course of these tests, a third test article was fabricated using a smaller, more uniform microbead silica gel with excellent uniformity in gap spacing. Tests of this test article are under way and are described in a forthcoming report (SERI/TR-252-2983).

the present approach to ensuring the uniformity of air gaps must be reviewed for other viable geometries.

- The solid-side conductance geometry factor for formulating an "effective" solid-side mass-transfer coefficient indicates that the solid-side resistance can be lowered by using smaller desiccant particles. An additional benefit here is that this also ensures more uniform passages. However, the effect of a reduction in the particle size on the effective gel fraction is uncertain and requires additional study.
- A suitable means must be found for attaching amorphous desiccants to substrates.
- More creative methods for combining polymeric desiccant films or a better extruded desiccant-cum-substrate combination could provide solutions to many of these problems.
- Contamination of desiccants caused by airborne pollutants and the associated reduction in dehumidifier capacity must be studied.
- The approximate analogy theory used here is not an exact solution of the model partial differential equations. A high-speed finite-difference solution based on an algorithm such as MOSHMX (Maclaine-cross 1974) would eliminate the errors associated with the approximations of these analyses.

7.0 REFERENCES

Ambrose, C. W., I. L. Maclaine-cross, and E. B. Robson, 1983, *The Use of Rotary Regenerative Heat Exchangers for the Conservation of Energy in Buildings*, Final Report Project 109, Canberra, Australia: National Energy Research Development and Demonstration Committee, Australian Government.

Banks, P. J., Feb. 1985, "Prediction of Heat and Mass Regenerator Performance Using Nonlinear Analogy Method: Part 1—Basis," and "Prediction of Heat and Mass Regenerator Performance Using Nonlinear Analogy Method: Part 2—Comparison of Methods," *Trans. ASME, J. Heat Transfer*, Vol. 107, pp. 222-238.

Banks, P. J., 1972, "Coupled Equilibrium Heat and Single Adsorbate Transfer in Fluid Flow through a Porous Medium—I, Characteristic Potentials and Specific Capacity Ratios," *Chem. Engng. Sci.*, Vol. 27, pp. 1143-1155.

Banks, P. J., D. J. Close, and I. L. Maclaine-cross, Sept. 1970, "Coupled Heat and Mass Transfer in Fluid Flow through Porous Media—An Analogy with Heat Transfer," *Proc. 4th Int. Heat Transfer Conf.*, Versailles.

Benedict, R. P., 1977, *Fundamentals of Temperature, Pressure, and Flow Measurements*, New York: John Wiley and Sons.

Benedict, R. P., Dec. 1966, "Most Probable Discharge Coefficients for ASME Flow Nozzles," *Trans. ASME, J. Basic Eng.*, p. 734.

Cornish, R. J., 1928, "Flow in a Pipe of Rectangular Cross-Section," *Proc. of the Royal Society*, Vol. A120, pp. 691-700.

Duffie, J. A., and W. A. Beckman, 1980, *Solar Engineering of Thermal Processes*, New York: John Wiley and Sons.

Dunkle, R. V., P. J. Banks, and I. L. Maclaine-cross, 1980, "Wound Parallel Plate Exchangers for Air-Conditioning Applications," *Compact Heat Exchangers*, ASME HTD-Vol. 10, edited by R. K. Shah et al., pp. 65-72.

Henry, P. S. H., 1939, "Diffusion in Adsorbing Media," *Proc. Roy. Soc.*, Ser. A, Vol. 171, pp. 215-241.

Hilsenrath, J., et al., 1960, "Tables of Thermodynamic and Transport Properties of Air, Argon, Carbon Dioxide, Carbon Monoxide, Hydrogen, Nitrogen, Oxygen, and Steam," Oxford, England: Pergamon Press.

Johnston, R. C. R., 1967, "Regenerative Evaporative Air Conditioning with Dehumidification," *Aust. Refrigeration, Air Conditioning and Heating*, Vol. 21, No. 2, pp. 29-34 and 65.

Jurinak, J. J., and P. J. Banks, Nov. 1982, "A Numerical Evaluation of Two Analogy Solutions for a Rotary Silica Gel Dehumidifier," *Heat Transfer in Porous Media*, edited by J. V. Beck and L. S. Yao, ASME, Pub. HTD-Vol. 22.

Jurinak, J. J., and J. W. Mitchell, 1984, "Effect of Matrix Properties on the Performance of a Counterflow Rotary Dehumidifier," *Trans. ASME, J. Heat Transfer*, Vol. 106, pp. 638-645.

Jurinak, J. J., 1982, "Open Cycle Desiccant Cooling — Component Models and Systems Simulations," Ph.D. Thesis, University of Wisconsin, Solar Energy Laboratory.

Kang, T. S., 1985, "Adiabatic Desiccant Open Cooling Cycles," Master of Engineering Thesis, New South Wales, Australia: University of New South Wales.

Kays, W. M., and A. L. London, 1984, *Compact Heat Exchangers*, 3rd edition, New York: McGraw-Hill.

Lambertson, T. J., 1958, "Performance Factors of a Periodic-Flow Heat Exchanger," *Trans. ASME*, pp. 586-592.

Lavan, Z., J. B. Monnier, and W. M. Worek, 1982, "Second Law Analysis of Desiccant Cooling Systems," *Trans. ASME, J. Solar Energy Eng.*, Vol. 104, pp. 229-236.

Lee, K. C., Oct. 1984, "Tests on a Compact Shielded Wet Bulb Psychrometer," Bachelor of Engineering Thesis, New South Wales, Australia: The University of New South Wales.

Lunde, P. J., 1980, *Solar Thermal Engineering*, New York: John Wiley and Sons.

Lundgren, T. S., E. M. Sparrow, and J. B. Starr, Sept. 1964, "Pressure Drop Due to the Entrance Region in Ducts of Arbitrary Cross Section," *ASME J. Basic Engineering*, Vol 86, No. 3, pp. 620-626.

Maclaine-cross, I. L., 1985, "High Performance Adiabatic Desiccant Open Cooling Cycles," *Trans. ASME, J. Solar Energy Eng.*, Vol. 107, pp. 102-104.

Maclaine-cross, I. L., 1980, "Effect of Interstitial Fluid Heat Capacity on Regenerator Performance," *Trans. ASME, J. Heat Transfer*, Vol. 102, pp. 572-573.

Maclaine-cross, I. L., Aug. 1978, "Comparison of the Analogy Theory of Combined Heat and Mass Transfer in Regenerators with a Finite Difference Solution," New South Wales, Australia: Department of Mining and Mineral Sciences, University of New South Wales.

Maclaine-cross, I. L., 1974, "A Theory of Combined Heat and Mass Transfer in Regenerators," Ph.D. Thesis, Department of Mechanical Engineering, Monash University.

Maclaine-cross, I. L., 1973, "Combined Heat and Mass Transfer in Regenerators with Multiple Film Transfer Coefficients," paper presented at the First Australian Conference on Heat and Mass Transfer, Melbourne, Australia.

Maclaine-cross, I. L., and C. W. Ambrose, Mar. 1980, "Predicted and Measured Pressure Drop in Parallel Plate Rotary Regenerators," *Trans. ASME, J. Fluids Engineering*, Vol. 102, pp. 59-63.

Maclaine-cross, I. L., and P. J. Banks, 1972, "Coupled Heat and Mass Transfer in Regenerators—Prediction Using an Analogy with Heat Transfer," *Int. J. Heat Mass Transfer*, Vol. 15, pp. 1225-1242.

Maclaine-cross, I. L., and J. M. Parsons, 1986, *A Five-Ton Advanced Solid-Desiccant Solar Cooling System with Heating and Service Hot Water*, SERI/SP-252-2832, Golden, CO: Solar Energy Research Institute.

Mason, E. A., and L. Monchick, 1965, "Survey of the Equation of State and Transport Properties of Moist Gases," *Humidity and Moisture*, edited by A. Wexler, New York: Reinhold, Vol. 3, pp. 257-272.

Mitchell, J. W., 1983, *Energy Engineering*, New York: John Wiley and Sons.

Ower, E., and R. C. Pankhurst, 1975, *The Measurement of Air Flow*, London: Pergamon Press.

Penney, T. R., and I. L. Maclaine-cross, May 1985, "Promising Advances in Desiccant Cooling," SERI/TP-252-2683, Golden, CO: Solar Energy Research Institute.

Pennington, N. A., 1955, "Humidity Changer for Air Conditioning," U.S. Patent No. 2,700,537.

Pesaran, A. P., I. L. Maclaine-cross, and E. Van Den Bulck, 1986, *Measurements on Promising Dehumidifier Materials and Geometries*, SERI/TR-252-2898, Golden, CO: Solar Energy Research Institute.

Schlepp, D., and R. Barlow, Sept. 1984, *Performance of the SERI Parallel-Passage Dehumidifier*, SERI/TR-252-1951, Golden, CO: Solar Energy Research Institute.

Schlepp, D., K. J. Schultz, and F. Zangrando, 1984, *Facility Design for Cyclic Testing of Advanced Solid Desiccant Dehumidifiers*, SERI/TR-252-2464, Golden, CO: Solar Energy Research Institute.

Schultz, K. J., 1986, *SERI Desiccant Cooling Test Facility: Status Report: Preliminary Data on the Performance of a Rotary Parallel Passage, Silica Gel Dehumidifier*, SERI/TR-252-2718, Golden, CO: Solar Energy Research Institute.

Sladek, K. J., E. R. Gilliland, and R. F. Baddour, 1974, "Diffusion on Surfaces II: Correlation of Diffusivities of Physically and Chemically Adsorbed Species," *Ind. Eng. Chem. Fundam.*, Vol. 13, No. 2, pp. 100-105.

Spahn, H., and V. Gnielinski, 1971, "Wärme und Steffaustausch in Cinem Sorptions Regenerator," *Verfahrenstechnik*, Vol. 5, No. 4, pp. 143-149.

Van Den Bulck, E., S. A. Klein, and J. W. Mitchell, Nov. 1985, "Second Law Analysis of Solid Desiccant Rotary Dehumidifiers," paper presented at the National Heat Transfer Conference, AIChE, Denver, CO.

van Leersum, J. G., and D. J. Close, June 1982, "Experimental Verification of Open Cycle Cooling System Component Models," draft report, University of Wisconsin.

Wylie, R. G., 1981, "Detailed Determination of the Psychrometer Coefficient for the Wet Cylinder in a Transverse Airstream and an Analysis of Its Accuracy," Technical Paper No. 7, Australia: Commonwealth Scientific and Industrial Research Organization, Division of Applied Physics.

Wylie, R. G., June 1969, *The Psychrometer Problem—A Precise Analysis*, PIR Report No. 65, Australia: Commonwealth Scientific and Industrial Research Organization.

Wylie, R. G., and T. Lalas, 1981, "The WMO Psychrometer," Technical Paper No. 3, Australia: Commonwealth Scientific and Industrial Research Organization, Division of Applied Physics.

APPENDIX A

MEASUREMENT UNCERTAINTIES

Uncertainties in the primary measurements were discussed in Section 2.0 and are summarized in Table A-1. Uncertainty estimates in the derived parameters were arrived at by performing the propagation analyses using partial derivatives described by Kline and McClintock (1953).*

For the low-speed-test results, the following nominal operating conditions were assumed:

$$\dot{m}_p = \dot{m}_r = 0.24 \text{ kg/s}; \; t_{pi} = 30°\text{C}; \; t_{ri} = 80°; \; w_{pi} = w_{ri} = 0.015 \text{ kg/kg} .$$

For the high-speed-test results, the following nominal operating conditions were assumed:

$$\dot{m}_p = \dot{m}_r = 0.24 \text{ kg/s}, \; t_{pi} = 30°\text{C}, \; t_{ri} = 60°\text{C}, \; w_{pi} = 0.020 \text{ kg/kg}; \; w_{ri} = 0.010 \text{ kg/kg} .$$

The results of the propagation analyses are presented in Table A-2. These estimates provide uncertainties for the majority of the tested conditions.

Table A-1. Summary of Uncertainties in Primary Measurements

Air flow rate	±3.6%
Air temperature	±0.6°C
Air absolute humidity	±3%
Pressure differences	±1%
Wheel rotational speed	±1%

*Kline, S.J. and McClintock, F.A., "Describing Uncertainties in Single-Sample Experiments," *Mechanical Engineering*, Jan. 1953, pp. 3-8.

Table A-2. Summary of Uncertainties in Derived Quantities

Quantity	Relative Uncertainty Estimate (%)	Remarks
$\frac{\Delta p D_h^2}{2 \mu u L}$	4.2	Results from uncertainties in air-flow and area estimates
$\frac{Re D_h}{4L}$	4.2	Results from uncertainties in air-flow and area estimates
η_t	2.0	Calculated for high-speed-test results only
η_w	6.0	Calculated for high-speed-test results only
$(NTU)_t$	10.0	Calculated for high-speed-test results only
$(NTU)_w$	30.0	Increases with smaller $(w_1 - w_2)$
Nu	10.8	
$\frac{Re Pr D_h}{2L}$	4.7	
Le_{eff}	32.0	Increases with smaller (w_1-w_2)
e_s	33.0	Solid-side conductance geometry factor
C_{2p}	6.2	
η_{2p}	7.8	For $C_{2p} > 0.1$
x_{eff}	10.0	Errors due to gel age and adhesive penetration not taken into account
C_{1p}	12.6	
η_{1p}	8.9	For $C_{1p} > 0.1$

APPENDIX B

EXPERIMENTAL DATA

The experimental data for test article 2 are summarized in Table B-1. The tabular entries are rather self-explanatory. For each test, there are two adjacent rows of entries. The first row refers to the process stream conditions and the second row to the corresponding regeneration stream conditions.

Column 1 contains the arbitrary experimental classifications that were based on the wheel rotational speed (low, medium, and high) and other primary test variables, such as process and regeneration temperatures, air flow rates, and humidity levels. Columns 2 and 3 contain the test sequence numbers and identification numbers stored in floppy diskettes. Column 4 identifies the air stream as either process or regeneration. Column 5 presents the dry air mass flow (in kg/s) into the rotary dehumidifier test article. In columns 6 and 7 are the inlet and outlet air temperatures (in ^{o}C). Columns 8 and 9 contain the static pressure (in Pa) just upstream and downstream of the rotor. The absolute humidity levels (kg/kg of dry air) at the rotor inlet and outlet are presented in columns 10 and 11. Column 12 lists the wheel rotational speed in revolutions per hour, and columns 13 and 14 provide a measure of error in mass and energy balances, respectively, in relation to the exchange taking place.

The errors in mass and energy balances are calculated as follows. The exchange error in moisture mass balance,

$$= \frac{\dot{m}_p \; \Delta w_p + \dot{m}_r \; \Delta w_r}{(|\dot{m}_p \; \Delta w_p| + |\dot{m}_r \; \Delta w_r|)/2} \; ,$$

is expressed as a percentage, and the exchange error in enthalpy balance,

$$= \frac{\dot{m}_p \; \Delta h_p + \dot{m}_r \; \Delta h_r}{(|\dot{m}_p \; \Delta h_p| + |\dot{m}_r \; \Delta h_r|)/2} \; ,$$

is also expressed as a percentage. Here, Δw_p refers to the change in the absolute humidity of the process stream, and Δh_p refers to its change in specific enthalpy. Similar definitions apply to the regeneration stream.

For perfect mass balance in tests, it is clear that these exchange errors must be zero. The majority of the experimental exchange errors quoted are within ±10%. However, there are instances in which the enthalpy errors are large. These high errors occur (a) when the wheel rotational speed is quite low, and the enthalpy exchange between the process and regeneration streams is minimal, and (b) in two of the high-speed tests, where the enthalpy difference between the process and the regeneration inlet stream was minimal.

These errors illustrate the accuracy with which the process and regeneration effectivenesses can be calculated and are indicators of the consistency of the test results. Results for 73 tests are reported in Table B-1.

Table B-1. Experimental Data

Expt. Category	Ser. No.	Run Identifier	Air Stream Tag	Dry Air Flow Rate (kg/s)	Inlet Temperature (C)	Outlet Temperature (C)	Inlet Static Pressure (Pa)	Outlet Static Pressure (Pa)	Inlet Humidity (kg/kg)	Outlet Humidity (kg/kg)	Wheel Rotational Speed (rev/hr)	Balance Errors Mass (%)	Balance Errors Enth. (%)
Med. Speed	6	1030852A	process	0.220	29.97	62.66	82421.1	82358.1	0.01535	0.00746	15.301	-1.4	-0.1
Med. Speed	6	1030852A	regen.	0.222	79.78	47.41	82403.9	82352.0	0.01514	0.02304	15.301		
Med. Speed	7	1030853A	process	0.220	29.97	64.27	82328.9	82266.5	0.01584	0.00873	25.623	-5.3	-0.5
Med. Speed	7	1030853A	regen.	0.222	79.78	45.25	82310.6	82259.0	0.01547	0.02287	25.623		
Med. Speed	8	1030854A	process	0.220	29.97	65.13	82248.8	82186.4	0.01677	0.00979	29.958	-3.3	-0.8
Med. Speed	8	1030854A	regen.	0.222	79.77	44.85	82230.3	82178.7	0.01650	0.02362	29.958		
Med. Speed	9	1030855A	process	0.220	29.97	64.69	82138.7	82076.5	0.01836	0.00986	19.279	-4.1	-2.0
Med. Speed	9	1030855A	regen.	0.222	79.77	45.05	82121.1	82070.0	0.01661	0.02537	19.279		
Med. Speed	30	1106851E	process	0.219	29.97	58.90	82249.3	82182.8	0.01640	0.00840	6.350	-6.1	-6.8
Med. Speed	30	1106851E	regen.	0.221	79.77	50.57	82236.9	82180.0	0.01672	0.02515	6.350		
Med. Speed	31	1106852E	process	0.219	29.96	60.82	82273.2	82206.9	0.01618	0.00802	9.116	-2.6	-0.3
Med. Speed	31	1106852E	regen.	0.222	79.75	48.86	82260.1	82203.3	0.01640	0.02470	9.116		
Med. Speed	32	1106853E	process	0.219	29.96	61.80	82317.7	82251.8	0.01615	0.00809	12.234	-3.5	-0.7
Med. Speed	32	1106853E	regen.	0.222	79.74	47.80	82304.4	82247.8	0.01640	0.02466	12.234		
Med. Speed	33	1106854E	process	0.219	29.97	62.69	82328.5	82264.1	0.01577	0.00814	16.923	-3.4	1.5
Med. Speed	33	1106854E	regen.	0.222	79.76	46.73	82315.2	82259.6	0.01600	0.02381	16.923		
Med. Speed	34	1106855E	process	0.219	29.97	63.64	82341.9	82276.3	0.01561	0.00844	22.817	-0.4	1.9
Med. Speed	34	1106855E	regen.	0.222	79.76	46.31	82327.5	82270.9	0.01585	0.02296	22.817		
Med. Speed	36	1107852A	process	0.219	29.97	65.79	82073.6	82009.4	0.01749	0.01060	35.086	-3.6	-0.0
Med. Speed	36	1107852A	regen.	0.222	79.77	43.91	82060.6	82002.3	0.01642	0.02349	35.086		
Med. Speed	38	1107854A	process	0.219	29.97	67.80	82013.4	81949.6	0.01745	0.01220	55.146	4.4	3.9
Med. Speed	38	1107854A	regen.	0.222	79.77	42.14	81999.0	81941.1	0.01645	0.02141	55.146		
Med. Speed	39	1107855A	process	0.219	29.98	68.65	81991.8	81928.2	0.01744	0.01296	65.590	5.1	3.6
Med. Speed	39	1107855A	regen.	0.222	79.78	41.28	81976.8	81918.8	0.01643	0.02063	65.590		
Med. Speed	61	1113854B	process	0.220	29.98	64.00	82084.2	82019.5	0.01450	0.00795	26.665	-0.5	-0.7
Med. Speed	61	1113854B	regen.	0.222	79.77	46.34	82071.5	82015.2	0.01493	0.02145	26.665		
Med. Speed	62	1114851A	process	0.219	29.98	66.67	82618.8	82555.6	0.01468	0.00971	47.730	1.4	3.2
Med. Speed	62	1114851A	regen.	0.222	79.80	43.13	82604.0	82547.3	0.01446	0.01930	47.730		
Med. Speed	45	1112851A	process	0.171	29.97	63.99	81900.6	81851.2	0.01619	0.00848	16.382	-0.6	7.6
Med. Speed	45	1112851A	regen.	0.173	79.70	45.04	81891.0	81847.4	0.01597	0.02364	16.382		
Med. Speed	46	1112851B	process	0.171	29.97	62.42	81785.9	81735.8	0.01743	0.00881	8.448	-4.4	-4.9
Med. Speed	46	1112851B	regen.	0.173	79.71	47.40	81776.1	81732.6	0.01774	0.02665	8.448		
Med. Speed	47	1112852B	process	0.171	29.96	63.00	81675.0	81624.9	0.01636	0.00791	10.092	-2.5	2.2
Med. Speed	47	1112852B	regen.	0.173	79.72	46.48	81664.7	81621.4	0.01564	0.02420	10.092		

Table B-1. Experimental Data (Continued)

Expt. Category	Ser. No.	Run Identifier	Air Stream Tag	Dry Air Flow Rate (kg/s)	Inlet Temperature (C)	Outlet Temperature (C)	Inlet Static Pressure (Pa)	Outlet Static Pressure (Pa)	Inlet Humidity (kg/kg)	Outlet Humidity (kg/kg)	Wheel Rotational Speed (rev/hr)	Balance Errors Mass (%)	Balance Errors Enth. (%)
Hum. Level	40	1108851A	process	0.217	29.97	54.53	80897.5	80830.8	0.00678	0.00178	9.703	-0.6	2.5
Hum. Level	40	1108851A	regen.	0.219	79.75	55.05	80885.9	80828.9	0.00685	0.01184	9.703		
Hum. Level	42	1111851A	process	0.219	29.97	59.09	81651.0	81584.7	0.01243	0.00539	11.123	-3.5	7.3
Hum. Level	42	1111851A	regen.	0.221	79.76	49.56	81639.8	81581.5	0.01288	0.02011	11.123		
Hum. Level	43	1111852A	process	0.220	29.97	61.61	81659.3	81592.9	0.01579	0.00750	10.502	-0.5	0.1
Hum. Level	43	1111852A	regen.	0.222	79.77	48.44	81648.2	81589.6	0.01485	0.02310	10.502		
Hum. Level	44	1111853A	process	0.221	29.97	63.58	81510.2	81445.0	0.02206	0.01322	9.608	-1.4	-2.0
Hum. Level	44	1111853A	regen.	0.223	79.77	46.56	81500.6	81442.3	0.02119	0.03008	9.608		
Air Flow	48	1112853B	process	0.190	29.96	62.27	81681.7	81625.4	0.01584	0.00755	10.291	-1.7	3.4
Air Flow	48	1112853B	regen.	0.192	79.74	47.20	81670.5	81621.6	0.01517	0.02351	10.291		
Air Flow	49	1112854B	process	0.210	29.97	61.60	81665.4	81602.8	0.01625	0.00805	10.626	-1.2	3.1
Air Flow	49	1112854B	regen.	0.212	79.77	48.07	81653.4	81598.8	0.01662	0.02484	10.626		
Air Flow	50	1112855B	process	0.229	29.97	61.19	81608.1	81539.0	0.01646	0.00824	10.653	-4.2	-5.0
Air Flow	50	1112855B	regen.	0.232	79.79	48.70	81595.3	81535.0	0.01684	0.02534	10.653		
Air Flow	51	1112851C	process	0.249	29.97	59.56	81604.3	81528.3	0.01565	0.00778	10.036	-3.1	4.9
Air Flow	51	1112851C	regen.	0.251	79.80	49.52	81590.6	81524.6	0.01603	0.02408	10.036		
Air Flow	52	1112852C	process	0.268	29.97	59.36	81615.4	81532.5	0.01550	0.00771	10.369	-2.4	1.3
Air Flow	52	1112852C	regen.	0.271	79.81	50.21	81600.2	81528.4	0.01576	0.02368	10.369		
Air Flow	53	1112853C	process	0.288	29.98	58.56	81742.4	81652.8	0.01521	0.00763	10.294	-3.0	1.0
Air Flow	53	1112853C	regen.	0.290	79.81	50.92	81726.1	81648.7	0.01558	0.02332	10.294		
Proc. Temp.	2	1029852A	process	0.191	32.96	64.97	83141.9	83089.2	0.01995	0.01096	10.998	1.2	9.8
Proc. Temp.	2	1029852A	regen.	0.194	79.74	47.63	83126.7	83083.5	0.01872	0.02748	10.998		
Proc. Temp.	4	1029854A	process	0.191	29.97	64.46	83076.3	83023.8	0.02002	0.01058	10.894	-2.7	-6.3
Proc. Temp.	4	1029854A	regen.	0.194	79.73	45.91	83060.8	83018.7	0.01844	0.02801	10.894		
Proc. Temp.	54	1113851A	process	0.191	27.14	61.91	81844.1	81787.9	0.01870	0.00953	11.205	-3.4	-0.6
Proc. Temp.	54	1113851A	regen.	0.193	79.73	44.88	81833.2	81783.9	0.01906	0.02845	11.205		
Proc. Temp.	55	1113852A	process	0.191	32.97	63.77	81864.8	81808.2	0.01872	0.01055	10.752	-3.8	4.3
Proc. Temp.	55	1113852A	regen.	0.193	79.74	48.22	81854.0	81804.1	0.01928	0.02769	10.752		
Proc. Temp.	56	1113853A	process	0.191	35.96	65.05	81966.0	81909.4	0.01860	0.01107	11.404	-3.3	3.3
Proc. Temp.	56	1113853A	regen.	0.193	79.73	50.10	81955.4	81905.6	0.01913	0.02686	11.404		
Proc. Temp.	57	1113854A	process	0.191	29.97	63.10	81851.3	81794.9	0.01862	0.01000	11.367	-2.4	-2.7
Proc. Temp.	57	1113854A	regen.	0.193	79.74	46.95	81840.0	81791.3	0.01927	0.02803	11.367		
Regn. Temp.	27	1105851B	process	0.220	29.97	43.05	81571.0	81512.2	0.01520	0.01146	9.851	11.7	-22.5
Regn. Temp.	27	1105851B	regen.	0.221	49.87	38.68	81564.1	81508.8	0.01574	0.01905	9.851		

Table B-1. Experimental Data (Continued)

Expt. Category	Ser. No.	Run Identifier	Air Stream Tag	Dry Air Flow Rate (kg/s)	Inlet Temperature (C)	Outlet Temperature (C)	Inlet Static Pressure (Pa)	Outlet Static Pressure (Pa)	Inlet Humidity (kg/kg)	Outlet Humidity (kg/kg)	Wheel Rotational Speed (rev/hr)	Balance Errors Mass (%)	Balance Errors Enth. (%)
Regn. Temp.	58	1113851B	process	0.220	29.98	42.49	81997.9	81939.5	0.01476	0.01121	10.071	-0.6	-12.1
Regn. Temp.	58	1113851B	regen.	0.222	49.89	37.85	81989.9	81936.9	0.01521	0.01876	10.071		
Regn. Temp.	59	1113852B	process	0.220	29.98	54.36	81993.6	81930.6	0.01456	0.00812	10.593	-4.2	3.8
Regn. Temp.	59	1113852B	regen.	0.222	69.81	44.74	81983.2	81927.9	0.01516	0.02182	10.593		
Regn. Temp.	60	1113853B	process	0.220	29.98	65.63	81918.9	81850.7	0.01436	0.00582	10.499	-3.9	3.4
Regn. Temp.	60	1113853B	regen.	0.222	89.74	53.34	81905.6	81848.3	0.01505	0.02384	10.499		
Low Speed	21	1104851B	process	0.220	29.97	33.49	82354.4	82287.9	0.01459	0.01367	0.279	-7.7	-75.9
Low Speed	21	1104851B	regen.	0.222	79.77	76.69	82339.9	82293.5	0.01491	0.01590	0.279		
Low Speed	23	1105851A	process	0.220	29.97	40.81	81557.9	81488.7	0.01472	0.01140	1.000	-10.3	-65.8
Low Speed	23	1105851A	regen.	0.221	79.78	69.22	81546.6	81492.7	0.01482	0.01847	1.000		
Low Speed	63	1114851B	process	0.220	29.98	49.93	82589.3	82523.3	0.01471	0.00886	2.698	-5.3	0.7
Low Speed	63	1114851B	regen.	0.222	79.78	59.04	82577.7	82524.1	0.01419	0.02031	2.698		
Low Speed	64	1114852B	process	0.220	29.98	52.77	82476.2	82410.3	0.01500	0.00842	3.419	-2.9	-9.6
Low Speed	64	1114852B	regen.	0.222	79.78	57.20	82464.0	82410.0	0.01443	0.02114	3.419		
Low Speed	65	1114853B	process	0.220	29.98	55.81	82328.5	82262.5	0.01498	0.00773	4.660	-4.5	-8.0
Low Speed	65	1114853B	regen.	0.222	79.77	53.92	82315.4	82260.9	0.01436	0.02187	4.660		
Low Speed	74	1121851A	process	0.220	29.97	31.83	81130.9	81060.9	0.01533	0.01503	0.130	1.9	-98.0
Low Speed	74	1121851A	regen.	0.221	79.77	78.65	81120.9	81068.0	0.01605	0.01634	0.130		
Low Speed	75	1122851A	process	0.220	29.98	34.03	81582.5	81514.3	0.01425	0.01314	0.358	1.9	-30.6
Low Speed	75	1122851A	regen.	0.221	79.77	76.05	81576.0	81522.2	0.01361	0.01470	0.358		
Low Speed	76	1122852A	process	0.220	29.97	35.64	81451.7	81382.5	0.01447	0.01282	0.517	-4.4	-10.9
Low Speed	76	1122852A	regen.	0.221	79.78	74.01	81441.3	81388.4	0.01385	0.01556	0.517		
Low Speed	77	1122853A	process	0.220	29.97	36.53	81398.7	81330.8	0.01454	0.01254	0.593	0.8	3.6
Low Speed	77	1122853A	regen.	0.221	79.77	73.09	81391.0	81337.7	0.01420	0.01618	0.593		
Low Speed	78	1122854A	process	0.220	29.98	34.18	81317.4	81249.0	0.01459	0.01343	0.374	0.1	-16.5
Low Speed	78	1122854A	regen.	0.221	79.77	75.71	81308.9	81256.6	0.01431	0.01547	0.374		
Low Speed	79	1122855A	process	0.220	29.98	32.29	81428.4	81359.1	0.01458	0.01413	0.181	3.2	-80.4
Low Speed	79	1122855A	regen.	0.221	79.78	78.15	81418.6	81366.7	0.01422	0.01466	0.181		
Low Speed	80	1122851B	process	0.220	29.96	38.02	81550.4	81483.2	0.01369	0.01122	0.787	5.8	25.6
Low Speed	80	1122851B	regen.	0.221	79.77	71.41	81543.2	81490.1	0.01399	0.01631	0.787		
Low Speed	81	1125851A	process	0.220	29.97	42.22	80885.1	80816.9	0.01494	0.01085	1.246	5.6	49.1
Low Speed	81	1125851A	regen.	0.221	79.77	66.63	80876.7	80821.3	0.01436	0.01820	1.246		
Low Speed	82	1125851B	process	0.220	29.99	44.77	80793.8	80726.2	0.01474	0.01015	1.601	-0.8	16.8
Low Speed	82	1125851B	regen.	0.221	79.77	64.22	80785.1	80729.6	0.01415	0.01874	1.601		

Table B-1. Experimental Data (Continued)

Expt. Category	Ser. No.	Run Identifier	Air Stream Tag	Dry Air Flow Rate (kg/s)	Inlet Temperature (C)	Outlet Temperature (C)	Inlet Static Pressure (Pa)	Outlet Static Pressure (Pa)	Inlet Humidity (kg/kg)	Outlet Humidity (kg/kg)	Wheel Rotational Speed (rev/hr)	Balance Errors Mass (%)	Balance Errors Enth. (%)
Low Speed	83	1125852B	process	0.220	30.00	43.69	80788.2	80719.8	0.01472	0.01049	1.427	0.7	17.2
Low Speed	83	1125852B	regen.	0.221	79.77	65.49	80778.1	80723.2	0.01420	0.01838	1.427		
Low Speed	84	1125853B	process	0.220	29.97	40.66	80825.7	80756.3	0.01462	0.01137	1.013	2.3	11.1
Low Speed	84	1125853B	regen.	0.221	79.76	68.86	80815.5	80761.2	0.01410	0.01726	1.013		
Low Speed	85	1125854B	process	0.220	29.97	46.02	80823.6	80755.6	0.01461	0.00979	1.810	-2.8	0.3
Low Speed	85	1125854B	regen.	0.221	79.77	63.31	80814.3	80758.9	0.01413	0.01906	1.810		
Low Speed	86	1125855B	process	0.220	29.97	47.21	80858.4	80791.0	0.01525	0.01004	1.967	-2.8	-2.4
Low Speed	86	1125855B	regen.	0.221	79.77	62.23	80849.7	80793.9	0.01469	0.02000	1.967		
Low Speed	87	1125851C	process	0.220	29.96	48.02	80898.1	80830.5	0.01445	0.00908	2.257	-3.6	-2.6
Low Speed	87	1125851C	regen.	0.221	79.77	61.34	80889.0	80833.0	0.01445	0.01997	2.257		
Low Speed	88	1125852C	process	0.220	29.97	49.98	80938.0	80870.7	0.01453	0.00865	2.714	-4.0	-7.4
Low Speed	88	1125852C	regen.	0.221	79.77	59.57	80928.7	80872.4	0.01450	0.02058	2.714		
Low Speed	89	1125853C	process	0.220	29.96	51.07	81053.2	80986.2	0.01464	0.00849	2.983	-3.5	-10.9
Low Speed	89	1125853C	regen.	0.222	79.76	58.76	81044.0	80987.6	0.01463	0.02095	2.983		
Low Speed	90	1126851A	process	0.220	29.97	54.92	81766.9	81700.7	0.01477	0.00766	4.469	-4.1	3.0
Low Speed	90	1126851A	regen.	0.222	79.77	54.05	81757.2	81700.2	0.01430	0.02165	4.469		
Low Speed	91	1126852A	process	0.220	29.99	53.70	81730.0	81663.8	0.01481	0.00804	3.774	-3.0	-9.6
Low Speed	91	1126852A	regen.	0.222	79.78	56.29	81720.4	81664.2	0.01433	0.02127	3.774		
High Speed	11	1031852A	process	0.218	29.97	45.67	81391.7	81336.0	0.00590	0.01477	121.192	1.7	3.0
High Speed	11	1031852A	regen.	0.226	49.89	34.11	81377.8	81328.9	0.01748	0.00877	121.192		
High Speed	12	1031853A	process	0.170	29.95	47.01	81253.8	81211.7	0.00825	0.01834	122.049	4.1	1.0
High Speed	12	1031853A	regen.	0.176	49.84	34.14	81242.1	81206.7	0.02084	0.01071	122.049		
High Speed	14	1101851B	process	0.218	29.97	47.36	82093.3	82038.1	0.00715	0.02000	598.751	-1.4	-0.6
High Speed	14	1101851B	regen.	0.226	49.88	33.12	82076.8	82027.6	0.02226	0.01005	598.751		
High Speed	16	1101851D	process	0.331	37.73	55.41	82200.2	82107.6	0.01412	0.00672	601.931	-2.1	200.0
High Speed	16	1101851D	regen.	0.336	59.91	40.88	82183.3	82100.6	0.00472	0.01217	601.931		
High Speed	17	1101852D	process	0.223	26.50	55.77	82025.0	81968.4	0.01847	0.00700	598.410	3.6	-122.7
High Speed	17	1101852D	regen.	0.220	59.84	31.50	82006.8	81957.5	0.00499	0.01620	598.410		
High Speed	18	1101853D	process	0.174	29.95	56.10	81879.9	81837.6	0.01606	0.00642	598.416	-2.4	30.3
High Speed	18	1101853D	regen.	0.172	59.79	31.91	81865.6	81830.0	0.00500	0.01499	598.416		
High Speed	66	1115851A	process	0.169	29.95	47.66	81955.0	81912.0	0.00375	0.01450	638.755	0.2	1.1
High Speed	66	1115851A	regen.	0.173	49.83	32.13	81946.3	81905.0	0.01581	0.00525	638.755		
High Speed	68	1118852A	process	0.218	29.98	47.03	80933.2	80875.8	0.00495	0.01377	638.915	2.5	2.9
High Speed	68	1118852A	regen.	0.222	49.88	32.70	80921.0	80866.5	0.01543	0.00655	638.915		

Table B-1. Experimental Data (Concluded)

Expt. Category	Ser. No.	Run Identifier	Air Stream Tag	Dry Air Flow Rate (kg/s)	Inlet Temprature (C)	Outlet Temprature (C)	Inlet Static Pressure (Pa)	Outlet Static Pressure (Pa)	Inlet Humidity (kg/kg)	Outlet Humidity (kg/kg)	Wheel Rotational Speed (rev/hr)	Balance Errors Mass (%)	Balance Errors Enth. (%)
High Speed	69	1118853A	process	0.333	29.98	45.79	81151.6	81060.6	0.00507	0.01310	638.154	3.3	2.4
High Speed	69	1118853A	regen.	0.339	49.92	34.36	81132.2	81045.1	0.01559	0.00747	638.154		
High Speed	70	1118851C	process	0.172	29.94	56.54	81207.4	81162.3	0.01723	0.00630	645.590	2.5	200.0
High Speed	70	1118851C	regen.	0.171	59.79	32.79	81199.4	81158.2	0.00490	0.01558	645.590		
High Speed	71	1119851A	process	0.171	29.96	56.62	82146.8	82102.3	0.01551	0.00413	594.609	-0.8	0.7
High Speed	71	1119851A	regen.	0.171	59.78	32.71	82138.5	82097.5	0.00230	0.01378	594.609		
High Speed	72	1119852A	process	0.220	29.99	55.92	82345.1	82286.7	0.01626	0.00458	606.723	-2.6	-16.3
High Speed	72	1119852A	regen.	0.220	59.85	33.51	82335.5	82280.2	0.00197	0.01398	606.723		
High Speed	73	1120851A	process	0.337	29.98	54.06	82380.1	82287.9	0.01134	0.00440	605.495	-4.0	-11.1
High Speed	73	1120851A	regen.	0.334	59.89	35.43	82359.0	82270.5	0.00212	0.00941	605.495		

APPENDIX C

FABRICATION OF THE TEST ARTICLE

SERI's parallel-passage dehumidifier test articles 1 and 2 were fabricated with a polyester tape under tension and coated with desiccant. The tape was 203.2 mm wide ARclad 5190, which is 25-μm-thick polyester coated on either side with 25 μm of thermosetting adhesive. The desiccant was crushed, screened, microporous silica gel with a particle size of 150 to 297 μm. The coated tape resulted in an overall tape thickness of 0.67 mm for test article 2. The nominal passage spacing of 1.755 mm yielded a matrix porosity of 0.62.

The following sections describe the fabrication procedure used for test articles 1 and 2. Potential improvements in the matrix fabrication process can be obtained by contacting Ian Maclaine-cross at Monash University, Australia.

C.1 Tape Coating

The roll of carrier tape was coated with Davison Chemical Grade 11 Silica Gel by drawing the tape through a batch of gel with both sides of the tape exposed. The coated tape was continuously taken up by another roll. At the end of each 33-m-long roll, splices were made to obtain a continuous length of approximately 550 m of the coated tape.

C.2 Rotor Winding

Figure C-1 is a photograph of the apparatus used to wind the coated tape onto a circular frame to fabricate the test matrix. The main components of the winding apparatus are the rotor frame (consisting of the rotor hub and spoke assembly), the coated tape feeder roll, a set of rollers, a dancer (to maintain constant tension), and a brake mechanism to control the tape tension during winding.

The rotor frame's hub is made of cast aluminum, machined to a 0.198-mm outer diameter. The radial spoke was an extruded aluminum U-section channel, with rounded edges to cause little disturbance to the air flow. The outer face of the spoke was grooved so that the front and back radial reals could be inserted (see Figure 3-4). The inner face was also grooved to allow the spacers to fit snugly into the spoke. A close-up view of the rotor frame assembly is shown in Figure C-2.*

Test article 1 was wound by Rotary Heat Exchangers, Ltd., in Australia. A close-up view of this article is shown in Figure 3-2. The winding process was similar to that used in the manufacture of rotary heat exchanger matrixes that use smooth Mylar tape with a 100-mm nominal width. Because of the rough surface of the desiccant-coated tape, and the large particle size in relation to the spacer width, our initial attempt at winding resulted in a rather large nonuniformity in the passages.

Test article 1 was tested, however, and the results are reported by Schultz (1986). This article was then unwound and rewound to improve the gap spacing. The rewound article was labeled test article 2.

---

*The photograph is of test article 3, fabricated in FY 1985. Tests on this article are planned for FY 1986.

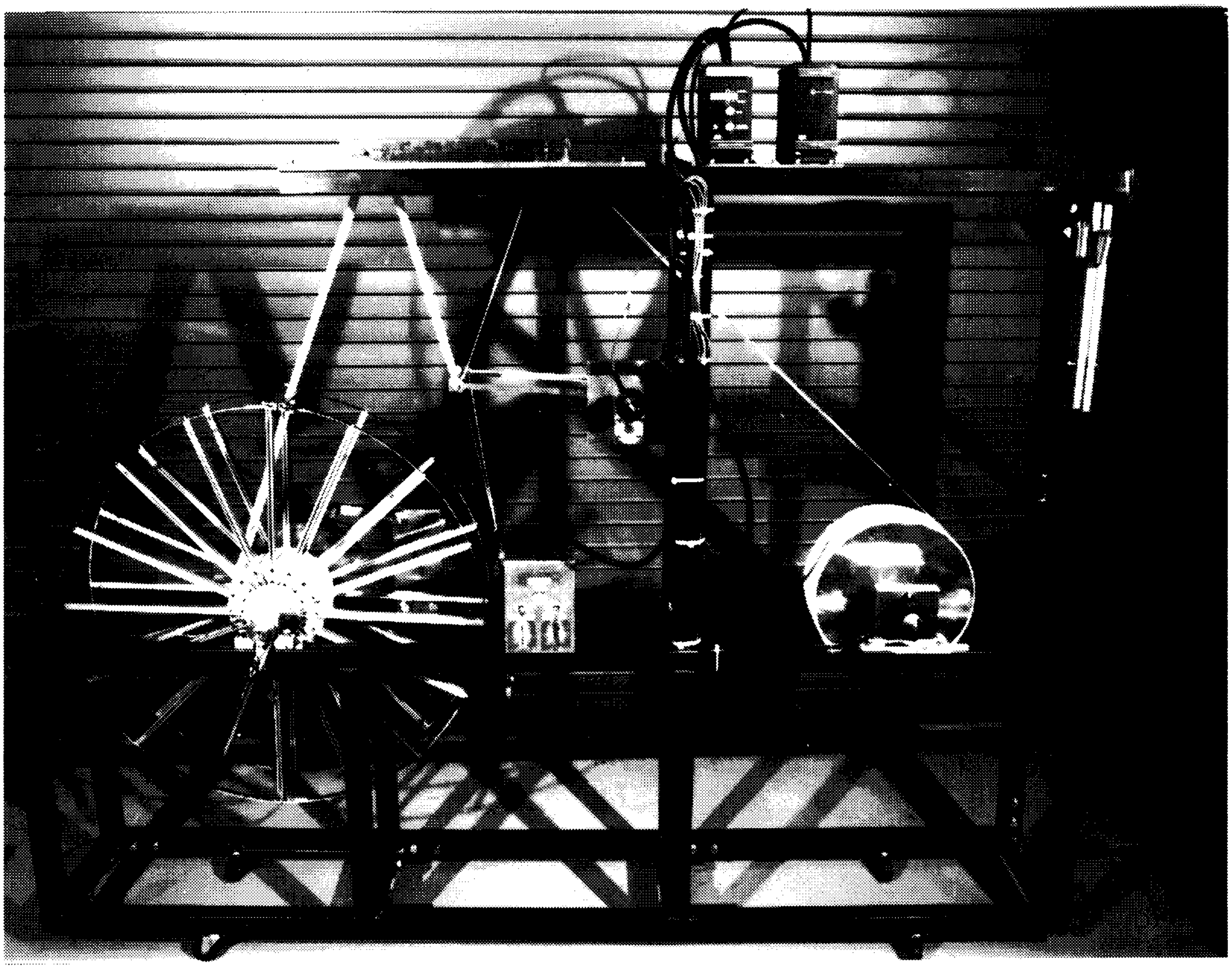

Figure C-1. Photograph of the Rotor Winding Apparatus

Before the rewinding, the cause of the nonuniformity was identified as inadequate radial stiffness of the matrix along the spokes. Later improvements could not, however, be adopted in rewinding test article 1. Thus, temporary "fixes" to increase the radial stiffness were achieved by using minute amounts of epoxy to increase radial support at either ends of the spacers. The spacers and the epoxy used during the rewinding process are shown in the photograph in Figure C-3. The process of inserting the spacer in the spoke is illustrated in Figure C-4. Despite the increased labor requirement, this process considerably improved the gap spacing, as illustrated in Figure 3-3.

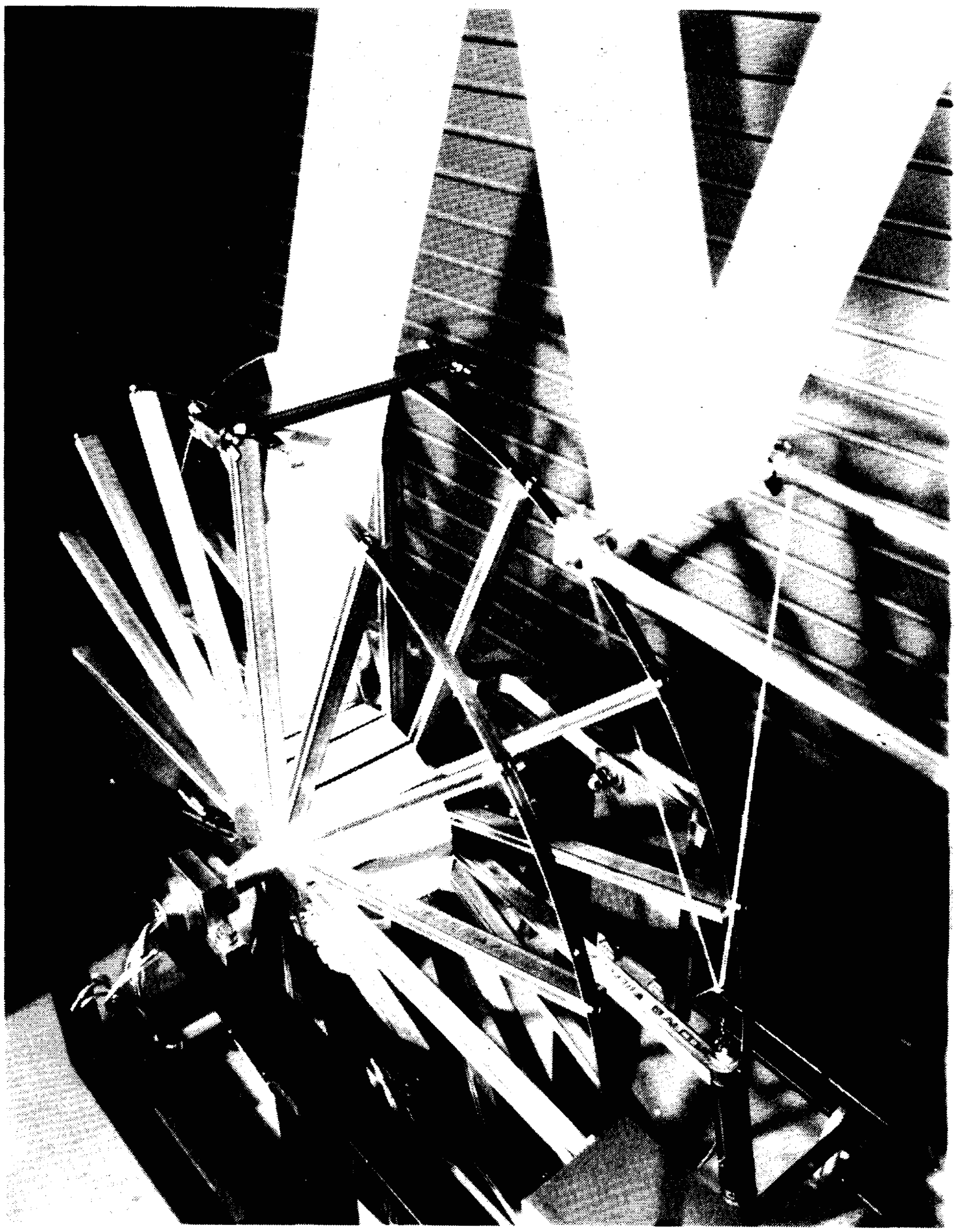

Figure C-2. Photograph Illustrating the Rotor Tape Winding Mechanism

Figure C-3. Photograph of Spacers and Epoxy Resins

008121

Figure C-4a. Adhesive Being Applied to the Spacer Tips

008122

Figure C-4b. Spacer Being Inserted in the Radial Spokes

APPENDIX D

DESICCANT PROPERTIES

D.1 Physical Properties of Desiccant, Substrate, and Humid Air

D.1.1 Silica Gel

The silica gel used in this investigation is Grade 11, manufactured by Davison Chemical Division of W. R. Grace Co. The original batch was crushed and sieved over 50 to 80 wire-mesh screens to yield particles whose nominal size ranged from 150 to 297 μm. Because of its amorphous nature, the gel's density, absorption capacity, isotherm, and related properties are highly variable. Table D-1 summarizes some of the physical properties of the gel used here. Other properties of interest are discussed below.

Table D-1. Physical Properties of Dry Silica Gel

Property	Value	Remarks
Density of fused silica gel ρ_s	2,200 kg/m^3	See Ref. [D-1]
Pore volume v_p	0.43 cc/g	See Ref. [D-2]
Density of dry gel $\rho_d - \rho_s/(1 + v_p\rho_s)$	1,131 kg/m^3	
Specific heat C_p	921 J/kg	See Ref. [D-2]
Thermal conductivity k	0.144 W/m K	See Ref. [D-2]
Tortuosity τ	2.8	See Ref. [D-3]

Water-Vapor Diffusivity in Silica Gel. For surface diffusivity D_s of water molecules on the adsorbent surface, Sladek et al. [D-4] provide a general correlation. With a tortuosity τ of 2.8 for the silica gel, the moisture diffusivity D_w can be expressed as

$$D_w = D_s/\tau = 0.57 \times 10^{-6} \exp \left\{\frac{-0.973 \times 10^{-3} h}{T}\right\} (m^2/s) \ , \qquad \text{(D-1)}$$

where h is the heat of adsorption (J/kg), and T is the absolute temperature (K). Equation D-1 yields diffusivities consistent with the experimentally observed values for silica gel reported in the literature.

Vapor Pressure Isotherm. Isotherm data for Grade 40 silica gel from Ref. [D-2] are tabulated in Table D-2. The Grade 11 isotherm is essentially the same as that of Grade 40. These data were curve-fitted in a least-squares manner to yield

$$W = 0.61\ r - 0.97\ r^2 - 2.78\ r^3 + 1.63\ r^4 \ , \qquad \text{(D-2)}$$

where W is the gel moisture content (kg/kg), and r is the relative humidity. A plot of W versus r, together with the curve-fit representation, is shown in Figure D-1.

Table D-2. Isotherm Data for Grade 40 Silica Gel Taken at 21.1°C (from Ref. [D-2])

Relative Humidity	Gel Moisture Content (kg/kg of dry gel)
0	0
0.10	0.072
0.20	0.137
0.40	0.265
0.60	0.325
0.80	0.353
1.00	0.430

Heat of Adsorption. The Dubinin-Polanyi [D-5] theory predicts that W is a function of the parameter {T ln r}; i.e.,

$$W = f\ (T \ln r)\ . \tag{D-3}$$

This representation of W was found to be accurate for a silica gel moisture system [D-5]. Conversely, Eq. D-3 can be written as

$$\ln p = \ln p_s + \frac{g(W)}{T}\ , \tag{D-4}$$

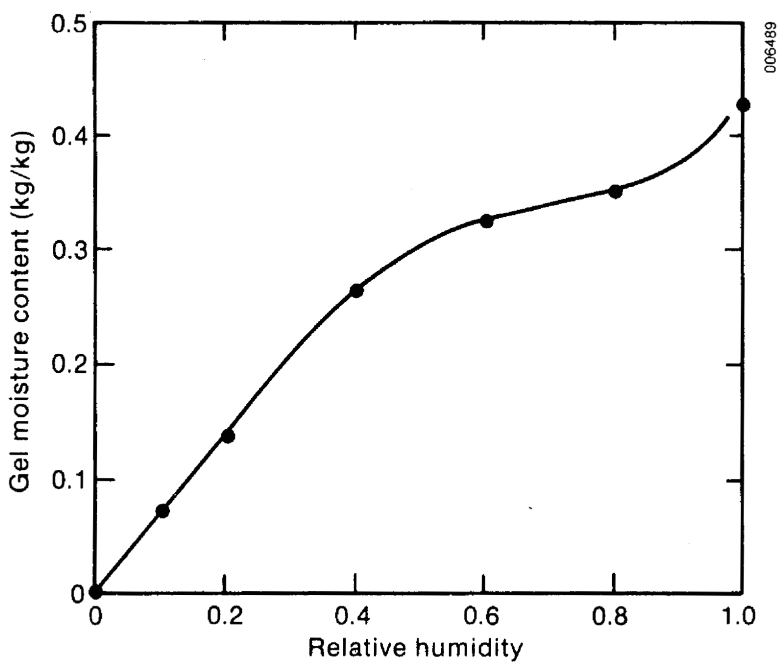

Figure D-1. A Plot of the Silica Gel Isotherm Data Shown in Table D-2 where

p = the vapor pressure (Pa)

p_s = the saturation pressure (Pa) at T temperature (K)

$g(W)$ = an arbitrary function of W alone.

Using the Clausius-Clapeyron equation, the heat of adsorption h can be written as

$$h = h_s \left(\frac{\partial \ln p}{\partial \ln p_s}\right)_W \quad , \tag{D-5}$$

where h_s is the latent heat of vaporization (J/kg).

Reducing Eq. D-5, using Eq. D-4, yields

$$h = h_s \left[1 + T \ln r \frac{d\,(1/T)}{d\,(\ln p_s)}\right] \quad . \tag{D-6}$$

D.1.2 Substrate Tape

The substrate tape used in the matrix fabrication was ARclad 5190. The 25-μm-thick Mylar tape was covered with a 25-μm adhesive layer on both sides. The tape width used was 0.2032 m. The nominal tape surface density was 0.086 kg/m^2. The heat capacity of the tape was taken to be that of Mylar [D-6]:

$$c_{p_{tape}} = 1039 + 4.14t \ (J/kg\ K) \quad ,$$

where t is the temperature (°C).

D.1.3 Humid Air

The following describe the air properties that are used in this report.

Universal gas constant:	$R = 8.3141$ J/mole K
Molecular weight of air:	$M_a = 28.964 \times 10^{-3}$ kg/mole
Molecular weight of water:	$M_R = 18.01534 \times 10^{-3}$ kg/mole

Specific enthalpy of moist air h:

$$h = 1005.22\ t + 0.02615\ t^2 + w\,(2500800 + 1868\ t)\ (J/Kg)$$

where t = temperature (°C)
w = absolute humidity.

Dynamic viscosity of moist air μ:

$$\mu = \frac{1.459 \times 10^{-6}\ T^{3/2}}{(T + 110.77)} - 2.5 \times 10^{-6}\ w \quad ,$$

where T is the absolute temperature (K).

Prandtl number Pr:

$$Pr = 0.7756 - 2.24 \times 10^{-4}\ T\ .$$

Schmidt number Sc:

$$Sc/Pr = 0.7027 + 478 \times 10^{-6}\ T\ .$$

Vapor pressure of water p_r:

$$p_r = \exp\left\{23.28199 - \frac{3780.82}{T} - \frac{22.5805}{T^2}\right\}.$$

D.2 Evaluation of F_i Transfer Properties

The evaluation of F_i transfer properties for a silica gel-air-water system follows the procedures described by Banks [D-7] and Banks and Close [D-8], as modified by Maclaine-cross [D-9]. A brief outline of the procedure is provided here.

The basic heat and moisture transfer equations are written as

$$\frac{\partial w}{\partial \theta} + v\frac{\partial w}{\partial \chi} + \mu\frac{\partial W}{\partial \theta} = 0\ , \tag{D-7}$$

$$\frac{\partial h}{\partial \theta} + v\frac{\partial h}{\partial \chi} + \mu\frac{\partial H}{\partial \theta} = 0\ . \tag{D-8}$$

Here, w and W are the ratios of the mass of the moisture to that of dry air and the matrix, respectively; w represents the absolute humidity; and W is the matrix moisture content. Also, h and H represent the specific enthalpies of the moist air and the matrix, respectively. χ represents a distance in the direction of fluid flow, and θ represents time.

When h, H, and W can be represented as functions of t and w alone, Eqs. D-7 and D-8 can be written as

$$\left(\frac{\partial t}{\partial \theta} + \alpha_i\frac{\partial w}{\partial \theta}\right) + A_i v\left(\frac{\partial t}{\partial \chi} + \alpha_i\frac{\partial w}{\partial \chi}\right) = 0,\ i = 1,2\ , \tag{D-9}$$

where

$$2\alpha_i = (\lambda\alpha_h + \sigma\nu + \alpha_w) - (-1)^i\ [(\lambda\alpha_h + \sigma\nu + \alpha_w)^2 - 4\alpha_w\lambda\alpha_h]^{1/2},\ i = 1,2\ , \tag{D-10}$$

and

$$A_i \approx (1 + \mu\gamma_i)^{-1},\ i = 1,2 \tag{D-11}$$

for air-water systems at ambient pressures, and where

$$\frac{\gamma_i}{\sigma} = \frac{(\alpha_i - \alpha_w)}{\sigma\nu},\ i,j = 1,2,\ i \neq j\ . \tag{D-12}$$

The quantities α_i and γ_i have been expressed in terms of convenient parameters derived from partial differentials of the properties of the fluid mixture and the matrix with respect to each other. Thus,

$$\alpha_h = -\left(\frac{\partial t}{\partial w}\right)_h \text{ and } \alpha_W = -\left(\frac{\partial t}{\partial w}\right)_W$$

are the slopes of lines of constant h and W, respectively, on a t-w plot;

$$\lambda = 1 - \frac{(\partial H/\partial W)_t}{(\partial h/\partial w)_t}$$

is the ratio of the heat of sorption and the enthalpy of the sorbate in the fluid mixture;

$$\sigma = \frac{(\partial H/\partial t)_W}{(\partial h/\partial t)_w}$$

is the ratio of the specific heats of the porous medium and the fluid mixture; and

$$\nu = -\left(\frac{\partial t}{\partial W}\right)_w$$

is a sorption parameter, which contributes to the parameter

$$\beta = -\frac{\alpha_W}{\nu} = \left(\frac{\partial W}{\partial w}\right)_t ,$$

which is termed the sorbability of the porous medium for the sorbate.

Quantities $F_i(t,w)$ are now introduced, which satisfy the equations

$$\left(\frac{\partial F_i}{\partial w}\right)_t = \alpha_i\left(\frac{\partial F_i}{\partial t}\right)_w, \quad i = 1,2 , \tag{D-13}$$

so that multiplying Eqs. D-9 by $(\partial F_i/\partial t)_w$, one obtains

$$\frac{\partial F_i}{\partial \theta} + A_i\nu\frac{\partial F_i}{\partial x} = 0, \quad i = 1,2 . \tag{D-14}$$

Equation D-13 may be written

$$\alpha_i = -\left(\frac{\partial t}{\partial w}\right)_{F_i}, \quad i = 1,2 . \tag{D-15}$$

Hence, each quantity F_i is such that the slope of a line of constant F_i on a t-w plot is given by α_i, which has been defined above in terms of the similar slopes α_h and α_W.

For a mixture of perfect gases,

$$\left(\frac{\partial W}{\partial t}\right)_w = -r\left(\frac{\partial W}{\partial r}\right)_t\left(\frac{\partial \ln p}{\partial t}\right)_W , \tag{D-16}$$

where p is the partial pressure of the water vapor in the gas mixture, and r is its relative humidity p/p_s.

For water vapor in air, at near atmospheric pressures,

$$\frac{p}{p_t} = \frac{w}{(0.622 + w)\, f_w} . \tag{D-17}$$

Using Eq. D-5, and defining the parameter ψ as

$$\psi = \frac{(\partial h/\partial w)_t}{h_s} , \tag{D-18}$$

an expression for the sorption parameter ν is

$$\nu = (\xi \lambda \psi S)^{-1} , \tag{D-19}$$

where

$$S = \frac{d \ln p_s}{dt}$$

depends on the variation of the saturation vapor pressure of the sorbate with temperature, and

$$\xi = r \left(\frac{\partial W}{\partial r}\right)_t$$

depends on the sorption isotherm slope.

From partial differentiation and Eq. D-17, we derive

$$\beta = \left(\frac{\partial W}{\partial w}\right)_t = \zeta \Omega w^{-1} , \tag{D-20}$$

where

$$\Omega = 1 - \frac{f_w p}{p_t} .$$

The set of equations above provides a means of evaluating α_i and γ_i as defined in Eq. D-10 and D-12, provided the vapor pressure isotherm relationship (D-2) is available. The convention of $\gamma_2 > \gamma_1$ is used in all evaluations. The fugacity of water vapor in air, f_w = 1.0030, was lower than that used by Maclaine-cross [D-9] because of the reduced atmospheric pressure at Golden, Colo. (altitude = 1756 m).

D.3 Evaluation of the Intersection Point

Given the process and regeneration inlet conditions t_{pi}, w_{pi}, and t_{ri}, w_{ri}, respectively, the initial values of α and γ at these points are evaluated as described earlier. The intersection point is projected as the intersection of a line with a slope of $\alpha_1 \{= (\frac{\partial t}{\partial w})_{F1}\}$ originating from the process inlet condition and of a line with a slope of α_2 originating from the regeneration inlet condition. An incremental step is taken toward the intersection and updated values of α are evaluated. The estimate of the intersection point is revised and the procedure is continued until the final intersection is achieved.

During this procedure, a continual updating of the process mean values of $\bar{\gamma}_2$ along the F_1 lines and $\bar{\gamma}_1$ along the F_2 line is also evaluated by integrating the local values of γ_1 and γ_2.

D.4 References

D-1. *Handbook of Chemistry and Physics*, CRC Press, 56th Edition, 1975, p. F-78.

D-2. "Silica Gel Grade Chart and Application Guide," Davison Chemical Division, W. R. Grace and Co., Technical Bulletin ADS-16-373, Baltimore, MD.

D-3. Pesaran, A. A., "Moisture Transportation in Silica Gel Particles Bed," Ph.D. Dissertation, School of Engineering, University of California at Los Angeles, 1983.

D-4. Sladek, K. J., E. R. Gilliland, and R. F. Baddour, "Diffusion on Surfaces, II. Correlation of Diffusivities of Physically and Chemically Adsorbed Species," *Ind. Eng. Chem. Fundam.*, Vol. 13, No. 2, 1974, pp. 100-105.

D-5. Ruthven, D. M., *Principles of Adsorption and Adsorption Processes*, New York: John Wiley and Sons, 1984, pp. 82-85.

D-6. Smith, C. W., and M. Dole, "Specific Heat of Synthetic High Polymers, VII. Polyethylene Terephthalate," *J. Polymer Science*, Vol. 20, 1956, pp. 37-56.

D-7. Banks, P. J., "Coupled Equilibrium Heat and Single Adsorbate Transfer in Fluid Flow through a Porous Medium, I. Characteristic Potentials and Specific Capacity Ratios," *Chem. Eng. Sci.*, Vol. 27, 1972, pp. 1143-1155.

D-8. Banks, P. J., and D. J. Close, "Coupled Equilibrium and Single Adsorbate Transfer in Fluid Flow through a Porous Medium, II. Predictions for Silica-gel Air-Drier using Characteristic Charts," *Chem. Eng. Sci.*, Vol. 27, 1972, pp. 1157-1169.

D-9. Maclaine-cross, I. L., "A Theory of Combined Heat and Mass Transfer in Regenerators," Ph.D. Thesis, Department of Mechanical Engineering, Monash University, 1974.

APPENDIX E

SEAL LEAKAGE CHARACTERIZATION

The circumferential and radial seals at the rotor confine the majority of the counter-flowing air streams to their intended path through the dehumidifier and allow the rotor to spin without undue restriction. However, a small portion of the incoming air stream finds its way out of its intended path in the form of leaks. A typical air leakage pattern around the rotor is depicted in Figure E-1. The circumferential leakages are denoted with a single subscript (ℓ_1 through ℓ_4, for example) and the radial leakages are denoted by double subscripts (ℓ_{14} and ℓ_{23}, for example).

To characterize the true performance of a rotary dehumidifier, these seal leakages must be quantified by means of a series of independent seal-leakage tests. The following assumptions on seal-leakage patterns were made. First, each seal-leakage-path air flow can be expressed as

$$\dot{m} = \{C_dA\} \frac{p_1}{\sqrt{RT}} \{(\frac{2\gamma}{\gamma-1}) (r^{2/\gamma} - r^{(\frac{\gamma+1}{\gamma})})\}^{1/2} , \qquad \text{(E-1)}$$

where

p_1 = upstream total pressure (Pa)

T_1 = upstream temperature (K), $r = p_2/p_1$ with p_2 as the downstream static pressure (Pa),

C_dA = an "effective" discharge coefficient times a cross-sectional area available for leakage.

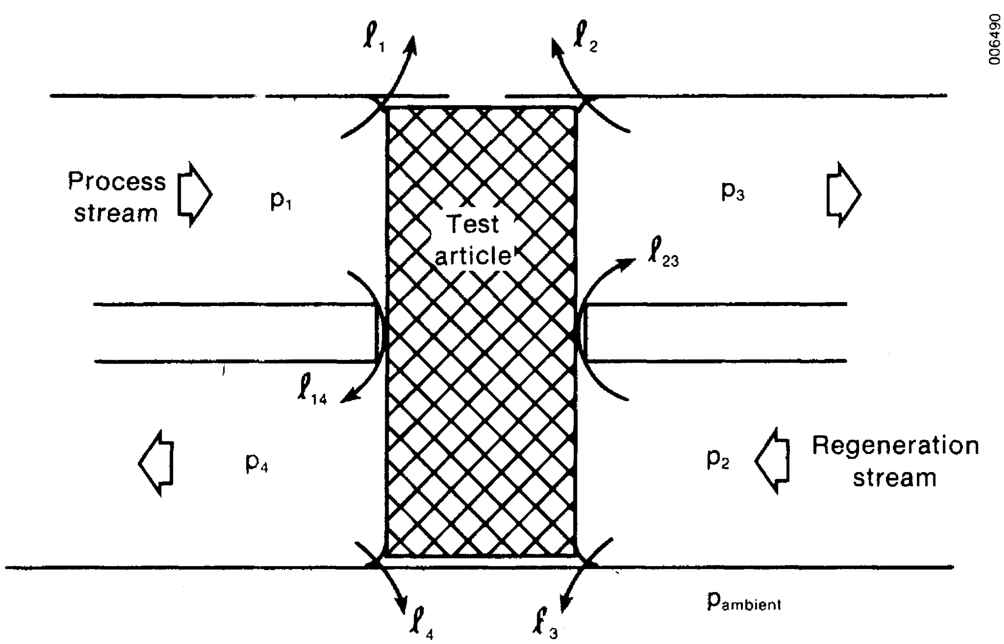

Figure E-1. Diagram Illustrating Leakage Paths around the Dehumidifier

Second, the leakage flow rates ℓ_1 through ℓ_4 can be represented as a function of

$$\ell_i = \text{fn}\{(C_dA)_c, p_i - p_{amb}\}, \quad i = 1 \text{ to } 4; \tag{E-2}$$

and third, the radial leakage flow rates can be represented as a function of

$$\{\ell_{23} = \text{fn}\{(C_dA)_R, p_2 - p_3\}, \text{ and } \ell_{14} = f_n\{(C_dA)_R, p_1 - p_4\} . \tag{E-3}$$

E.1 Circumferential Leakage Tests

These tests were carried out by first introducing a metered air stream m_1 through the process inlet duct and blocking off all other duct inlets and outlets. In this case, the incoming stream

$$m_1 = \ell_1 + \ell_2 + \ell_3 + \ell_4 . \tag{E-4}$$

Static pressures at the four stations (1 through 4) and the ambient pressure were recorded. At these low air flow rates, $p_1 \approx p_3$ and $p_2 \approx p_4$. Using Eqs. E-1 and E-2, we correlated the measurements. The total leakage m_1 is plotted as a function of p_1 in Figure E-2. The static pressure p_2 is also shown in this figure. A least-squares curve-fit to the variations in the data indicated an effective $(C_dA)_c$ for circumferential leakage of 4.8×10^{-4} m^2. Per unit length of the circumferential seal, the effective leak $(C_dA)_c$ product is 1.88×10^{-4} m.

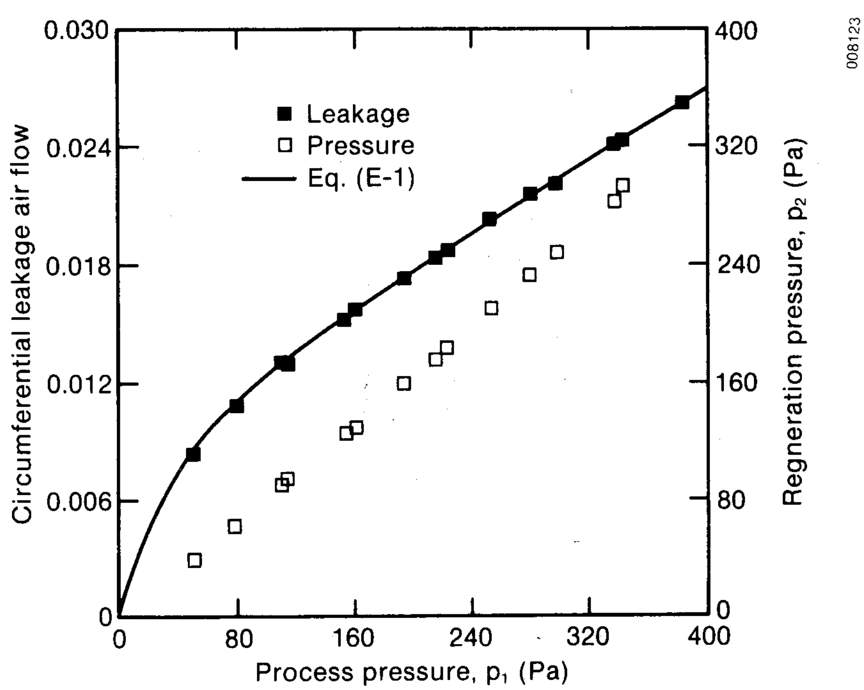

Figure E-2. Circumferential Leakage Flow and Regeneration Pressure vs. Process Pressure and the Fitted Variation of Leakage Using Eq. E-1

E.2 Radial Leakage Tests

The metered air stream m_1 introduced through the process inlet duct was allowed to exit through the regeneration inlet duct. Pressures p_1 through p_4 and the ambient pressure p_{amb} were again monitored.

For this arrangement, the incoming flow can be expressed as

$$m_1 = \{\ell_1 + \ell_2 + \ell_3 + \ell_4\} + \ell_{14} + \ell_{23} .$$

From the earlier circumferential leakage tests, ℓ_1 through ℓ_4 could then be estimated.

The sum of the radial leakages were then correlated as functions of the appropriate pressure differences to yield an effective radial discharge coefficient times area $(C_dA)_R$ of 15.2×10^{-4} m^2. Per unit length of the radial seal, the effective (C_dA) was found to be 9.35×10^{-4} m.

During the radial tests, we found that the radial leakage is somewhat a function of the wheel seal position in relation to the seal plate, i.e., whether a single-seal strip is effective or double strips are. Therefore, data were obtained for wheel positions when the seal leakage is high (i.e., when Δp between stations 1 and 4 is low) and when the seal leakage is low. The quoted $(C_dA)_R$ represents an "average" leakage between the low and high sealing positions of the rotor.

APPENDIX F

EFFECT OF NONUNIFORM AIR PASSAGES

For fully developed laminar flow through parallel passages of varied passage spacing, the pressure-drop and heat-transfer characteristics can be expressed by means of the parameters (fRe), K, and Nu, representing the intercept and slope of the pressure-loss variation, and the effective Nusselt number, respectively.

If the probability density function for the distribution gap size, b, is represented by p(b), in a domain $o < b < \infty$, the mean gap size b_m is

$$b_m = {}_o\int^{\infty} p(b)b\ db / {}_o\int^{\infty} p(b)db\ . \tag{F-1}$$

The three parameters listed above can then be expressed as*

$$\frac{(fRe)}{(fRe)_{pp}} = \frac{b_m^3}{{}_o\int^{o} p(b)\ b^3\ db}\ , \tag{F-2}$$

$$K = \frac{108}{35} \frac{b_m{}^2\ {}_o\int^{\infty} p(b)\ b^7\ db}{\left({}_o\int^{\infty} p(b)\ b^3\ db\right)^3} - \frac{12}{5} \frac{b_m\ {}_o\int^{\infty} p(b)\ b^5\ db}{\left({}_o\int^{\infty} p(b)\ b^3\ db\right)^2}\ , \tag{F-3}$$

and

$$\frac{Nu}{Nu_{pp}} = \frac{b_m \left({}_o\int^{\infty} p(b)\ b^3\ db\right)^2}{{}_o\int^{\infty} p(b)\ b^7\ db}\ . \tag{F-4}$$

For the present rotor, a simple probability distribution, shown in Figure F-1, is assumed. $(1 - p_f)$ represents a fraction, $0 \le p_f \le 1$, of passages that possess the mean gap spacing b_m. The remaining fraction p_f is assumed to be uniformly distributed in a gap size range of $(2-R_m)$ to R_m times b_m, for R_m values in a range of 1 to 2.

With these assumptions, we find

$$\overline{b^3} = \frac{\int p(b)\ b^3\ db}{\int p(b)\ db} = (1-p_f) + \frac{p_f\ \{R_m{}^4 - (2-R_m)^4\}}{8\ (R_m - 1)}\ , \tag{F-5}$$

$$\overline{b^5} = \frac{\int p(b)\ b^5\ db}{\int p(b)\ db} = (1-p_f) + \frac{p_f\ \{R_m{}^6 - (2-R_m)^6\}}{12\ (R_m - 1)}\ , \tag{F-6}$$

and

$$\overline{b^7} = \frac{\int p(b)\ b^7\ db}{\int p(b)\ db} = (1-p_f) + \frac{p_f\ \{R_m{}^8 - (2-R_m)^8\}}{16\ (R_m - 1)}\ . \tag{F-7}$$

---

*Maclaine-cross, I. L., 1969, "An Approximate Method for Calculating Heat Transfer and Pressure-Drop in Ducts with Laminar Flow," *J. of Heat Transfer*, Vol. 91, pp. 171-173.

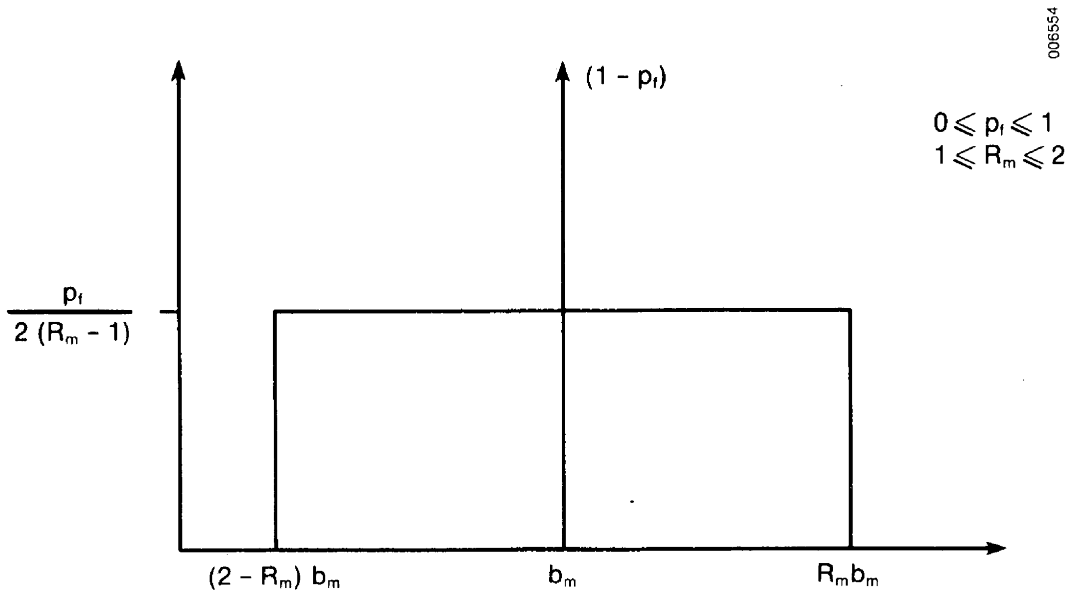

Figure F-1. Assumed Probability Distribution of the Air Passage Gap

Using these equations, together with Eqs. F-2 through F-4, we can evaluate the variations of (fRe), K, and Nu as functions of p_f and R_m.

From the pressure-loss results described in Section 5.1.2, the parameters (fRe) and K were found to be 16.8 and 3.98, respectively. Iterative evaluations varying both p_f and R_m to match the experimental results resulted in a determination of their values as $p_f = 0.48$ and $R_m = 1.92$. At these values, the predicted Nusselt number Nu was found to be 31% of that of the parallel-plate limit of $Nu_{pp} = 8.235$ (for constant-heat-flux boundary conditions).

APPENDIX G

RAW DATA PROCESSING PROCEDURE

Since finite circumferential and radial leaks exist at the rotor housing, the recorded data must be corrected to arrive at "true" measured rotor inlet and outlet conditions. Corrections must also be made for air carried over between streams (especially at high rotational speeds) and for heat loss through ducts from the measuring stations to locations adjacent to the dehumidifier. The correction procedure to accomplish this is described next.

The raw experimental data provide the following information for the process and regeneration streams, respectively:

$\dot{m}_1$, $\dot{m}_2$	dry-air flow rates to the rotor housing (kg/s)
t_1, t_2	inlet air temperatures (°C)
t_{dp1}, t_{dp2}	inlet air dew-point temperatures (°C)
t_3, t_4	outlet air temperatures (°C)
t_{dp3}, t_{dp4}	outlet air dew-point temperatures (°C)
Δp_p, Δp_r	static pressure difference across the dehumidifier (Pa)
Δp_{po}, Δp_{ro}	static pressure difference across outlet flow metering nozzles (Pa).

In addition, ambient pressure, temperature, and dew points are also recorded at each test condition.

(1) Estimates of static pressures upstream and downstream of the rotor for each stream are found as

$$p_{po} = p_{amb} + \Delta p_{po} \ , \tag{G-1}$$

$$p_{pi} = p_{po} + \Delta p_p \ , \tag{G-2}$$

and similarly,

$$p_{ro} = p_{amb} + \Delta p_{ro} \ , \tag{G-3}$$

$$p_{ri} = p_{ro} + \Delta p_r \ . \tag{G-4}$$

(2) The circumferential leakages ℓ_1 through ℓ_4 are calculated as in Appendix E.

(3) The direction of cross leakage between the two streams is determined by checking the sign of $(p_{pi} - p_{ro})$ for ℓ_{14} and $(p_{ri} - p_{po})$ for ℓ_{23}. Positive signs for both these pressure differences indicate that the leakages ℓ_{14} and ℓ_{23} are positive; i.e., leakage occurs from the process inlet area to the regeneration outlet and from the regeneration inlet to the process outlet.*

*For balanced flow, only positive cross leakage was found to occur in all the test data reported.

(4) Based on the appropriate pressure difference, the cross-leakage flow rates ℓ_{14} and ℓ_{23} are calculated (see Appendix E).

(5) The dry air mass flow into the process and regeneration sides of the test article are calculated as

$$\dot{m}_p = \dot{m}_1 - \ell_1 - \ell_{14} \tag{G-5}$$

and

$$\dot{m}_r = \dot{m}_2 - \ell_2 - \ell_{23} \ . \tag{G-6}$$

(6) The measured dew points are converted to absolute humidity in terms of kg of vapor per kg of dry air, based on the static pressure inferred in step 1. The absolute humidities are now denoted by w_1 through w_4.

(7) Since both ℓ_{14} and ℓ_{23} were found to be positive for all the reported test conditions, the process and regeneration inlet conditions are the same as those measured at stations 1 and 2, respectively; i.e.,

$$t_{pi} = t_1, \ t_{ri} = t_2 \tag{G-7}$$

and

$$w_{pi} = w_1 \ , \ w_{ri} = w_2 \ . \tag{G-8}$$

(8) From the downstream seals, an additional air leak out of the housing causes the mass flow at measurement stations 3 and 4 to be, respectively,

$$\dot{m}_3 = \dot{m}_p - \ell_3 + \ell_{23} \tag{G-9}$$

and

$$\dot{m}_4 = \dot{m}_r - \ell_4 + \ell_{14} \ . \tag{G-10}$$

(9) The measured temperatures at stations 1 through 4 are corrected for heat loss from the ducts to arrive at temperatures at the dehumidifier's entry and exit.

(10) For high-speed tests, the process and regeneration outlet conditions are also corrected for air carried over from one side to the other.

(11) If t_{po}, w_{po}, and h_{po} represent the true rotor outlet temperature, humidity, and specific enthalpy, respectively, then the mass and enthalpy balance for the mixing of the cross-leakage stream from the regeneration inlet yields

$$(\dot{m}_p - l_3)\ w_{po} + \ell_{23}\ w_{ri} = m_3\ w_3 \tag{G-11}$$

and

$$(\dot{m}_p - l_3)\ h_{po} + \ell_{23}\ h_{ri} = m_3\ h_3 \ . \tag{G-12}$$

Here, h_3 is the specific enthalpy at station 3.

Equations G-11 and G-12 are then solved to arrive at w_{po} and h_{po}; t_{po} can readily be found from w_{po} and h_{po}.

(12) A similar set of calculations, described in step 11, is repeated for the regeneration side to arrive at the true rotor outlet temperature, humidity, and enthalpy, namely, t_{ro}, w_{ro}, and h_{ro}, respectively.

(13) Estimates of heat loss through the ducts from the measurement stations to locations adjacent to the dehumidifier are made; the temperatures of the air stream at all four locations are revised. All steps through step 13 are repeated until a convergence to within ± 0.02°C of all temperatures is achieved.

(14) Energy and mass balances across the dehumidifier are then made to verify the calculations and the experimental data to ensure overall balance errors of less than 2%.

The experimental data reported in Appendix B represent the true rotor inlet and outlet conditions for both streams.

APPENDIX H

DETAILED OPERATING PROCEDURE

The following is a short description of the experimental procedure, assuming that the operator is starting the loop from its overnight shutdown. When the system is left unattended overnight, power to the main system components is turned off at the main breaker panels. To start the system, the first step is to supply power to these components. Four switches on the 480-V breaker panel provide power to the fans, heaters, and boiler, and a single switch on the 120-V breaker panel provides power to the boiler SCR control loop. The following is a list of additional switches and valves located adjacent to the components; it is important to ensure that they are all in the "on" position for system operation.

- Fans (same for both process and regeneration fans)
  - A large, enclosed switch to connect power to the fan and the Fincor variable-speed controller
  - Switch to "auto" position and press run button
- 6-kW heater (process stream heater)
  - "Door closing" switch
  - 120-VAC switch to connect power to contacters
- 35-kW heater (regeneration stream heater)
  - "Door closing" switch
  - "Step no. 1" switch to connect power to contacters
- Wheel drive
  - On/off switch on KEPCO power supply to power the drive motor
  - Archer AC adapter plugged in and set to 4.5 V to supply power for the optical encoder
- Boiler
  - Two switches to connect power to boiler SCR control loop
  - Water supply valve
- Humidifiers (same for both process and regeneration humidifiers)
  - Compressed air valve open to the pneumatic control valve
  - Steam valve from boiler open to supply humidifier
  - Bleed valve open slightly.

At this point, the operator must check that all the instrumentation is connected and functioning properly. The sampling pumps in the four humidity sensing loops must be on, and checking the flow meters in these loops is a convenient way to be sure they are. The thermocouple connectors and the lines to the six differential-pressure transducers should also be checked visually. Mirrors inside each of the four humidity sensors should be cleaned every 4-6 weeks. This is the point in the procedure, before the hygrometers have been balanced, at which the mirrors should be cleaned. Finally, the five hygrometers (including the ambient hygrometer) are balanced, and the differential pressure transducers are zeroed (on the DAS control panel for P_1-P_4, and at the transducer for P_5-P_7). Ambient temperature and pressure are read and recorded from a thermometer and barometer on the east wall of the laboratory and checked against the thermocouple thermometers (now reading approximately ambient temperature) and P_7 (the ambient pressure).

If data are to be saved on a diskette, a diskette with enough space for a day's data must be inserted in drive B of the IBM PC. This is the best time to check how much space is remaining. If less than 100 kilobytes are available, it is advisable to use a new diskette. The IBM Basic data acquisition program "JPDAS" can then be loaded and run.

The initial program prompt asks for the correct date. Data files are named using the date given, so if data are being taken, it is important that the date be correct. The operator can then enter up to five experiments, specifying inlet temperatures, humidity ratios, mass flow rates, and wheel speeds for each experiment. We have found it convenient to enter five experiments: four for data-taking purposes, and the fifth as a cooling-down period during which room air is circulated through the system. Typically, we have chosen values of 10 readings for pressure averages, 10 seconds for the data update interval, and 60 seconds for the printer and storage update interval.

Once an experiment has begun, the operator can be confident that the temperature and mass flow rates specified will be reached within 5 minutes. But the experimenter must manually control the humidity ratios (from the keyboard) and the wheel speed (at the drive motor power supply). The humidity ratios can take up to an hour to come close to the specified conditions, i.e., with 0.0005 kg/kg above or below the specified humidity ratio.

The inlet and outlet temperatures, mass flow rates, humidity ratios, the wheel speed, and the enthalpy and mass balance errors are updated as often as every 10 seconds on the CRT screen. A trend plot on a Leeds and Northrup strip chart traces the inlet and outlet temperatures and dew-point temperatures. The operator remains in the transient data routine until the update screen shows low enthalpy and mass balance errors (±1%), and the trend plot shows the inlet and outlet conditions to be in a steady state. As a rule of thumb for low and medium wheel speeds, once both of the conditions above have been met for 15 minutes, the operator strikes the appropriate key to enter the steady-state routine. The length of time spent in the steady-state routine depends on the wheel speed. At very low speeds, we allow at least four segments of the rotor to rotate from one flow stream to the other. Because of the periodic nature of the outlet states at low wheel speeds, it is important to exit the steady-state routine only after an integral number of periods. At medium speeds, the outlet states are much less periodic, and we normally remain in the steady-state routine for 20 minutes before going on to the next experiment. As indicated earlier, data gathering for high speeds occurs over a much longer time interval.

At the end of a series of tests, the data acquisition program is ended. All equipment and instruments are shut down in an order that is exactly the reverse of the start-up sequence.

APPENDIX I

DETERMINATION OF DEHUMIDIFIER STATIC CAPACITY

To determine the static wheel capacity independently of the heat- and mass-transfer tests, we measured the weight of the dehumidifier wheel at two different relative humidities under static equilibrium. The effective silica gel mass and the effective silica gel fraction were calculated using the low-speed-test data-reduction procedure to estimate the water uptake in the desiccant at each relative humidity and also using the difference in wheel weight.

An experimental rig was constructed adjacent to the CTF using only the conditioned airflow capabilities of the CTF. The rotor was removed from its flanges and housing and set in an enclosure on a 60-kg scale (Mettler, Model #PK60). Air of a controlled temperature and humidity was blown through the enclosure; the measured quantities were enclosure air temperature and dew-point temperature, ambient pressure, and wheel weight. When the rotor reached equilibrium with the enclosure conditions (inferred from constant wheel weight data), a data point was taken.

The low-speed data reduction program was used to calculate the change in the water uptake in the desiccant (kg of water/kg of dry desiccant) between the two data points. With this information and the change in wheel weight (in kg of water) between the two data points, we calculated the effective silica gel mass and the effective silica gel fraction. Table I-1 provides a summary of the measurements.

Table I-1. Summary of Measurements for Determination of Wheel Static Capacity

Data Point Number	Pressure (mm Hg)	Temp. (^oC)	Dew-Point Temp. (^oC)	Relative Humidity (%)	Absolute Humidity (g H_2O/ kg dry air)	Water Uptake (kg H_2O/ kg dry des.)	Wheel Weight (kg)
1	612.3	32	7.0	20.47	7.746	0.13576	40.736
2	612.2	33	18.2	42.71	16.34	0.26855	42.104

Notes:

Δ water uptake = 0.13279 kg/kg.

Δ wheel weight = 1.368 kg.

Effective gel mass [Δ wheel weight/Δ water uptake] = 10.30 kg.

Calculated gel mass = 15.147 kg.

Effective gel fraction = 68% (with a ±5% estimated uncertainty).

SELECTED DISTRIBUTION LIST

William M. Anderson
Anderson Consulting
7605 E. Windlawn Way
Parker, CO 80134

Carl Bergt
Trane Systems Engineering Co.
6200 Troup Highway
Tyler, TX 75711

Kennard L. Bowlen
Cargocaire Engineering Corp.
79 Monroe St.
Amesbury, MA 01913

Glen Chinery
Tennessee Valley Authority
217 Power Board Bldg
Chattanooga, TN 37401

James Coellner, Director R&E
American Solar King Corp.
700 Loop 340 South
Waco, TX 76710

Barry Cohen
Thermal Products Division
ThermoElectron Corporation
45 First Avenue
Waltham, MA 02154

Kirk Collier, Ph.D.
Everscope, Inc.
4886 W. Port Au Prince
Glendale, AZ 85306

Keith Davidson
Gas Research Institute
8600 West Bryn Mawr Avenue
Chicago, IL 60631

Jim Hill, Ph.D.
National Bureau of Standards
Technology B-148
Washington, DC 20585

Michael Epstein
Fauske & Associates, Inc.
162070 West 83rd Street
Burr Ridge, IL 60521

Phillip Fairey
Florida Solar Energy Center
300 State Road, 401
Cape Canaveral, FL 32920

A. Hunter Fanney, Ph.D.
Bldg. 226, Room B310
National Bureau of Standards
Washington, DC 20234

Stephen D. Fitch
Bry-Air
P. O. Box 795
Sunbury, OH 43074

Paul Gandhidasan, Ph.D.
Dept. Mechanical Engineering
Texas A&M University
College Station, TX 77843

John Goldsmith
U.S. Department of Energy
Route CE-311, Room 5H065
1000 Independence Ave., S.W.
Washington, DC 20585

William C. Griffiths
Midland Ross Corporation
P. O. Box 791
New Brunswick, NJ 08903

R. Harkins
ASES
2030 17th St.
Boulder, CO 80302

Richard B. Hayter, Ph.D.
Engineering Extension
Ward Hall, Kansas State University
Manhattan, KS 66506

Anthony Hines, Ph.D.
College of Engineering
Oklahoma State University
Stillwater, OK 74078

Ralph Johnson
NAHB Research Foundation, Inc.
3720 T St., N.W.
Washington, DC 20007

Robert Jones
Los Alamos National Lab
P.O. Box 1663
Mail Stop H577
Los Alamos, NM 87545

K. LaPorta
SEIA
1156 15th St., N.W., Suite 520
Washington, DC 20005

Zalman Lavan, Ph.D.
Illinois Institute of Technology
Department of Mechanical Engineering
Illinois Institute of Technology Center
Chicago, IL 60616

Robert LeChevalier
U.S. Department of Energy
San Francisco Operations Office
1333 Broadway
Oakland, CA 94612

George O. G. Lof, Ph.D.
Colorado State University
Solar Energy Applications Lab
Fort Collins, CO 80523

John Mitchell, Ph.D.
University of Wisconsin-Madison
Engineering Research Building
1500 Johnson Drive
Madison, WI 53706

Jeff Morehouse
Department of Mechanical Engineering
University of South Carolina
Columbia, SC 29208

Frederick Morse, Ph.D.
U.S. Department of Energy
Route CE-31, Room 5H-095
1000 Independence Ave., S.W.
Washington, DC 20585

Stanley A. Mumma
104 Engineering "A" Building
University Park, PA 16802

Yves O. Parent
Res. Eng.
Industrial Chemicals Research
Davison Chemical Division
W. R. Grace & Co.
Washington Research Center
7379 Route 32
Columbia, MD 21044

David Pellish
Solar Buildings Technology Division
Office of Solar Heat Technology
U.S. Department of Energy
Forrestal Building, Room 5H-041
1000 Independence Ave., S.W.
Washington, DC 20585

D. M. Ruthven, Ph.D.
University of New Brunswick
P. O. Box 4400
Fredericton, N.B.
Canada E58 5A3

William Seaton
ASHRAE
1791 Tullie Circle, NE
Atlanta, GA 30329

M. Wahlig, Ph.D.
Lawrence Berkeley Laboratories
University of California
1 Cyclotron
Berkeley, CA 94720

Alex Willman
ACEC Resource and Management Foundation
1015 15th Street, N.W.
Washington, DC 20005

Byard Wood, Ph.D.
Department of Mechanical & Aerospace Engineering
Arizona State University
Tempe, AZ 85287

Document Control Page	1. SERI Report No. SERI/TR-252-2897	2. NTIS Accession No.	3. Recipient's Accession No.

4. Title and Subtitle Experimental Studies of Heat and Mass Exchange in Parallel-Passage Rotary Desiccant Dehumidifiers for Solar Cooling Applications	5. Publication Date November 1987 6.
7. Author(s) D. Bharathan, J.M. Parsons, I.L. Maclaine-cross	8. Performing Organization Rept. No.
9. Performing Organization Name and Address Solar Energy Research Institute 1617 Cole Boulevard Golden, Colorado 80401	10. Project/Task/Work Unit No. 3023.210 11. Contract (C) or Grant (G) No. (C) (G)
12. Sponsoring Organization Name and Address	13. Type of Report & Period Covered Technical Report 14.

15. Supplementary Notes

16. Abstract (Limit: 200 words)

This report presents results of work done to experimentally characterize the performance of rotary desiccant dehumidifiers and to develop and validate analytical methods for evaluating their performance in air-conditioning systems. A facility, the Cyclic Test Facility, and a test-and-analysis procedure were developed to evaluate the performance of the rotary dehumidifiers. Experiments were performed to develop a basic understanding of the simultaneous heat- and mass-transfer processes in the dehumidifiers. Two test articles were tested under cyclic operation to characterize their performance. Detailed accounts of the Cyclic Test Facility, its hardware and instrumentation, the two test articles, and data reduction and analysis methods are provided. The data provide an engineering data base for evaluating rotary desiccant dehumidifiers for cooling applications.

17. Document Analysis

a. Descriptors Solar cooling systems ; hehumidifiers ; desiccants ; air conditioning ; heat transfer ; mass transfer

b. Identifiers/Open-Ended Terms

c. UC Categories

59a

18. Availability Statement National Technical Information Service U.S. Department of Commerce 5285 Port Royal Road Springfield, VA 22161	19. No. of Pages 101 20. Price A06